Transition metal impurities in wide bandgap oxides: fundamental model systems for strongly correlated oxides

I n a u g u r a l - D i s s e r t a t i o n
zur
Erlangung des Doktorgrades
der Mathematisch-Naturwissenschaftlichen Fakultät
der Universität zu Köln

vorgelegt von
Tim Jakobus Thomas Haupricht
aus Köln

Köln 2011

Berichterstatter:
Prof. Dr. L. H. Tjeng
Prof. Dr. T. Michely

Tag der mündlichen Prüfung:
03.02.2011

Abstract

Most of the modern electronic devices are still based on the electrical properties of metals and semiconductors. Yet, the transition metal oxides show a variety of spectacular physical effects like, e.g., high-temperature superconductivity, the giant or tunnel magneto resistance, spin-polarized transport, metal to insulator transitions, or multiferroic order. If ways could be found to make use of these phenomena, one could obtain devices with unprecedented functionalities. This, however, requires a profound understanding of the electronic structure of these compounds. Electron-electron correlations are very important here, thereby requiring a more sophisticated theoretical *ansatz*. An effective first order approach to take these correlation effects into account is to neglect the translational symmetry of the real crystal and to describe the electronic structure in a local single-site impurity model. This is done for example in the so-called configuration-interaction cluster calculations where the system is reduced to a single ion and its ligands, and also, at least for the correlations, in dynamical mean-field theory (DMFT). The underlying idea is that the ground state and near ground state properties as well as the excitation spectra can be described on an equal footing as far as the many body aspects are concerned. It is not always easy, however, to judge about the applicability of the results for the real bulk systems. An experimental test is highly desired.

In this thesis we have, therefore, set out to study the electronic structure of selected transition metal impurities in oxides using photoemission (PES) and x-ray absorption spectroscopy (XAS). We have simulated our experimental data using a single-site cluster model and compare the results to the respective bulk systems. We found that transition metal impurities in oxides are fundamental model systems to study the electronic structure of strongly correlated oxides. A detailed study of their electronic structure yields essential information on the importance of local and non-local interactions in the associated bulk compounds and even more complicated materials.

Kurzzusammenfassung

Die Funktionsweise moderner elektronischer Geräte basiert noch immer weitestgehend auf den elektronischen Eigenschaften von einfachen Metallen und Halbleitern. Übergangsmetalloxide hingegen weisen eine Vielzahl spektakulärer physikalischer Eigenschaften auf. So zeigen Sie z.B. Hochtemperatursupraleitung, den Riesen- oder Tunnelmagnetwiderstand, Spinpolarisierten Transport, Metall-Isolator Übergänge oder multiferroische Ordnung. Die technische Nutzung dieser Phänomene würde einen Zugang zu Geräten mit nie dagewesenen Eigenschaften ermöglichen. Diese allerdings erfordert ein tiefgehendes Verständnis der elektronischen Struktur dieser Verbindungen. Elektron-Elektron Wechselwirkungen sind hier sehr ausgeprägt und erfordern eine anspruchsvollere und detailliertere theoretische Behandlung. In einem weit verbreiteten und sehr erfolgreichen Ansatz zur Berücksichtigung dieser Korrelationseffekte wird die Translationssymmetrie eines realen Kristalls vollkommen vernachlässigt. Stattdessen wird die lokale elektronische Struktur einer einzigen isolierten Störstelle beschrieben. Diesen Ansatz verfolgen sog. *configuration-interaction* Clusterrechnungen, in denen der Festkörper auf ein einzelnes Ion nebst den dazugehörigen Liganden reduziert wird. Die zugrunde liegende Idee ist, dass hier Grundzustands- und Nahgrundzustandseigenschaften sowie Anregungsspektren im Hinblick auf Korrelationseffekte gleichberechtigt behandelt werden können. Auch eine der am weitesten fortgeschrittenen Methoden der theoretischen Festkörperphysik, die dynamische Mean-Field Theorie (DMFT), basiert auf diesem Ansatz. Trotzdem ist es oft nicht leicht zu beurteilen, wie gut die Ergebnisse und Modellparameter auf reale, ausgedehnte Systeme übertragbar sind. Ein experimenteller Test wäre daher sehr wünschenswert.

Diese Arbeit beschäftigt sich aus diesem Grund mit der Untersuchung der elektronischen Struktur von Übergangsmetall-Störstellen in Oxiden mittels Photoemissions- (PES) und Röntgenabsorptionsspektroskopie (XAS). Die gewonnenen experimentellen Daten wurden im Rahmen von Clusterrechnungen simuliert, und die Ergebnisse mit den zugehörigen Volumensystemen verglichen. Es wird gezeigt, dass Übergangsmetall-Störstellen in Oxiden als

fundamentale Modellsysteme zur Untersuchung der elektronischen Struktur stark korrelierter Oxide dienen können. Ihre detaillierte Untersuchung liefert essentielle Informationen über den Einfluss lokaler und nicht-lokaler Wechselwirkungen in den zugehörigen Volumensystemen oder weitaus komplizierteren Verbindungen.

Contents

Abbreviations

XAS	X-ray absorption spectroscopy
(I)PES	(Inverse) Photoemission spectroscopy
XPS	X-ray photoemission spectroscopy
HAXPES	Hard x-ray photoemission spectroscopy
MBE	Molecular beam epitaxy
UHV	Ultra-high vacuum
CI	Configuration-interaction
DFT	Density functional theory
DMFT	Dynamical mean-field theory
L(S)DA	Local (spin-)density approximation
DOS	Density of states
NSRRC	National Synchrotron Radiation Research Center
MIT	Metal to insulator transition

Chapter 1

Introduction

This thesis deals with the investigation of the electronic structure of transition metal impurities in oxides. It will be shown how these impurity systems can be used as fundamental model compounds for (usually much more complicated) correlated electron systems, and to test the reliability of recent electronic structure theories. Therefore, in this first introductive chapter we will briefly outline the most important physical concepts of strongly correlated electron systems and some basic ideas of a popular method of the local electronic structure calculation for these compounds, namely, the configuration-interaction cluster model. In Section 1.3 the key issues and aims of this thesis will be introduced.

1.1 Correlated electron systems

One of the key problems in modern technology is to find proper materials for new applications and devices. Most modern electronics is still based on the transistor invented in the 1940s by Schockley, Bardeen, and Brattain [1].[1] These transistors make use of the charge degree of freedom of the electron. Since then it is one of the key issues in the design of integrated electronic circuits to increase the number of transistors per area. Today's microprocessors are built from 32 nm structures produced using extreme ultraviolet (EUV) lithography [2]. This is already very close to the physical limit of integration which is in the order of a few Å, the size of single atoms. Modern materials research tries to make also use of other properties of the electron, like, e.g., the spin and the orbital degrees of freedom. The ordering of these charge, orbital, and spin degrees of freedom, their fluctuations, interactions, and coupling to the crystal lattice lead to a variety of phenomena. New ef-

[1] W. B. Shockley, J. Bardeen, and W. H. Brattain, Nobel Prize in 1956

fects like high-T_c superconductivity[2], giant magneto resistance (GMR)[3] and tunnel magneto resistance (TMR) [3], spin-polarized electron transport [4, 5], or metal to insulator transitions [6] have been found from which part of them are already used in modern devices. In so-called multiferroics two or more ferroic phases appear simultaneously, opening a path to multi-functional materials, very interesting with respect to device miniaturization [7]. In order to understand all these effects or, in the second step, to develop new materials or compounds for applications, a profound comprehension of the underlying physics and the electronic structure is indispensable. Unfortunately, most of these effects can no longer be explained by one-electron theory. Electron-electron interactions play a major role here, and thus electrons cannot be described as embedded in a static mean-field generated by the other electrons [8]. Due to the importance of these correlations, such systems are referred to as *correlated electron systems*. In this field of fundamental research binary transition metal monoxides are often regarded as "simple" model systems for more complicated compounds containing more elements in different environments. However, most of these binary transition metal monoxides are by far not that simple as they might appear at first sight.

It was kind of a starting point of correlated electron physics when de Boer and Verwey [9] pointed out that many of the properties of the $3d$ transition metal compounds do not agree with the predictions of band theories. In basic classes of solid state physics we learn that [10]: "In the ground state of an insulator all bands are either completely filled or completely empty; in the ground state of a metal at least one band is partially filled." Thus, from a band theory point of view, systems with an incompletely filled $3d$ shell should be a metal. Standard density-functional theory (DFT) [11, 12] predicts FeO, CoO, and CuO to be metallic [13, 14], for MnO and NiO a (way too small) bandgap is found, but only in the magnetically ordered phase [13, 15, 16]. Experimentally, all of these compounds have been found to be insulators with bandgaps between about 1 and 4 eV. In DFT calculations this problem could be fixed by the inclusion of a so-called self-interaction-correction term into the model, which than gives reasonable values for the bandgap [17]. However, even though DFT methods have shown to give a good description of the ground state properties of many systems with weak correlation effects [17], they usually fail to reproduce excitation spectra such as x-ray absorption and photoemission. Configuration-interaction cluster calculations [18] and combined photoemission/ inverse-photoemission experiments [19] have pointed out the importance of the d-d Coulomb interaction U for the elec-

[2]J. G. Bednorz and K. A. Müller, Nobel Prize in 1987

[3]A. Fert and P. Grünberg, Nobel Prize in 2007

tronic structure of correlated electron systems.

These electron-electron interactions have been used to explain the insulating state of a so-called *Mott insulator*. In his model, Mott considered a lattice with one single electronic orbital on each site. Electrons are now allowed to hop between these sites and each site can be occupied by up to two electrons. However, since two electrons would feel a large Coulomb repulsion if they occupy the same site, the band will split into two: a lower lying band from electrons that occupy an empty site and a higher lying band from electrons occupying a site that is already taken by another electron. At half filling, i.e., one electron per site, the lower band is full and the system is an insulator. A first theoretical description of the transition from a Mott insulator to a metal was given within the *Hubbard model* which is the inclusion of interaction effects into a tight-binding description. The Hamilton operator of the Hubbard model is given by [20]

$$H = -t \sum_{\langle i,j \rangle} c^{\dagger}_{i\sigma} c_{j\sigma} + U \sum_{i} n_{i\uparrow} n_{i\downarrow} \tag{1.1}$$

and describes the competition between the kinetic energy (hopping) which favors the electrons to be delocalized over the lattice and the Coulomb repulsion that drives the electrons to localize on the lattice sites (Mott insulator). The first term in 1.1 describes the kinetic energy: An electron is annihilated at site j and created at site i, accompanied with the gain of the kinetic energy t, the strength of the hopping integral. $\sum_{\langle i,j \rangle}$ here is a shorthand notation for the sum over neighboring lattice sites. The second term in 1.1 includes the number operator $n_{i\sigma}$ and describes the Coulomb repulsion. For double occupation the system has to pay the on-site repulsion U. So far the Hubbard model has been exactly solved only in the limits of one dimension [21] or infinite-range hopping [22]. However, it is already very interesting to look at the limiting cases: For $U = 0$ we are back in the tight-binding model with non-interacting electrons. For $t = 0$ or $U/t = \infty$ we have no hopping at all and, thus, a lattice of isolated atoms. For $U \gg t$ the band splits into a *lower* and a *upper Hubbard band* (see above).

However, for d electron systems orbital degeneracy is important and must be taken into account. In transition metal compounds the overlap of d bands and p bands of the ligands upon hybridization is also crucial. This led to the distinction of two types of insulators, depending on the character of the first electron removal and addition states. Figure 1.1 schematically explains the difference between the electronic structure of a Mott-Hubbard (a) and a charge-transfer (b) insulator. For a Mott-Hubbard insulator, the partially filled d band is split by the d-d Coulomb repulsion U into a completely filled lower Hubbard band and an empty upper Hubbard band - the material is

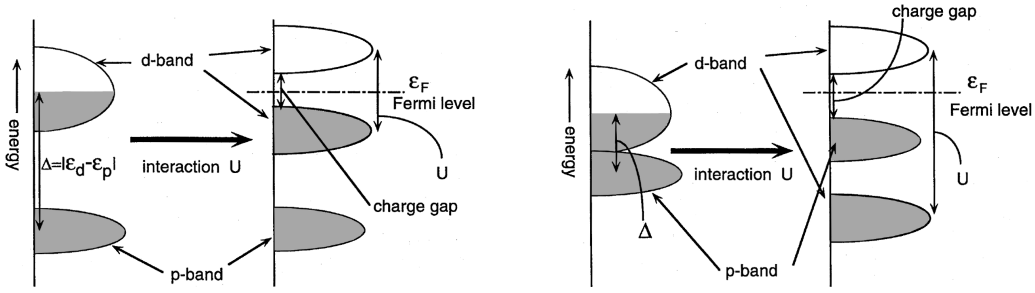

(a) Mott-Hubbard insulator (b) Charge-transfer insulator

Fig. 1.1: Schematic illustration of the electronic structure of a (a) Mott-Hubbard and a (b) charge-transfer insulator. The insulating phase is driven by the *d*-*d* Coulomb repulsion U. (Reproduced from Ref. [6])

an insulator. If on the other hand, the charge-transfer energy Δ is much smaller than U, the lower Hubbard band falls below the ligand p band. The insulating gap is then between the ligand p and the upper Hubbard band. The system is called a charge-transfer insulator. For both scenarios, Δ and U are defined in terms of energy differences between configurations as

$$\Delta = E(d^{n+1}\underline{L}) - E(d^n), \tag{1.2}$$

$$U = E(d^{n+1}) + E(d^{n-1}) - 2E(d^n), \tag{1.3}$$

where $E(d^n)$ is defined as the total energy of a d^n configuration and $\underline{L}$ denotes a ligand hole.

The concept of Mott-Hubbard and charge-transfer insulators has been generalized by Zaanen, Sawatzky, and Allen [23]. Their results is summarized in the phase diagram in Fig. 1.2. Here, compounds are classified dependent on the parameters U, Δ, and the ligand p and transition metal $3d$ hybridization parameter T. The heavy solid line ($E_{gap} = 0.5\ T$) here separates metals from insulators. In region (A) one finds Mott-Hubbard insulators. Δ is much larger than U, and thus $E_{gap} \propto U$. Charge-transfer insulators are found in region (B), where $U \gg \Delta$ and $E_{gap} \propto \Delta$. In the intermediate region (AB) Δ and U are of comparable strength. For materials falling into this region the density of states close to the Fermi level is of highly mixed ligand $2p$ and transition metal $3d$ character.

Note that electron-electron correlation effects as described above are not small or only important in very complicated systems. They already play an essential role in one of the easiest systems than one can imagine: In the hydrogen molecule (H_2) we consider two electrons in s-like orbitals, two sites, and the hopping probability t. Within a one-electron picture one finds the

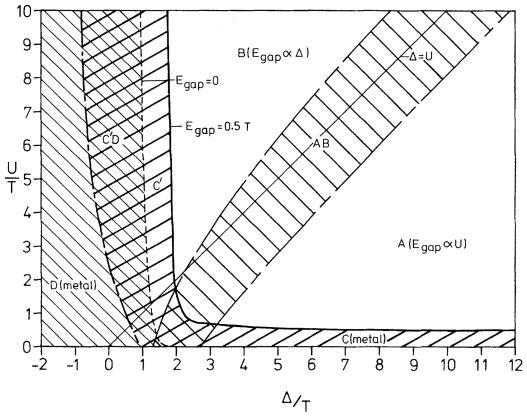

Fig. 1.2: Zaanen, Sawatzky, and Allen (ZSA) phase diagram, estimating the character of material (metal/insulator) dependent on the strength of the *d-d* Coulomb repulsion U and the charge-transfer energy Δ. The heavy solid line ($E_{gap} = 0.5\ T$) represents the separation between metals and semiconductors. (Reproduced from Ref. [23])

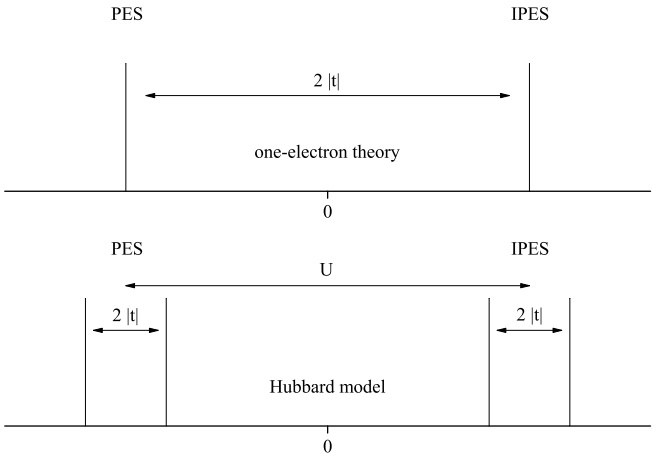

Fig. 1.3: Schematic photoemission and inverse photoemission spectra and bandgap of the H_2 molecule within one-electron theory (top) and the Hubbard model (bottom).

well-known bonding and anti-bonding states at $E_0 \pm t$. Thus, in the ground state both electrons will occupy the bonding state with opposite spins. PES and IPES spectra would yield a single peak, respectively, separated by the bandgap $E_g = 2|t|$ (see Fig. 1.3). When we treat this system within the Hubbard model with $U \gg t$, however, the bands split up in a lower and upper Hubbard band, and the PES and IPES spectra show two peaks each. Within the spectra the two peaks are separated by $\Delta E = 2|t|$, the bandgap is $E_g = U - 2|t| + 2\delta$, where $\delta = 4t^2/U$. The intensity ratio of the two peaks of the PES/IPES spectrum turns out to depend on the ratio t/U. Even though it is very simple, the hydrogen molecule model has been used to estimate t/U for real systems such as Ti_2O_3, a d^1 system with a pronounced dimerization in the crystal structure [24].

As outlined above, standard band theory is not able to fully describe the electronic structure of systems in which electron-electron correlations are important. The Hubbard model captures well the basic concept of correlations but its simplifications are severe. Another approach is to concentrate on the local electronic structure. Configuration-interaction cluster calculations which usually treat a cluster of a transition metal ion surrounded by the ligands in the correct symmetry turned out to be extremely useful to simulate excitation spectra such as x-ray absorption or photoemission [25, 26, 27]. On the other hand these kind of calculations are not *ab initio* and thus depend on parameters which have to be estimated from experiments or different theoretical approaches. Since they are impurity calculations, long range crystallographic order and intersite effects are also neglected here. New approaches like the dynamical mean-field theory (DMFT) try to combine the advantages of density-functional theory and impurity calculations: Here, the translation invariant lattice of atoms in a solid is replaced by a single impurity atom that resides in a bath of electrons. In contrast to common DFT methods here the bath is not static. The central atom fluctuates between certain atomic configurations with a certain probability. DMFT becomes exact in the limit of infinite lattice coordination. In practice, DMFT and DFT methods are often combined: Weakly correlated electrons are described within the LDA approach and strongly correlated electrons are treated using DMFT. The resulting Hamiltonian can then be solved with this LDA+DMFT method in a self-consistent way [8]. However, also (single-site) DMFT is often not able to reproduce details of experimental data such as intersite correlations or multiplet structures (cf. Chapter 3). Recent multi-site cluster and DMFT models are a another promising step towards electronic structure calculations of real materials.

1.2 Configuration-interaction cluster calculations

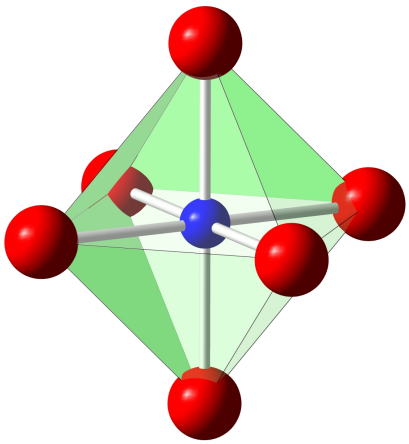

Fig. 1.4: Cluster of a transition metal cation (blue) surrounded by an octahedron of six oxygen anions (red), here in O_h symmetry. Illustrated using [28]

A cm^3 of a material in the solid state contains about 10^{24} electrons which can principally interact whith each other. This makes an exact theoretical treatment of the electronic structure of a real solid impossible. Standard band theory makes use of the translational symmetry of crystals and then treats a single electron in the mean-field potential of all other electrons. Electron-electron interactions are completely neglected here. However, despite of these rather strong restrictions, many (ground state) properties of solid state materials, in particular those of metals, can be very well understood within this one electron model.

A completely different approach is to neglect the translational symmetry of the crystal completely and to concentrate on the local correlations. In this impurity or cluster *ansatz* one restricts oneself to the description of one or a very limited number of ions residing in the surrounding of their ligands in the correct local symmetry. This restriction allows in principle to take all correlations explicitly into account, even the full atomic multiplet theory. This model is in particular interesting for systems with narrow shells, such as transition metal ($3d$) or rare earth ($4f$) compounds. Here, the spread of the radial wave functions is rather limited suggesting that the electrons may mostly retain their local character. Since within this method the ground state, low-lying excited states, and final states due to excitations can be treated on equal footing it is particulary interesting for the simulation of

excitation spectra such as photoemission or x-ray absorption. In these cases the cluster model turned out to be very powerful [25, 29].

In this work configuration-interaction cluster calculations have been performed for the simulation of experimental x-ray absorption and photoemission data. For the calculations we have used the XTLS 8.30 code by Arata Tanaka [25]. In this section some of the basic concepts of the cluster approach will be illustrated. For more detailed information we refer to Refs. [25, 26, 30, 31].

Talking about a (single-site) cluster we here refer to a transition metal ion surrounded by six O^{2-} ligands in the respective symmetry (see Fig. 1.4). When hybridization is taken into account the ground state of a d^n system can be described as:

$$|i\rangle \;=\; \alpha_1|d^n\rangle + \alpha_2|d^{n+1}\underline{L}\rangle + \alpha_3|d^{n+2}\underline{L}^2\rangle + ...,$$

where $\underline{L}$ means a ligand hole and $\sum_i \alpha_i^2 = 1$. The cluster is then treated using the following Hamiltonian:

$$\begin{aligned}
H &= H_1 + H_2, \\
H_1 &= \sum_i \epsilon_d(\Gamma_i) \sum_{\gamma_i} d^\dagger_{\gamma_i} d_{\gamma_i} + \sum_i \epsilon_p(\Gamma_i) \sum_{\gamma_i} p^\dagger_{\gamma_i} p_{\gamma_i} + \epsilon_c \sum_\xi c^\dagger_\xi c_\xi \\
&+ U_{dd} \sum_{i,j} \sum_{\gamma_i \neq \gamma_j} n_{d\gamma_i} n_{d\gamma_j} - U_{dc} \sum_{i,\gamma_i} n_{d\gamma_i} \sum_\xi (1 - n_{c\xi}) \\
&+ \sum_i V(\Gamma_i) \sum_{\gamma_i} (d^\dagger_{\gamma_i} p_{\gamma_i} + h.c.), \\
H_2 &= H_{dd} + H_{dc} + H_d(\zeta_d) + H_c(\zeta_c).
\end{aligned}$$

In H_1 the six different terms denote

1. The energy of the $3d$ orbit of the transition metal ion, where $\{\Gamma_i\}$ stands for the corresponding representations of the respective symmetry group (t_{2g} and e_g in the case of O_h) and γ_i is the basis of each representation including the spin state.

2. The energy of the ligand molecular orbit.

3. The energy of the core orbit. Here, ξ denotes the orbital and spin state of the core orbit.

4. The effective $3d$-$3d$ interaction U_{dd}.

5. The attractive core-hole potential acting on the $3d$ electron U_{dc}.

6. The hybridization between the ligand and the $3d$ orbit.

H_2 describes the full-multiplet $3d$-$3d$ (H_{dd}) and $3d$-core (H_{dc}) interaction, expressed in terms of Slater integrals, and the spin-orbit coupling in the $3d$ ($H_d(\zeta_d)$) and core ($H_c(\zeta_c)$) state. (cf. [25])

Depending on the spectrum that one wants to simulate the final state wave function then is:

$$\begin{aligned} 3d \text{ valence band PES: } |f\rangle &= \beta_1|d^{n-1}\rangle + \beta_2|d^n\underline{L}\rangle + \beta_3|d^{n+1}\underline{L}^2\rangle + \dots , \\ \text{core level PES: } |f\rangle &= \beta_1|\underline{c}d^n\rangle + \beta_2|\underline{c}d^{n+1}\underline{L}\rangle + \beta_3|\underline{c}d^{n+2}\underline{L}^2\rangle + \dots , \\ \text{XAS: } |f\rangle &= \beta_1|\underline{c}d^{n+1}\rangle + \beta_2|\underline{c}d^{n+2}\underline{L}\rangle + \beta_3|\underline{c}d^{n+3}\underline{L}^2\rangle + \dots . \end{aligned}$$

Again, $\underline{c}$ and $\underline{L}$ denote a core and ligand hole, respectively, and $\sum_i \beta_i^2 = 1$. The input parameters of a cluster calculation, therefore, typically are:

- The initial and final state configurations taken into account.
- Crystal field and hybridization, generally expressed in coefficients of an expansion in spherical harmonics. The crystal field can be, e.g., determined by LDA(+U) calculations but is often fitted to the experimental data. This is possible since for systems with a high local symmetry the number of parameters needed is only very small (only one for O_h symmetry, see below). Hybridization is usually calculated within the tight-binding model by Slater and Koster [32]. Here, the basis set used in the calculation can be significantly reduced by taking only the bonding orbitals into account.
- The Coulomb repulsion U and charge transfer energy Δ as defined in Sec. 1.1.
- The spin-orbit coupling parameters ζ_d and ζ_c.
- The Slater integrals F^2_{dd} and F^4_{dd}, and F^2_{cd}, G^1_{cd} and G^3_{cd} describing the electron-electron interaction. The Slater integrals and spin-orbit coupling parameters are usually calculated within the Hartree-Fock approximation and are tabulated for a variety of elements, e.g., in Refs. [25, 30]. In a solid the Slater integrals are partially screened and are, thus, typically reduced to about 80% of the (atomic) Hartree-Fock value [33].

In this work systems with a cubic (O_h), tetragonal (D_{4h}), or trigonal (D_{3d}) local symmetry are treated. In the O_h case the crystal field splits the $3d$ states into the well-known t_{2g} and e_g states. This splitting can be described by one single parameter only, namely, the cubic crystal field splitting $10Dq$. See Fig. 1.5. A distortion of the O_h octahedron of the ligands along one of

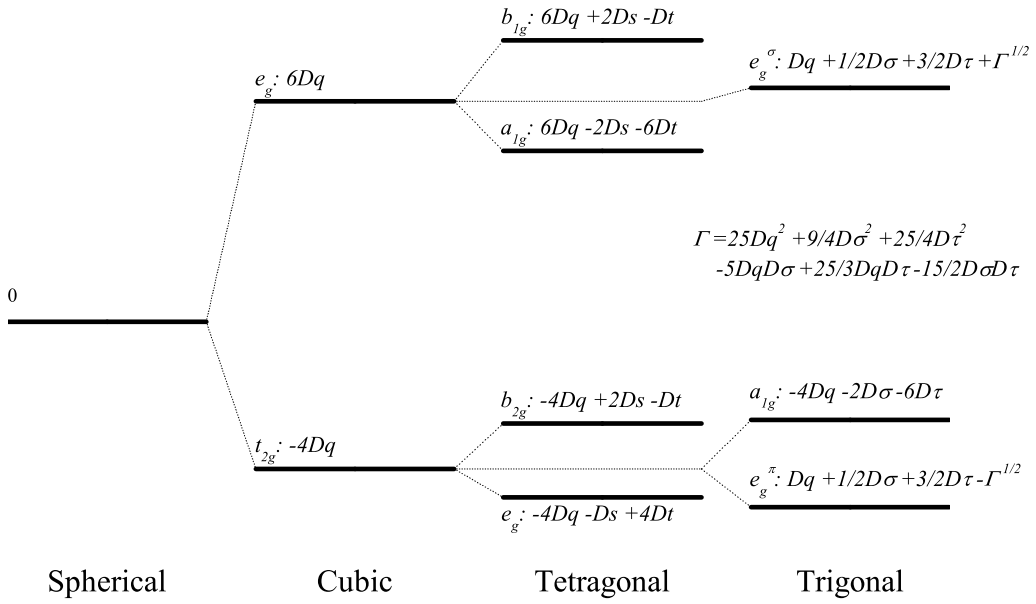

Fig. 1.5: Splitting of the d orbitals in an octahedral, tetragonal, and trigonal field (cf. [30, 34]).

the principal axes leads to a D_{4h} local symmetry in which the t_{2g} and e_g states are further split by additional parameters Δt_{2g} and Δe_g. Following Ballhausen [34], these splittings are described by introducing the parameters Ds and Dt, with $\Delta t_{2g} = 3Ds - 5Dt$ and $\Delta e_g = 4Ds + 5Dt$. When the distortion of the octahedron is applied along the [111] direction we have a D_{3d} local symmetry. Here, the trigonal crystal field lifts the degeneracy of the t_{2g} and splits these into a non-degenerate a_{1g} and a doubly degenerate e_g^π state. For the description of the crystal field splitting in trigonal symmetry three parameters, usually called Dq, $D\sigma$, and $D\tau$ is needed, as well. These parameters are often re-expressed in terms of a so-called bare trigonal field $D^0_{trig} = -3D\sigma - 20D\tau/3$ and a mixing term $V_{mix} = \sqrt{2}(D\sigma - 5D\tau/3)$ which mixes the t_{2g} and e_g states of the cubic field and, thus, leads to the formation of the e_g^σ and e_g^π states. D^0_{trig} is the crystal field splitting between the a_{1g} and e_g^π states in the absence of the stabilization of the e_g^π due to the mixing of t_{2g} and e_g states. In the XTLS 8.30 code the crystal field is expressed in terms of spherical harmonics. In this notation the complete form of the crystal field on the d orbitals in O_h, D_{4h}, and D_{3d} symmetry is [30]:

$$V_{O_h} = 21DqC_4^0(\theta,\phi) + 21\sqrt{\frac{5}{14}}Dq(C_4^4(\theta,\phi) + C_4^{-4}(\theta,\phi)), \quad (1.4)$$

$$V_{D_{4h}} = -7DsC_2^0(\theta,\phi) + 21(Dq - Dt)C_4^0(\theta,\phi) \quad (1.5)$$
$$+21\sqrt{\frac{5}{14}}Dq(C_4^4(\theta,\phi) + C_4^{-4}(\theta,\phi)),$$

$$V_{D_{3d}} = -7D\sigma C_2^0(\theta,\phi) - 14(Dq + \frac{3}{2}D\tau)C_4^0(\theta,\phi) \quad (1.6)$$
$$-14\sqrt{\frac{10}{7}}Dq(C_4^3(\theta,\phi) + C_4^{-3}(\theta,\phi)),$$

where $C_l^m(\theta,\phi) = \sqrt{\frac{4\pi}{2l+1}}Y_l^m(\theta,\phi)$.

Finally, excitation spectra are usually calculated within the dipole approximation. One has to diagonalize the initial and final state Hamiltonians and then to calculate the excitation probability to each final state. This gives a set of energies with the respective weights that, after taking a reasonable lifetime and experimental broadening into account, can be compared to experimental spectra. A comparison of the parameter set found from a fit to experimental data to parameters from other experiments or calculations is, however, not always easy. The parameters from a fit to valence band PES data can be considerably different from those from a fit to, e.g., core level PES data of the same compound. This is because in the latter the parameters are used in the presence of a core hole which can screen the strength of, e.g., crystal fields, hybridization, or hopping integrals in the final state [35, 36].

1.3 Scope of this thesis

As outlined above, configuration-interaction cluster calculations are very successful for the simulation of excitation spectra and the local electronic structure of correlated electron systems. On the other hand they are impurity calculations that neglect the translational symmetry of a real crystal and, since they are not *ab initio*, depend on parameters. One could, therefore, imagine that the parameter set that one finds by fitting a cluster simulation to experimental data of bulk samples is kind of effective in the sense that it may compensate for differences originating from shortcomings of the model. Also (single-site) DMFT treats correlations in an impurity *ansatz*, thereby neglecting all possible non-local interactions. A natural approach to test the validity of the cluster model and the physical meaning of its parameters would

be to investigate real impurity systems. Here, a single-site model should work perfectly, and parameters found from these simulations should be more meaningful. In the past, work on optical absorption spectra and electron spin resonance experiments on dilute crystalline salts of transition metals has already shown to yield valuable information about the energy levels, the ligand fields, and possible distortions [37, 38, 39, 40]. Modern spectroscopic techniques together with the availability of synchrotron radiation now allow us to investigate their electronic structure with unprecedented detail. We have, therefore, set out to systematically study the electronic structure of transition metal impurities in oxide host materials using x-ray absorption (XAS) and photoemission spectroscopy (PES). We have simulated the experimental results using a single-site cluster approach. Depending on the investigated system the impurity approach allows to study various physical effects which will be shown for different examples: The impurity approach allows to eliminate intersite or non-local effects in the electronic structure. Hence, details in the local electronic structure can be separately studied (cf. Chapter 3 and 6). It gives the possibility to prepare model systems which are not stable as bulk compounds (cf. Chapter 4). By using impurity systems instead of the stoichiometric bulk compound one can induce changes in the local environment of the transition metal ions like, e.g., the strength of the ligand field (cf. Chapter 5).

However, in order to do these experiments, we still have to overcome an experimental problem. The host materials that one would typically use for transition metal oxide impurity systems (like MgO or Al_2O_3) are very good insulators and, therefore, not suitable for electron spectroscopic experiments. They would immediately cause charging problems. Yet, we decided to prepare the impurity systems as thin films on metal substrates using molecular beam epitaxy (MBE). It is known from other studies [41] that, if the oxide film is thin enough, the conducting substrate can provide electrons to neutralize the sample charging. Furthermore, with MBE one operates far from equilibrium conditions which allows to prepare model systems which are not stable as bulk compounds. In addition, the *in situ* preparation and direct characterization using spectroscopy offers, in contrast to bulk crystal growth, an online control of the growth parameters at the experiment (stoichiometry, impurity concentration, etc.), an important aspect regarding time-limited experiments (e.g., at synchrotron facilities). For clarity and better readability, details of the electronic structure and the physical properties of the studied compounds (or of the associated stoichiometric bulk crystals) and open questions therein will be introduced and discussed in the respective chapters. In Chapter 2 the most important experimental techniques that were used for the studies in this thesis will be explained.

Chapter 2

Experimental methods

In this Chapter the experimental techniques that were used for this work will be introduced. The explanation will be very general and concentrate on the basic concepts. Details that are important for certain experiments will be dealt with in the respective chapters.

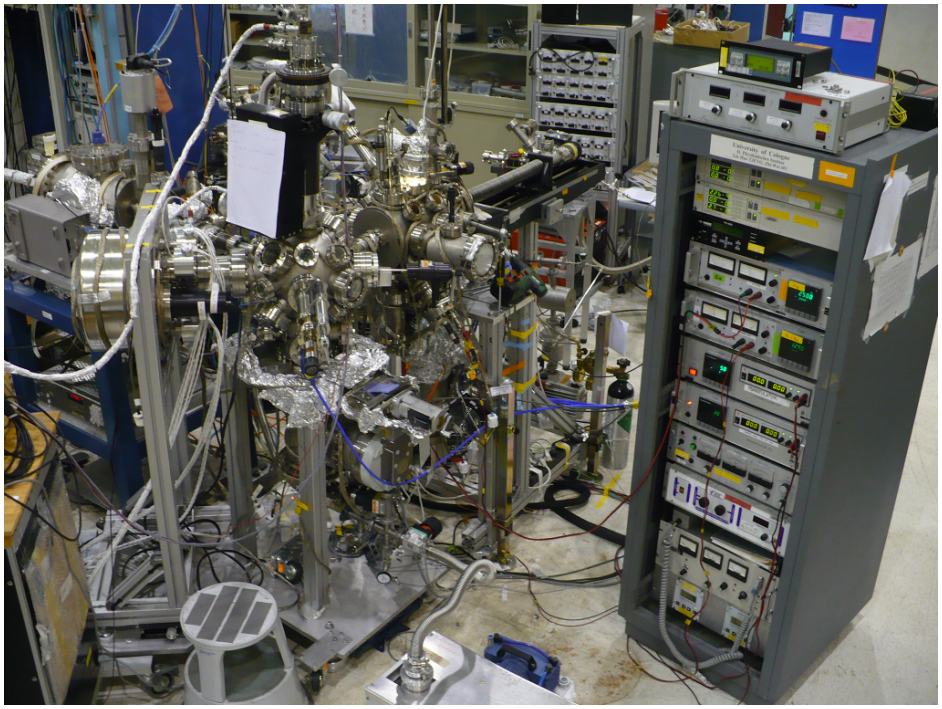

Fig. 2.1: The Cologne combined XAS/PES and Mini-MBE setup installed at the Dragon beamline of the National Synchrotron Radiation Research Center (NSRRC) in Hsinchu, Taiwan

2.1 Molecular beam epitaxy

For several reasons most of the samples studied in this thesis have been prepared as thin films. Therefore, the most important nucleation processes and growth modes of thin films, and some details of molecular beam epitaxy will be discussed in the following.

In Fig. 2.2 the fundamental atomic processes for thin film growth on surfaces are shown. When single atoms or molecules from an evaporation source hit the substrate they may diffuse on the surface until one of the other processes shown in Fig. 2.2 sets in: They can nucleate to small clusters or at special sites such as defects or steps, but they can also diffuse into the substrate or even be re-evaporated. (cf. [42])

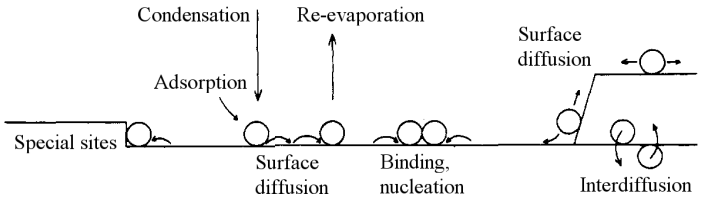

Fig. 2.2: Relevant processes in nucleation and growth of thin films on surfaces. (Reproduced from Ref. [42])

In epitaxy one distinguishes between different growth modes. The four most important are illustrated in Fig. 2.3. When the impinging atoms or molecules are stronger bound to the substrate than to each other one finds the *layer-by-layer growth* mode, in which the next layer starts to form when the previous one is already completed. In the other situation, namely the binding of the impinging particles to each other is stronger than to the substrate, the atoms nucleate as small clusters on the substrate surface and then grow into islands of the condensed phase. This situation is called *island growth*. An intermediate situation occurs if the binding energy to the substrate or the previous layers changes in a non-monotonic way: In the *Stranski-Krastanov* growth mode, the film grows in island-growth after the first monolayer(s) have formed in a layer-by-layer fashion. A possible reason for such a change in binding energy is, e.g., the reduction of stress due to lattice misfit by island formation. In reality, substrates are usually not atomically flat but, on a microscopic scale, show crystallographic imperfections such as dislocations, defects, or steps. These sites are energetically favorable for impinging atoms such that new layers start to form preferentially at steps (*step-flow growth*). Which of the above mentioned growth modes appears for a certain

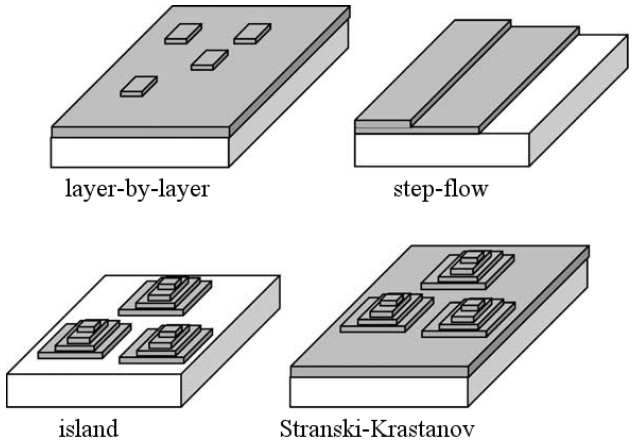

Fig. 2.3: Sketch of the relevant growth modes for thin film growth. (Reproduced from Ref. [44])

system depends on many parameters such as, e.g., material fluxes, growth temperature, substrate quality, and lattice misfit to the substrate. (cf. [43])

In molecular beam epitaxy (MBE), materials are deposited from different sources (solids, gases) onto a substrate whose temperature can usually be controlled. This is done in ultra-high vacuum conditions (base pressures of MBE systems usually are in the order of 10^{-10} mbar), allowing for several advantages of this technique. The low residual gas pressure leads to a very long mean free path of atoms or molecules in the systems. Therefore, the mass flow from evaporation sources can be regarded as a directed beam. Furthermore, it allows for very clean thin films with very little impurities and outstanding crystalline quality. In ultra-high vacuum, one also operates far from thermodynamic equilibrium conditions. For this reason the kinetics of the above mentioned growth processes on surfaces become the most important parameters. This allows to prepare systems that are usually not stable at ambient pressure or whose preparation usually requires extreme process parameters like very high temperatures or pressures as it is the case, e.g., for the preparation of EuO [45]. The use of Knudsen cells or electron beam evaporators, in which the source materials are heated by a tungsten filament or an electron beam, allows to precisely control the material fluxes. In this way, the growth of even sub-monolayer films is possible. The vacuum environment also gives the possibility for an *in situ* real-time control of the crystal growth using, e.g., reflection high energy electron diffraction (RHEED). (cf. [43])

All thin film samples for this work have been prepared using our so-called Mini-MBE setup. A photograph of this machine, mounted in combination

with our XAS/PES measurement chamber at the Dragon beamline of the National Synchrotron Radiation Research Center (NSRRC) in Hsinchu, Taiwan is shown in Fig. 2.1. The Cologne Mini-MBE setup consists of a cylindrical main chamber which can be equipped with up to three evaporators. An Ar sputter gun and a heating stage can be used for substrate cleaning and annealing. The manipulator/ sample holder allows to heat the sample to up to 500 °C. Oxygen gas can be introduced as molecular O_2 via a leak valve or, if needed, as radical oxygen ions via a thermal gas cracker. The system further features a reflection high energy electron diffraction system (RHEED) for sample surface crystal structure analysis during growth.

The Mini-MBE setup is directly connected to a combined XAS/PES measurement chamber (see Fig. 2.1), thereby allowing for an all *in vacuo* characterization of the freshly grown films. These two techniques for the characterization of the microscopic electronic structure of the sample will be explained in the following two Sections.

2.2 X-ray absorption spectroscopy

In x-ray absorption spectroscopy (XAS) one measures the photon energy dependent absorption of x-rays of a sample. This can basically be done in two different ways, as it is shown in Fig. 2.4: In the *transmission mode*, the transmitted x-ray intensity if compared to that of the incoming light. Due to the rather strong absorption of x-rays by matter, the transmission mode is often not applicable. On the other hand, one can also measure the absorption of x-rays using the *yield mode*. Here, secondary effects are used to measure the absorption cross section. Upon relaxation from the photo-excited state, fluorescence photons, Auger electrons, photoelectrons, and even ions are emitted from the sample. All of them are supposed to give a signal that is proportional to the absorption cross section [46]. The most frequently used detection mode is the so-called *total electron yield* (TEY). Here, the drain current of the sample, which is the net current of all charged particles emitted, is measured with high accuracy. The probing depth of the TEY is about 40 Å [29]. In the *energy-selected* or *partial electron yield* (PY) one measures emitted electrons within a certain kinetic energy window [47]. Depending on the selected energies, the PY is very surface sensitive and probes only a few Å of the sample. The *ion yield* mode measures only ions emitted from the surface [48]. The ion yield mode is the most surface sensitive detection technique and probes only the surface (2 Å [29]). The most bulk-sensitive detection mode is the *fluorescence yield* (FY) [49], where emitted fluorescence photons are detected using a diode, a micro-channel

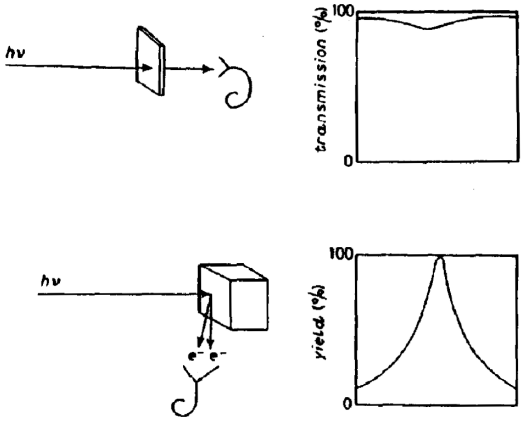

Fig. 2.4: Schematic representation of an x-ray absorption experiment performed in the transmission (top) and yield (bottom) detection mode. (Reproduced from Ref. [29])

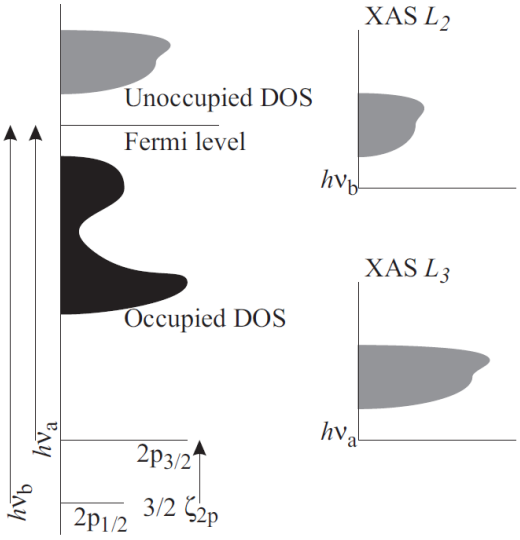

Fig. 2.5: Interpretation of x-ray absorption spectra within an one-electron picture: The experimental spectrum is a convolution of the delta-shaped core levels with the unoccupied density of states. (Reproduced from Ref. [30])

plate, or a channeltron. Since the attenuation length of photons in matter is much larger than that of charged particles, the probing depth of FY is comparably large (> 1000 Å [29]).

The basic mechanism of XAS is rather simple. When a sample is irradiated by light with an energy equal to the binding energy of a certain core level, electrons can be excited to the lowest lying unoccupied states, as it is illustrated using a single-electron model in Fig. 2.5. The interaction of x-rays with matter can here be described by Fermi's golden rule stating that the probability W of a system for a transition between initial state Ψ_i and final state Ψ_f is given by [50]:

$$W = \frac{2\pi}{\hbar}|\langle\Psi_f|\mathbf{T}|\Psi_i\rangle|^2\delta(E_f - E_i - \hbar\omega). \tag{2.1}$$

Here, E_i and E_f are the total energies of the initial and final states, and $\mathbf{T}$ is the transition operator. Re-writing the latter within the dipole approximation leads to:

$$W \propto \sum_{\mathbf{q}} \frac{2\pi}{\hbar}|\langle\Psi_f|\hat{\mathbf{e}}_{\mathbf{q}} \cdot \mathbf{r}|\Psi_i\rangle|^2\delta(E_f - E_i - \hbar\omega). \tag{2.2}$$

The dipole operator is only non-zero if the orbital quantum number of final and initial state differ by 1, and the spin is conserved, thus, $\Delta L = \pm 1$ and

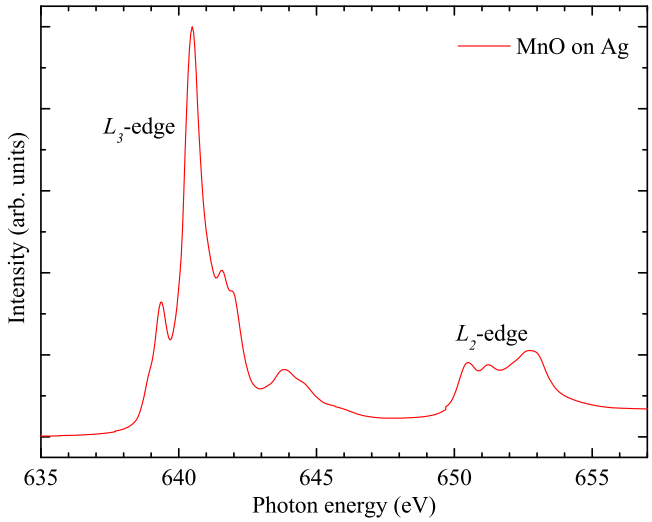

Fig. 2.6: Isotropic Mn $L_{2,3}$ x-ray absorption spectrum of MnO grown on Ag. The line shapes of the L_3 and L_2 edge are very different and the branching ratio is larger than 2/3, already indicating the breakdown of the one-electron picture here.

$\Delta S = 0$. Quadrupole transitions are some hundred times weaker and can usually be neglected in XAS. For historical reasons, in XAS the main peaks are labeled as follows: The shell of the initial state is referred to as K ($n = 1$), L ($n = 2$), M ($n = 3$) etc.. For a given shell, the transitions are numbered consecutively starting from the lowest core level. Related to this work, the most interesting transitions are the transition metal L_2 and L_3 edges, which are transitions from the spin-orbit split $2p$ ($2p_{1/2}$ and $2p_{3/2}$) to empty $3d$ final states. The energy position of these transitions, of course, depends on the binding energy of the core electron and is, thus, strongly element specific. For the $3d$ transition metals, the $2p$ core levels have binding energies between about 400 eV and 1000 eV.

Within this rather simple one-electron description and according to Fig. 2.5, we would expect the L_2 and L_3 edges of an x-ray absorption spectrum to have the same shape and an intensity ratio $I(L_3)/I(L_2 + L_3)$, the so-called branching ratio [51], of 2/3. Comparing Fig. 2.5 and Fig. 2.6, which shows the experimental Mn $L_{2,3}$ spectrum of MnO as an example, one finds that this is obviously not the case. Here, the L_2 and L_3 line shapes are very different and the branching ratio is much larger than 2/3. This already means that the one-electron picture is no valid description here. The reason for this is that one actually does not observe the unoccupied density of states in an XAS experiment. In the final state, the $2p$ core hole and the $3d$ valence

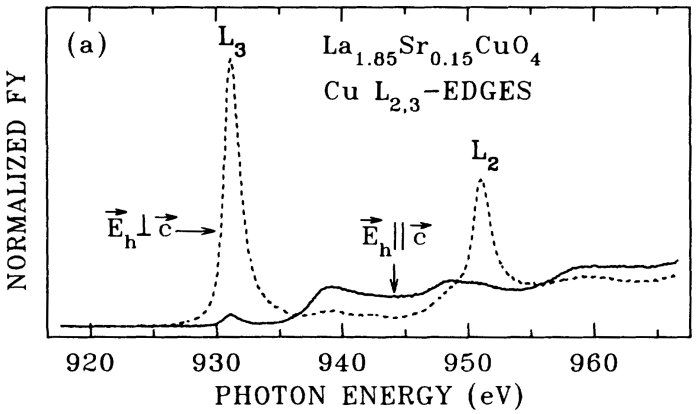

Fig. 2.7: Cu $L_{2,3}$ fluorescence yield x-ray absorption spectra of $La_{1.85}Sr_{0.15}CuO_4$ for $\mathbf{E} \perp \mathbf{c}$ (dashed line) and $\mathbf{E} \parallel \mathbf{c}$ (solid line). (Reproduced from Ref. [52])

wave function have a strong overlap. They are strongly bound and form an exciton, i.e., a bound electron-hole pair, due to the strong $2p$ core hole to $3d$ electron attraction. This strong bond of the core hole leads to almost atomiclike final states, allowing for successfully describing most features of x-ray absorption spectra within a local model. On the other hand, this also means that the one-electron picture breaks down here: An exciton can only be explained in terms of a many-electron system. The underlying atomiclike physics is, however, very well known. Core hole and $3d$ electron both can be in different orbitals, respectively, leading to a large number of possible final states. The number of possible transitions is, however, reduced significantly by the application of the dipole selection rules (see above). The full atomic multiplet theory has to be taken into account. A pure atomic description of XAS is usually not sufficient. The ligands surrounding the probed ion will react on the presence of the core hole and have, thus, to be taken into account. The exact energy position and line shape of an x-ray absorption spectrum depends on the local environment of the probed ion. This makes XAS sensitive to the valence, spin-state, and ligand field symmetry.

When linear polarized x-rays and single crystal samples are used in an XAS experiment, only electrons from orbitals which have a component parallel to the electric field vector $\mathbf{E}$ of the light can be excited. Furthermore, these electrons can only be excited to orbitals with a component parallel to $\mathbf{E}$. The intensity thus depends on the occupation of these orbitals. This effect is called linear dichroism and allows to directly probe the orbital occupation using XAS. An example where this effect can be seen in a very distinctive way is shown in Fig. 2.7. Here, the Cu $L_{2,3}$ edges of $La_{1.85}Sr_{0.15}CuO_4$ is shown

measured with $\mathbf{E} \perp \mathbf{c}$ (dashed line) and $\mathbf{E} \parallel \mathbf{c}$ (solid line). $La_{1.85}Sr_{0.15}CuO_4$ is a layered compound, belonging to the high-T_c cuprate superconductors, in which the CuO_2 planes are well separated by two LaO layers. In its tetragonal structure, the Cu ions (Cu^{2+} d^9) are surrounded by an octahedron of O ions, whose (out-of-plane) c-axis is considerably elongated compared to the a-axis. One would, therefore, expect the $d_{x^2-y^2}$ orbital to be high in energy and thus unoccupied. Looking at Fig. 2.7, this is what one can indeed see: For $\mathbf{E} \perp \mathbf{c}$ electrons can be excited to the $d_{x^2-y^2}$ hole. A strong absorption edge is found. For $\mathbf{E} \parallel \mathbf{c}$ there is no empty final state available. The absorption is consistently suppressed.

XAS also offers insight to magnetic properties of a sample. In *x-ray magnetic circular dichroism* (XMCD) circular polarized light is used on magnetized samples. Spectra taken using left- and right-circular polarized x-rays show a difference that gives information about magnetic moments of the probed ion. Sum rules have been derived [53, 54] which allow to comparably easily derive the orbital $\langle L_z \rangle$, spin $\langle S_z \rangle$, and dipole $\langle T_z \rangle$ moment from the dichroic signal.

Summarizing, XAS is a synchrotron-based, site selective tool which is sensitive to the valence, spin-state, and local environment of the probed ion. In an one-electron approximation, it measures the unoccupied density of states of a sample. For correlated systems, however, the core hole potential becomes dominant and a description including the full atomic multiplet theory is necessary.

2.3 Photoemission spectroscopy

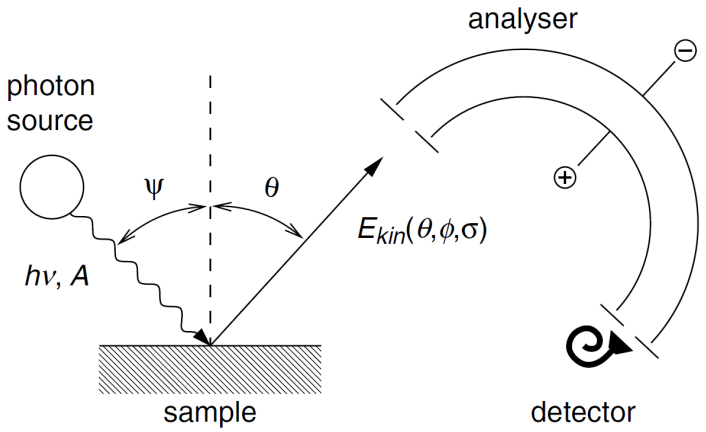

Fig. 2.8: Schematic setup of a photoemission experiment: The sample is irradiated by light of a certain energy and polarization. The kinetic energy of the emitted photoelectrons is then measured using an analyzer as a function of the emission angle θ and ϕ and the spin orientation of the electrons σ. (Reproduced from Ref. [55])

Photoemission spectroscopy (PES) has been established as one of the most important methods to study the electronic structure of molecules, solids and surfaces [55]. In contrast to XAS, which probes partially filled or empty states, PES is used to study the occupied states of a sample.

Figure 2.8 schematically shows the basic concept of a photoemission experiment. When a sample is irradiated by light of an energy $h\nu$ larger than the so-called work function Φ, electrons of the sample with binding energy E_B can be excited above the vacuum level and leave the sample (if they do not undergo inelastic scattering) with an kinetic energy

$$E_{kin} = h\nu - E_B - \Phi.$$

This is Einstein's famous equation [56], theoretically describing the photoelectric effect, which has been experimentally found earlier by Hertz [57] and Hallwachs [58]. From this rather simple equation one can already see that by measuring the kinetic energy of the photoelectrons (and knowing the photon energy and work function) one finds the binding energy of these electrons in the measured compound.

Nowadays, different kind of light sources are typically used for PES experiments. Monochromatic ultraviolet line spectra from discharge lamps are used

in ultraviolet photoemission (UPS) to study valence band states with high energy resolution. Since laboratory light sources can be used, this method is comparably easy to handle, but the very high surface sensitivity has to be taken into account. In x-ray photoemission spectroscopy (XPS) monochromatic x-ray sources such as Al or Mg K_α radiation are used as excitation sources. Compared to UPS, it is more bulk sensitive and allows to study core level spectra as well. XPS can be very well used for the chemical investigation of surfaces, thin films, and bulk samples and is for this reason also known as ESCA (electron spectroscopy for chemical analysis). Using synchrotron light as excitation source for PES allows to make use of different photoionization cross sections and to adjust the probing depth by properly tuning the photon energy. Present-day synchrotron sources also allow to use hard x-rays for PES (HAXPES), thereby enhancing the probing depth significantly, which makes bulk sensitive measurements possible and simplifies the sample preparation.

Modern hemispherical electron spectrometers are able to measure photoelectrons with an sub-meV energy resolution, and also allow to map the emission angle by using appropriate electron lens systems. Angle-resolved photoemission spectroscopy (ARPES) gives direct insight to the dispersion of valence band states.

Figure 2.9 shows in a simplified one-electron picture how a photoemission spectrum is connected to the electronic structure of the sample. Here, the photoemission spectrum is a direct image of the occupied density of states, convoluted with an experimental resolution function. However, this simplified picture is usually not valid for PES on systems where electron correlations play a role (see Sec. 1.1). Here, one should better think in terms of initial ($|i\rangle$) and final state ($|f\rangle$) configurations:

$$\begin{aligned} |i\rangle &= \alpha_1|d^n\rangle + \alpha_2|d^{n+1}\underline{L}\rangle + \alpha_3|d^{n+2}\underline{L}^2\rangle + ... \\ |f\rangle &= \beta_1|d^{n-1}\rangle + \beta_2|d^n\underline{L}\rangle + \beta_3|d^{n+1}\underline{L}^2\rangle + ..., \end{aligned}$$

for $3d$ valence band photoemission on a $3d^n$ system, where $\underline{L}$ denotes a ligand hole.

In a photoemission experiment the work function Φ, which is a characteristic of the analyzer, has to be found out experimentally by measurements on reference samples (typically scans of the Fermi edge of Ag or Au samples).

For photoemission experiments it is important to know that the photoionization cross section (the probability of a photoelectron to be emitted from a certain subshell when a photon is absorbed) can be very different for different elements and (sub-)shells, and strongly depends on the photon energy used for excitation. The photoionization cross section has been calculated and

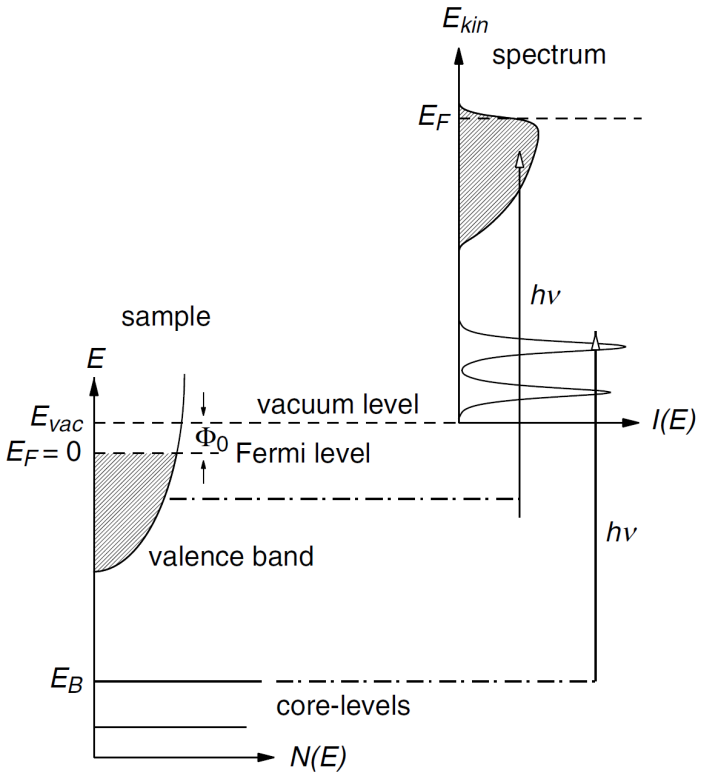

Fig. 2.9: Simplified representation of the photoemission process using an one-electron picture: An electron with binding energy E_B can be excited above the vacuum level by photons with energy $h\nu > E_B + \Phi_0$, where Φ_0 is the so-called work function. The measured energy distribution of the photoelectrons then reflects, in this simplified picture, the occupied density of states of the sample. (Reproduced from Ref. [55])

tabulated for free ions [59]. However, one needs to take into account that it can principally be different in solids [60].

In Fig. 2.10 the calculated photon energy dependence of the photoionization cross section of Ag is shown. One can see that the cross section is very different for each subshell, and that it decreases with increasing photon energy. However, the cross section of the Ag 4*d* shows a pronounced minimum at around 120 eV. This is a so-called *Cooper minimum* [61] that occurs due to vanishing matrix elements for certain transitions. As stated above, the photon energy dependence of the cross section can be exploited in experiments to enhance or suppress certain features in photoemission spectra.

The high surface sensitivity of PES is due to the strong interaction of electrons with matter. The probability that a photoelectron undergoes inelastic scattering on its way out of the sample is rather high and depends on its kinetic energy. It has been shown [62] that the resulting inelastic mean free path (IMFP) follows a so-called *universal curve* (see Fig. 2.11). This curve shows a minimum of only a few Å between around 10 and 100 eV kinetic energy. Note that the universality of the curve should be treated with attention. Even though it was experimentally shown to be valid for many el-

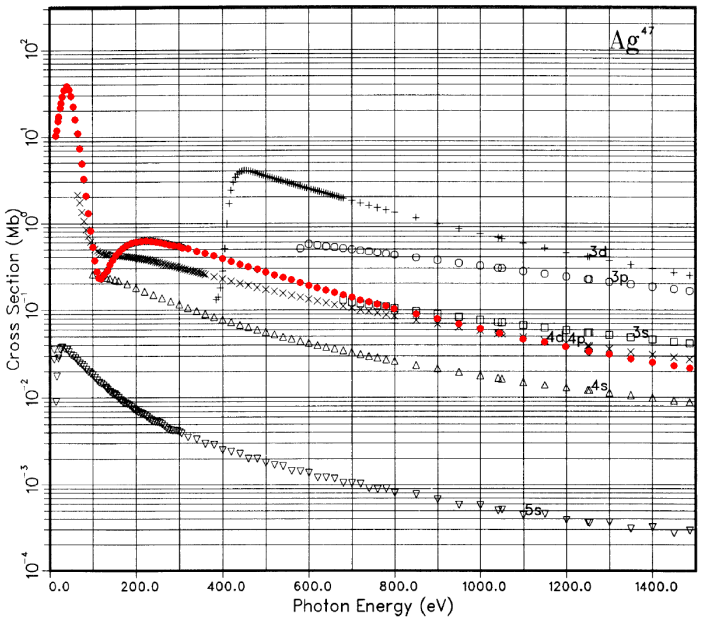

Fig. 2.10: Calculated atomic subshell photoionization cross sections of Ag. The subshell designation is marked at the end of each curve. The cross section of the Ag 4*d* subshell is highlighted in red. It shows a pronounced minimum at around 120 eV. (Reproduced from Ref. [59])

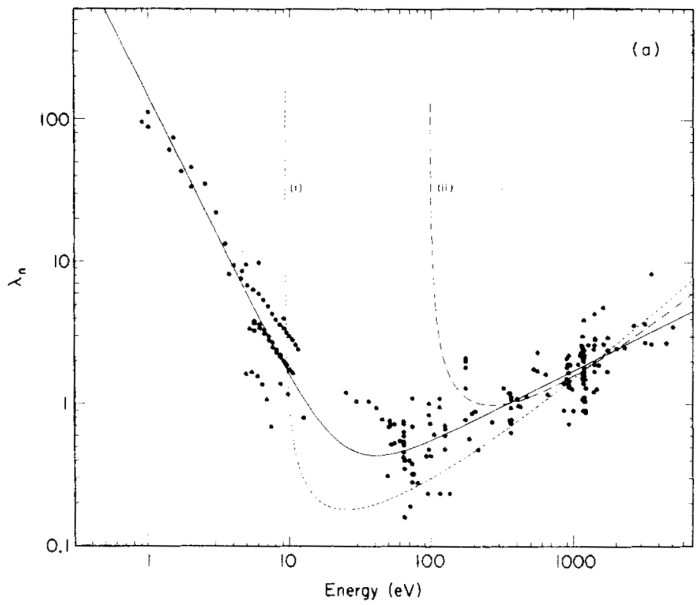

Fig. 2.11: Inelastic mean free path λ_n measured for various elements (in nm). The experimental data all approximately follow a so-called universal curve with a pronounced minimum between 10 and 100 eV. (Reproduced from Ref. [62])

ements and compounds, since the weight of the scattering processes involved strongly depends on the specific electronic structure, especially for correlated systems and wide bandgap insulators this is questionable. However, for photon energies that are typically used in conventional photoemission experiments (10 - 1500 eV) the inelastic mean free path and thus the probing depth is very short and only in the order of a few atomic monolayers. This is one of the main reasons why PES needs ultra-high vacuum conditions and a very careful sample surface preparation (like *in situ* cleaving or *in situ* thin film preparation)

Figure 2.12 shows a typical XPS overview scan of a Ag film grown on MgO by MBE *in situ*. The spectrum consists of the sharp $3s$, $3p$, $3d$, $4s$, and $4p$ core levels, the $4d$ valence band, and some Auger lines. The intensity of the lines mainly depends on the number of electrons in and the photoionization cross section of the respective subshell.

Summarizing, PES is a versatile experimental tool to study the microscopic electronic structure of gases, molecules, or solids. Depending on the measurement geometry and the photon energy used for the excitation, surface and bulk properties of the sample can be probed.

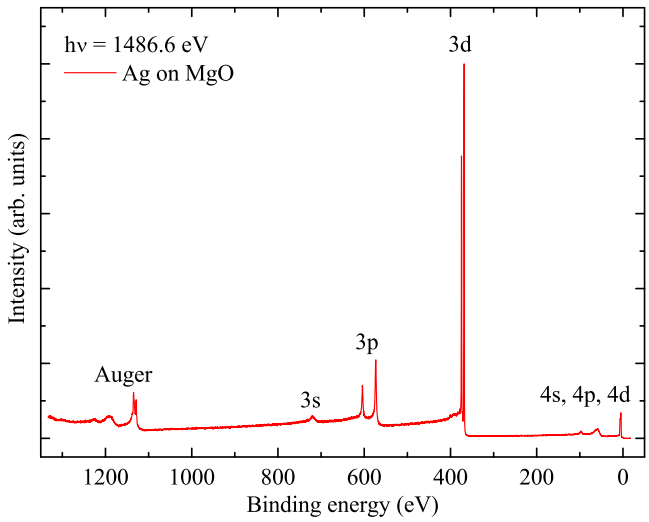

Fig. 2.12: Overview photoemission spectrum of a Ag film grown on MgO, measured using Al K_α radiation.

2.4 Synchrotron radiation

XAS and also a lot of the present-day PES experiments would not be possible without the availability of modern synchrotron light sources. Therefore, some very basic facts and concepts of these light sources will be presented here.

Synchrotron radiation occurs when a charged particle moving at relativistic speeds follows a curved trajectory [64]. It was already predicted theoretically in 1898 by Liénard [65] and finally found experimentally in 1947 by Elder et al. [66]. Since then synchrotron radiation in the x-ray and ultraviolet spectral regime has become one of the most important tools for the study of matter. The first synchrotron accelerators were only partially used for synchrotron radiation research but more for high-energy physics to study elementary particles. They are called first-generation synchrotron radiation sources. The Synchrotron Radiation Source (SRS) at the Daresbury Laboratory in Cheshire, UK was the first of the so-called second-generation synchrotron radiation sources since it was designed for and dedicated to the creation of synchrotron radiation. Modern third-generation synchrotrons are optimized for brightness by offering long straight sections for insertion devices such as undulators and wigglers. In Fig. 2.13 the layout of a typical third-generation synchrotron radiation source is shown. Electrons are accelerated to their final energy in a booster ring and finally injected into the storage ring. Dipole (bending), quadrupole, and sextupole magnets are used to guide and focus the electron beam. The synchrotron radiation that is created at

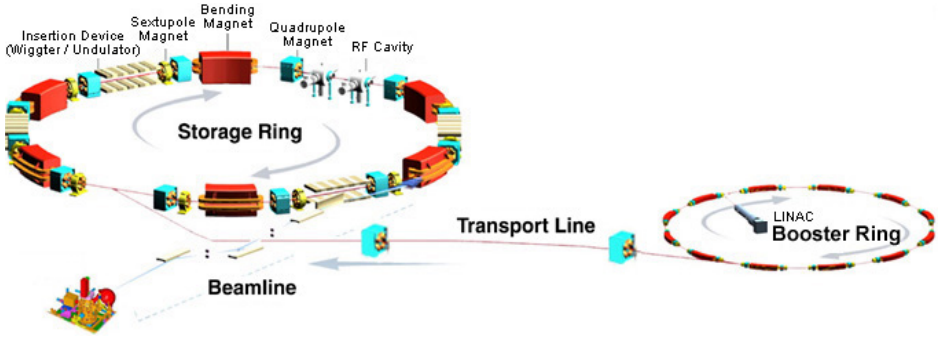

Fig. 2.13: Typical layout of a third-generation synchrotron radiation source. Electrons are accelerated to their final energy in a booster ring and then guided into the storage ring. The synchrotron radiation, which is generated at the bending magnets and insertion devices such as undulators and wigglers, reaches the experiment through so-called beamlines. (Reproduced from Ref. [63])

the bending magnets and at insertion devices in the straight sections such as undulators and wigglers is guided to the experiments through so-called beamlines. The beamlines are equipped with optics to monochromatize and focus the synchrotron light.

In Fig. 2.14 spectra of bending magnet radiation are shown for various electron energies. One can see that the spectrum is continuous with a rather sharp drop-off around a critical photon energy. This critical energy mainly depends on the electron energy and the magnetic field in the bending magnet.

Most experiments using synchrotron radiation carried out for this thesis were performed at the 11A1 Dragon beamline of the National Synchrotron Radiation Research Center (NSSRC) in Hsinchu, Taiwan. This third-generation synchrotron radiation source uses an electron energy of 1.5 GeV with a typical beam current of 300 mA. Its critical photon energy is at 2.14 keV [63]. The Dragon beamline at the NSRRC is the world's first beamline with the *Dragon design* originally designed by C. T. Chen in 1988 at the National Synchrotron Light Source (NSLS) in Brookhaven, USA [68, 69]. The Dragon design features separate and decoupled horizontal and vertical focusing mirrors, and a movable exit slit to provide both, high photon flux and high resolution (see Fig. 2.15). In addition the design allows easy operation and alignment. Six spherical gratings are used to cover a photon energy range from 10 eV to 1700 eV.

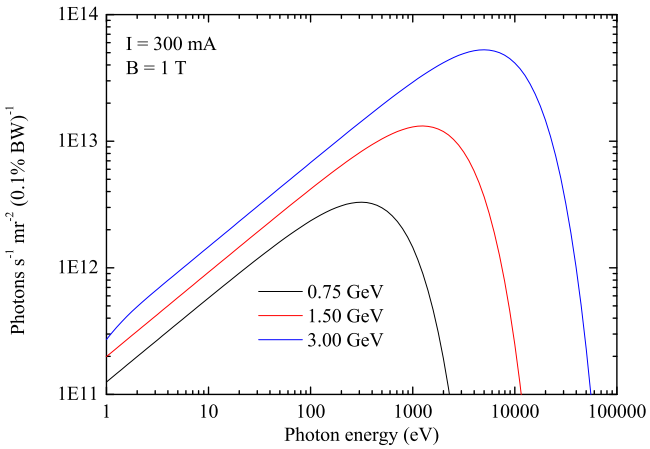

Fig. 2.14: Spectra of bending magnet synchrotron radiation for various electron energies. The radiation shows a continuous spectrum until a sharp drop-off around a critical photon energy that depends on the electron energy and the magnetic field in the bending magnet. (Calculated using [67])

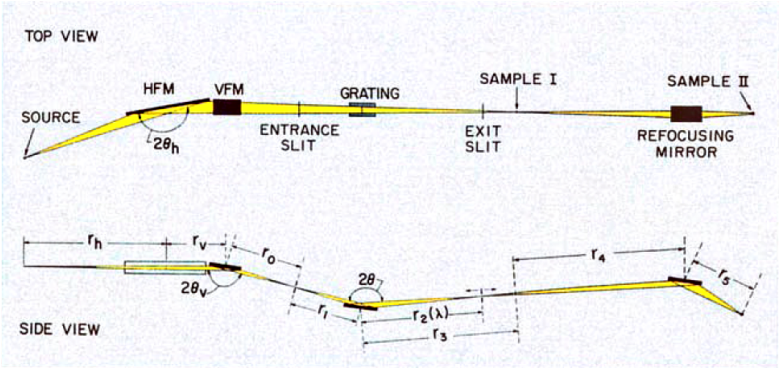

Fig. 2.15: The optical layout of the 11A1 Dragon beamline at the NSRRC (reproduced from Ref. [70]). It features separate horizontal and vertical focusing mirrors and a movable exit slit.

Chapter 3

Local correlations, non-local screening, multiplets, and band formation in NiO

Part of this work has been submitted for publication in Physical Review Letters.

NiO is a benchmark system in solid state physics. It crystallizes in the NaCl structure, has a partially filled $3d$ shell (Ni^{2+}, high-spin d^8), and is an antiferromagnetic insulator with a Néel temperature of 523 K. The superexchange interactions via the Ni-O-Ni 180° bonds are antiferromagnetic and lead to a type II antiferromagnetic order, with ferromagnetic sheets parallel to (111) planes and antiferromagnetically stacked along the [111] directions [71]. Physicists drew attention to the electronic properties of NiO since de Boer and Verwey [9] pointed out that many of the properties of the $3d$ transition metal compounds do not agree with the predictions of band theory. Standard band theory predicts NiO to be metallic. A qualitative explanation for NiO being an insulator was proposed in terms of the Mott-Hubbard model [72, 73] in which the large on-site Ni $3d$-$3d$ Coulomb interaction plays a decisive role (cf. Sec. 1.1).

An early *ab initio* attempt to fix the shortcoming of band theory was to treat NiO as a so-called Slater insulator in which the doubling of the (magnetic) unit cell allows for the existence of a gap [13, 15, 16]. However, the calculated gap of about 0.2 eV [15] turned out to be much too small: A combined photoemission (PES) and bremsstrahlung-isochromat (BIS) spectroscopy study showed that the bandgap is large, namely, 4.3 eV [19] and established thereby the correlated nature of NiO. The inclusion of a self-

interaction-correction (SIC) or Hubbard U term to the density-functional formalism may provide a justification for the magnitude of the experimental bandgap [17, 74].

Yet, one of the most direct methods to critically test the accuracy of the different approaches, is to determine the excitation spectrum associated with the introduction of an extra particle into the system [76], e.g., the Ni $3d$ one-electron removal (photoemission) spectrum in the case of NiO.

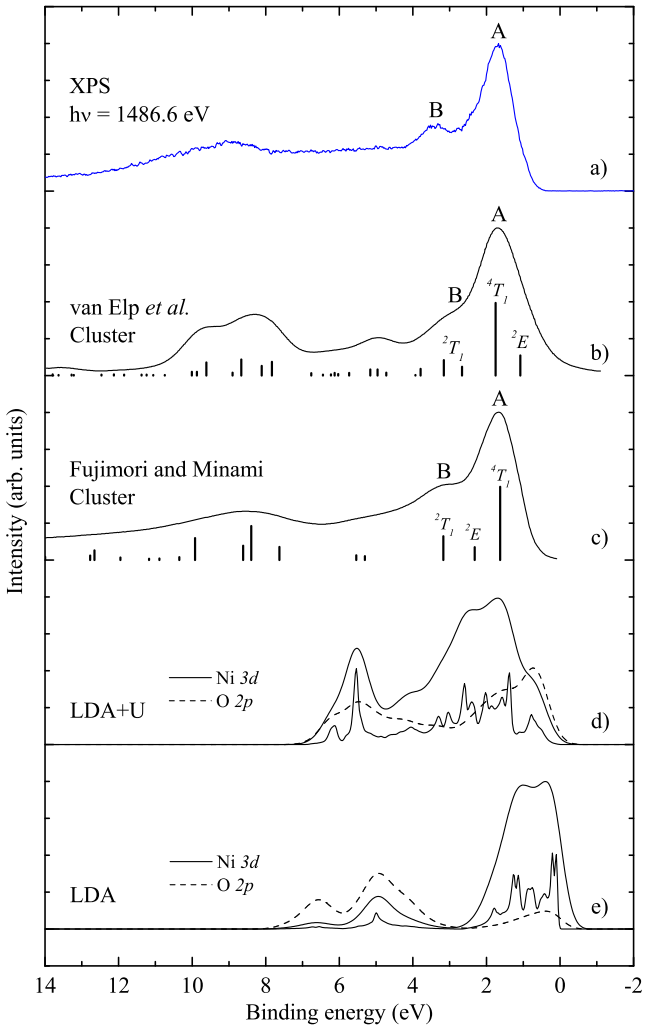

Fig. 3.1: Valence band XPS (1486.6 eV) spectrum of an *in situ* cleaved NiO single crystal. The results of two single-site cluster calculations (reproduced from Refs. [18] and [75]), and LDA and LDA+U calculations are also included for comparison.

This is shown in curve (a) in Fig. 3.1 which displays the valence band x-ray photoemission spectrum (XPS, $h\nu = 1486.6$ eV) of an *in situ* cleaved NiO single crystal. This spectrum represents essentially the Ni $3d$ spectral weight since the photoionization cross section of the O $2p$ is relatively small [59]. The valence band spectrum consists of two main parts, namely, a leading edge (A) at around 1.7 eV with a shoulder (B) and a broad high binding energy satellite around 9 eV. The main line has predominantly $d^8\underline{L}$ character ($\underline{L}$ denotes a hole in the oxygen ligands). The Ni $3d$ one-electron removal spectrum mainly consists of three states. The $3d^8$ ($^3A_2$) ground state has two spin-up electrons in the e_g orbitals. The removal of any of these two results in a ^2E state. Removing one of the three spin-up or spin-down t_{2g} electrons leads to low-spin $^2T_1$ and high-spin $^4T_1$ states, respectively. Due to hybridization in the ground state there is another possible ionization state, namely, a state with ^4E symmetry. It is rather accepted that the main line of the NiO Ni $3d$ valence band spectrum is due to the $^4T_1$ state. From curve (e) in Fig. 3.1 one can clearly observe that the Ni $3d$ density of states as calculated by band theory (in the local density approximation, LDA) does not match the experimental XPS spectrum at all: It has a Fermi cut-off and the line shape is completely different. The inclusion of the Hubbard U in the calculations (LDA+U) does not solve the line shape problem, see curve (d).[1] All this demonstrates the shortcomings of mean-field theories to describe spectra associated with the fundamental one-particle Green's function of the system [74, 78]. An impurity calculation, taking the input parameters from the LDA+U DOS (not shown here), also gives no convincing agreement with the experiment [79].

A completely different approach is to give up the translational symmetry of the system in order to focus on the local correlations and, especially, the dynamics of the propagation of the injected particle. Curve (c) of Fig. 3.1 shows the Ni $3d$ spectral weight from an early cluster configuration-interaction calculation by Fujimori and Minami [18], which also includes the full atomic multiplet theory. The agreement with the experimental spectrum is extremely good. Nevertheless, a later cluster calculation by van Elp *et al.* [75] arrived at a less satisfactory result: Peak B has almost disappeared in the calculation, see curve (b). Additionally, the ^2E-$^4T_1$ splitting is too large compared to our high-resolution experimental data. The prime motivation to use a different set of model parameters in this study was to infer that the first ionization state is low spin (^2E) [80] rather than the Hund's rule high-spin ($^4T_1$), analogous to the case of Zhang-Rice singlets in the cuprates [81, 82]. This is consistent with the magnetic behavior of Li doped NiO

[1] LDA and LDA+U calculations done by Hua Wu using the WIEN2K code [77].

[80, 75]. Extra holes doped in NiO behave as if low-spin Ni^{3+} is formed. Recent developments combining LDA with dynamical mean-field [83, 84, 85, 86] or GW approaches [87] yield Ni $3d$ spectral weights which deviate in important details from the experimental spectrum. These discrepancies between the experiment and the later theoretical simulations [75, 83, 84, 85, 86] do not provide confidence that one has made progress in understanding the nature of the first ionization state.

The issues that we need to address now are threefold. First of all we have to establish whether the XPS valence band spectrum in Fig. 3.1 is truly representative for bulk NiO. A detailed look at the $3d$ one-electron removal spectral weight reveals that the main line of the spectrum exhibits a high binding energy shoulder at about 2 eV (cf. features A and B in the top curve of Fig. 3.1), similar to that in the Ni $2p_{3/2}$ core level PES, which has been shown to be an intrinsic feature of NiO [88]. Neither the single-site cluster approach [75] nor the DMFT calculations [83, 84, 85, 86] are able to reproduce this shoulder in the Ni $3d$ spectral weight. There are reports in the literature claiming that certain satellite peaks in the Ni $2p$ spectrum are due to surface effects [89, 90, 91, 92]. Second, we have to determine to what extent a single-site many body approach can be utilized to describe the electronic structure of NiO for which band formation is also essential. For the Ni $2p_{3/2}$ core level PES it has been shown by CI calculations, which apply a cluster with more than only one Ni site, that the extra shoulder is related to non-local excitations which involve screening by electrons coming from ligands around neighboring Ni sites [88]. Here, the shoulder is caused by a $\underline{c}d^9$ final state leaving the neighboring Ni site in a $d^8\underline{L}$ configuration. $\underline{c}$ and $\underline{L}$ denote a core and ligand hole, respectively. This is supported by the results of experimental studies on ultra-thin layers of NiO epitaxially grown on MgO [93] and Ni impurities in MgO thin films where the shoulder is absent due to the lack of Ni neighbors [94]. For valence band spectra, however, it is not clear how such non-local screening effects (or their analogon for valence bands) enter the spectra. Third, we need to identify the nature of the first ionization state in the framework of a local *ansatz*. To this end we measured the valence band of NiO utilizing the more bulk-sensitive hard x-ray photoelectron spectroscopy (HAXPES) and we investigated experimentally the electronic structure of NiO impurities in MgO. We also compare our experimental data to recent LDA+DMFT results showing that they also match the NiO impurity rather than the bulk spectrum. In an attempt to explain the existence of the shoulder in the bulk system we propose a non-local screening mechanism for the valence band PES of NiO, analogous to that explaining the shoulder in the Ni $2p_{3/2}$ core level XPS.

The measurements on $Ni_xMg_{1-x}O$ were performed using our combined

PES and XAS setup at the 11A1 Dragon beamline [68, 69] of the NSRRC in Hsinchu, Taiwan. The thin film samples were prepared by means of MBE *in situ*. XAS spectra were recorded using the TEY detection in the normal light incidence. The photon energy resolution at the Ni $L_{2,3}$ edges ($h\nu \approx$ 850-875 eV) was set at about 0.35 eV. PES spectra were recorded using a Scienta SES-100 electron energy analyzer. For the PES measurements using 140 eV photons the overall energy resolution was set to about 150 meV. XPS data ($h\nu$ = 1486.6 eV) on bulk NiO were recorded in the normal emission geometry using a Vacuum Generators twin crystal monochromator Al-K_α source, with an overall energy resolution set to 0.35 eV. For the bulk sample we have used a commercially available single crystal from CrysTec GmbH. Just before measurement the bulk samples were cleaved *in vacuo* to expose a clean, mirror-like (100) surface. HAXPES spectra ($h\nu \simeq 6.5$ keV) of bulk NiO were taken at the BL12XU Taiwan beamline of the 8 GeV Super Photon Ring (SPring-8) in Hyogo, Japan using a MBS A-1HE electron energy analyzer. For the HAXPES measurements the overall energy resolution was set to 0.35 eV. In all cases the base pressure of the UHV system was below 3×10^{-10} mbar.

To interpret and understand the spectra, we have performed simulations using the well-proven configuration-interaction cluster model [25, 29, 95]. Within this method we have treated the Ni impurity site as an NiO_6 cluster which includes the full atomic multiplet theory and the local effects of the solid. It accounts for the intra-atomic 3*d*-3*d* and 2*p*-3*d* Coulomb interactions, the atomic 2*p* and 3*d* spin-orbit couplings, the local crystal field, and the O 2*p*-Ni 3*d* hybridization. This hybridization is taken into account by adding the $3d^{n+1}\underline{L}$ and $3d^{n+2}\underline{L}^2$ states to the starting $3d^n$ configuration, with $n = 8$ for Ni^{2+}. The simulations have been carried out using the program XTLS 8.3 [25], with parameter values typical for a Ni^{2+} system [96].

The $Ni_xMg_{1-x}O$ samples were grown on top of mirror-polished Ag foil which was cleaned *in situ* by several sputtering and annealing cycles before growth. High purity Mg and Ni metal were co-evaporated from effusion cells in an oxygen atmosphere of about 5×10^{-7} mbar. The substrate was kept at room temperature during growth. Polycrystalline films were used to eliminate the influence of emission angle dependent effects in the PES spectra. The use of thin films grown on a metal substrate is needed here to overcome the problem of specimen charging which readily occurs in PES and XAS experiments on large bandgap insulators such as MgO. The $Ni_xMg_{1-x}O$ films were capped by 2 monolayers of pure MgO (x=0) in order to prevent the surface termination to have an effect on the local electronic structure of the Ni impurity. However, we still have to solve another problem, namely, that for the valence band PES measurements the presence of the Ag 4*d* signal

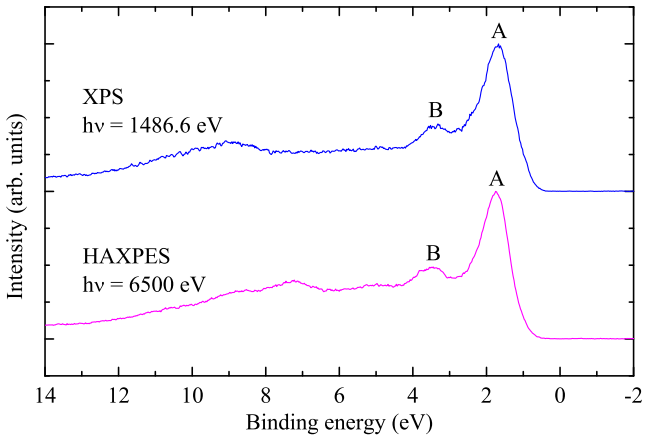

Fig. 3.2: Valence band photoemission spectra of an *in situ* cleaved NiO single crystal recorded using 1486.6 eV (XPS) and 6500 eV (HAXPES) photons.

will contaminate the small Ni 3*d* that we would like to record. Our solution is to make use of the so-called Cooper minimum in the photoionization cross section of the Ag 4*d* [59, 97]. By using 140 eV photons [97] we can suppress the Ag 4*d* signal and we can obtain signals representative for the O 2*p* valence band of the MgO and for the Ni impurity as well. The film thickness was then chosen thick enough to sufficiently suppress the Ag 4*d* signal but on the other hand thin enough to prevent charging effects. We found this to be the case for a film thickness of about 100 Å.

In Fig. 3.2 we show a comparison of the valence band photoemission spectra of a freshly cleaved NiO bulk crystal, taken with a photon energy of 1486.6 eV (XPS) and 6500 eV (HAXPES). To our knowledge, the HAXPES valence band spectrum of NiO has not been reported in the literature so far. By increasing the photon energy we increase also the kinetic energy of the outgoing photoelectron and, thus, also the inelastic mean free path. One can estimate that the probing depth is then enhanced from about 15 Å to roughly 80 Å [98]. Comparing both experimental spectra we observe that they are very similar. The intensity ratio between the different features in the spectrum, especially that of the main peak A and its shoulder B, hardly changes. We, thus, conclude that the XPS data as displayed in Figs. 3.1 and 3.2 is representative for the NiO bulk material and that the contribution of surface effects [89, 90, 91] can be safely neglected. To be specific: Peak B is intrinsic for bulk NiO. We would like to note that increasing the photon energy from 1486.6 eV to 6500 eV does not alter much the Ni 3*d* character of the spectrum. The O 2*p* photoionization cross section relative to that of the

Ni $3d$ remains very small, it changes from 1/13 to only 1/10 [99], meaning that peak B truly belongs to the Ni $3d$ spectral weight and does not originate from the O $2p$, as suggested by recent LDA+DMFT calculations [85]. However, between 6 and 12 eV binding energy the XPS and HAXPES valence band spectra differ slightly. This difference appears due to the (slightly) enhanced O $2p$ contribution in the HAXPES data. Indeed, the difference of the HAXPES and XPS spectra peaks at the same positions as the O p removal spectral weight as measured using O K_α x-ray emission spectroscopy [79, 100]. From the comparison to the HAXPES spectrum we found that, despite of the smaller probing depth, together with proper sample preparation normal emission XPS data represent the bulk electronic structure of NiO.

Before we turn to the valence band PES of a NiO impurity in MgO we have to confirm the quality and stoichiometry of our impurity sample. Figure 3.3 shows the Ni $L_{2,3}$ XAS spectra of bulk NiO and of a $Ni_{0.05}Mg_{0.95}O$ thin film. Impurity and bulk spectrum exhibit an almost identical line shape, as is the case for that of the Ni $2p$ [94]. Tiny differences are most likely due to small differences in the strength of the local crystal fields and due to the influence of an exchange field in the condensed system [101]. We compare the experimental data to a simulation of the atomiclike $2p^6 3d^8$-$2p^5 3d^9$ transition using a single-site cluster model. We find an excellent agreement of the experimental data sets and the simulation. These findings

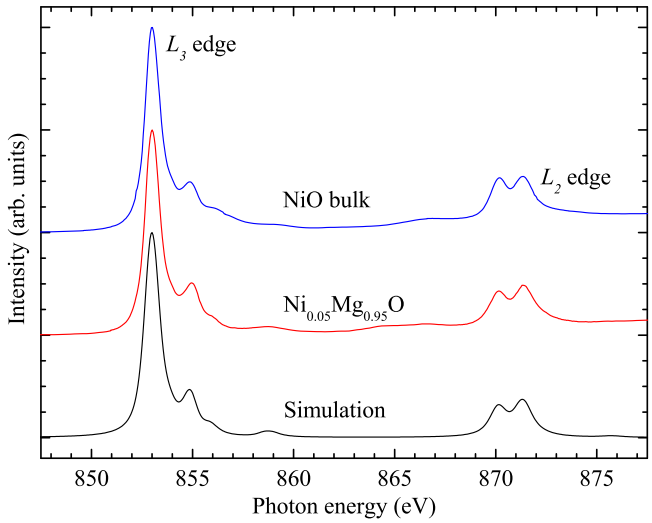

Fig. 3.3: Ni $L_{2,3}$ XAS spectra of bulk NiO and of $Ni_{0.05}Mg_{0.95}O$ compared to the result of a single-site cluster simulation. Parameters for the simulation are explained in the text.

let us firmly conclude that our bulk sample is indeed stoichiometric NiO and that the Ni impurities in the MgO film are all in the 2+ valence state, without any indication for the presence of Ni in other valence states.

We are now ready to investigate the valence band photoemission spectrum of the $Ni_{0.05}Mg_{0.95}O$ impurity system which is shown in Fig. 3.4 together with the spectrum of an MgO reference thin film grown simultaneously under identical oxygen and substrate conditions. The spectra are normalized to their O 2*s* core level intensities. Both are dominated by the O 2*p* valence band, yet, there are clear differences between them due to the presence or absence of the 5% NiO impurity. The difference spectrum multiplied by a factor of 6 is given by the red curve in Fig. 3.4. This curve represents the Ni 3*d* spectral weight of the NiO impurity. Remarkable is that it is different from the spectrum of bulk NiO as shown in Figs. 1 and 2. The impurity spectrum lacks specifically peak B which is prominently present in the bulk spectrum.

The bottom curve in Fig. 3.4 shows the Ni 3*d* one-electron removal spectrum from the cluster calculation. The agreement with the experiment is very satisfactory. In order to achieve this, we have started the calculations by using parameter values which were suggested from earlier studies on NiO [25, 75, 102, 103]. We then fine-tune the parameters describing the octahedral crystal and ligand fields, and also the difference between the Hubbard

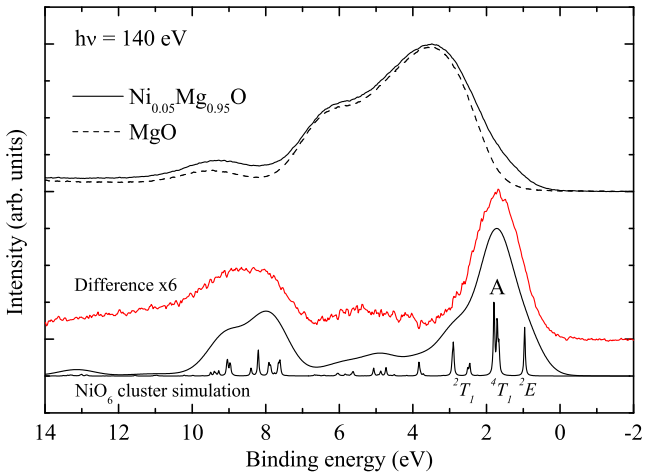

Fig. 3.4: Extraction of the NiO impurity valence band spectrum: Valence band PES (140 eV) spectra of $Ni_{0.05}Mg_{0.95}O$, an MgO reference, and the resulting difference spectrum. Also included is the result of a single-site cluster simulation. Parameters for the simulations are explained in the text.

U and the O $2p$-Ni $3d$ charge transfer energy [96]. The crucial issue here is to obtain a main line (peak A) without having another feature appearing at about 2 eV higher energies (peak B) as was the case in the simulations by Fujimori and Minami [18] and by van Elp *et al.* [75]. This has implications for the energetics of the states making up the valence band as we explain in the following.

A detailed look at the cluster calculations displayed in Fig. 3.1 shows that peak A is given by the ${}^4T_1$ final state of the Ni $3d^7$ multiplet structure while peak B is due to the ${}^2T_1$. Avoiding the appearance of peak B means that the energy splitting between these two states must be made smaller, e.g., 1 eV or less. This is what we have done in our simulation in Fig. 3.4, using different but equally reasonable parameter values [96]. The consequences for the physics are, yet, quite far reaching. Given the fact that various XAS studies find an effective octahedral crystal and ligand field splitting of about 1.65 eV [102, 103], i.e., the splitting between the isospin ${}^2T_1$ and ${}^2E$ states, we arrive at the conclusion that the ${}^2E$ must be lower in energy than the ${}^4T_1$ by 0.65 eV or more. This is what we read from our results in Fig. 3.4. In other words, our impurity study provides the spectroscopic evidence that the first ionization state has a compensated-spin character rather than the Hund's rule high-spin. This in turn justifies that the ground state of a hole doped NiO system may indeed be low-spin in nature [80].

We now return to the problem of the bulk NiO valence band spectrum. Fig. 3.5 shows the Ni $3d$ spectral weight taken with XPS and compares it with the spectra of the NiO impurity and of the single-site LDA+DMFT calculation [85]. For the bulk spectrum we have chosen for the XPS data here since, as we have seen above, it reflects best the Ni $3d$ spectral weight of the bulk. One can clearly observe that peak B is absent in the impurity as well as in the Ni $3d$ spectral weight of the single-site calculation. In fact, one could infer that the calculation reproduces quite well the impurity spectrum, with perhaps some discrepancies due to the incomplete implementation of the multiplet structure of the on-site Coulomb interactions. Yet, the discrepancy with the bulk spectrum strongly suggests that the origin of peak B must be sought in non-local correlations, i.e., effects which cannot be included in a single-site approach.

Our suggestion is that peak B is due to non-local screening processes involving the formation of low-energetic coherent many body states on neighboring NiO clusters, which are of the ${}^2E$ type as we have shown above. The mechanism is similar as it was proposed earlier for the Ni $2p$ core level spectrum of bulk NiO [88], but the application of it for the valence band requires a careful analysis. If one starts to interpret the valence band of bulk NiO from a local or impurity *ansatz*, then one has to make an estimate about

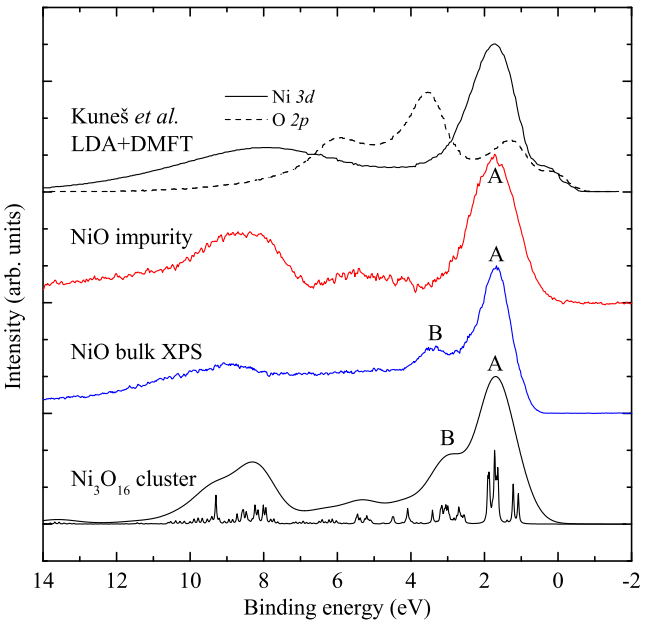

Fig. 3.5: Comparison of the valence band PES spectra of bulk NiO and of a NiO impurity in MgO. Also included is the simulated Ni $3d$ and O $2p$ spectral weight of the NiO valence band from a LDA+DMFT calculation (top, reproduced from Ref. [85]) and the result of a three-site Ni_3O_{16} configuration-interaction cluster calculation (bottom).

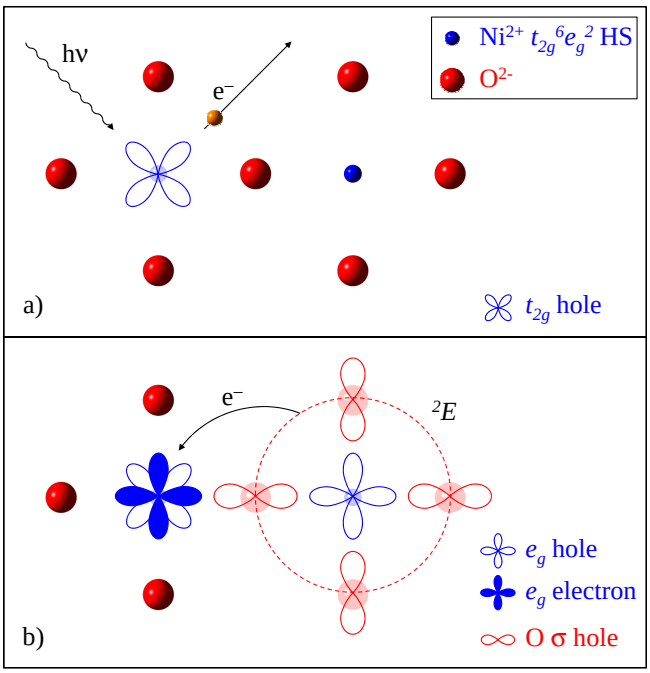

Fig. 3.6: Non-local screening in valence band photoemission of NiO: (a) Creation of the atomiclike (quasi core) ^4T hole state by the photoemission process. (b) Screening by a next nearest neighbor NiO_6 cluster producing a coherent Zhang-Rice singlet-like (ZRS) hole state there.

how well each of these states will retain their local character upon band formation. This is in particular difficult to calculate for the ^2E state, which is a state in which a hole is injected in an e_g orbital starting from the $3d^8$ $^3A_2$ ground state [103]. This hole can be expected to readily propagate in the lattice since the hopping between the Ni $3d(e_g)$ and O $2p(\sigma)$ orbitals are rather large [75, 88], yet, it may leave behind an energetically costly wake of wrong spins in the antiferromagnetic lattice. In any case, it would not be meaningful to describe its band formation as a low-energy screening process involving neighboring ^2E states [104].

However, for the main peak of the bulk NiO spectrum, i.e., the $^4T_1$ state, we infer that we can make a meaningful approximation by using the coherent ^2E screening model. The $^4T_1$ consists of a hole injected into the t_{2g} orbital, and its ability to move is rather limited since the overlap between the Ni $3d(t_{2g})$ and O $2p(\pi)$ is small. One could consider the $^4T_1$ as a localized quasi core state. We then can invoke the non-local screening process as follows: After the creation of the $^4T_1$ state, an e_g electron from a neighboring NiO cluster hops onto the Ni site, leaving behind a coherent ^2E hole state on

that neighbor. The qualitative idea is sketched in the cartoon in Fig. 3.6. In a first step (a) the atomiclike (quasi core) $^4T_1$ hole state is created by the photoemission process. This t_{2g} hole can then be screened by an electron from the $d_{x^2-y^2}$ orbital of a next-nearest neighbor, 180°-bond Ni site (b), leaving the latter in a coherent Zhang-Rice singlet-like hole state [81]. These two states are energetically almost degenerate [88], and the Ni $3d(e_g)$ and O $2p(\sigma)$ hybridization between them is then strong enough to produce two peaks: Not only the main peak A but also the satellite peak B.

This kind of screening mechanism requires the antiferromagnetic alignment of the involved neighboring Ni site. To show this we take a closer look at the involved electron removal states and the possible screening channels. In the following discussion the indices $\uparrow$ and $\downarrow$ denote the respective spin state. As shown above, the first two ionization states of the NiO $3d^8$ configuration are the ^2E and $^4T_1$ states. The ^2E has the $t_{2g}^6 e_{g\uparrow}$ (d^7) configuration. This configuration can hybridize with the oxygen ligands via the hopping of a spin-up or spin-down electron with e_g symmetry, leading to a $t_{2g}^6 e_{g\uparrow}^2 \underline{L}_\uparrow$ or $t_{2g}^6 e_{g\uparrow} e_{g\downarrow} \underline{L}_\downarrow$ ($d^8\underline{L}$) configuration (classical, local screening). These two can principally also be screened via non-local channels, namely, via $t_{2g}^6 e_{g\uparrow}^2$–$t_{2g}^6 e_{g\uparrow}$ and $t_{2g}^6 e_{g\uparrow} e_{g\downarrow}$–$t_{2g}^6 e_{g\downarrow}$ configurations. The two channels require a ferromagnetic and antiferromagnetic alignment of the involved Ni neighbor, respectively. In the antiferromagnetically ordered state, all Ni neighbors to be considered have an antiferromagnetic spin orientation. Thus, for $T < T_N$ only the "classical", antiferromagnetic non-local screening channel [88] is active. For $T > T_N$, the ferromagnetic non-local screening channel also contributes. The resulting width of the ^2E band becomes not necessarily narrower. The $^4T_1$ ionization state, however, has a $t_{2g\uparrow}^3 t_{2g\downarrow}^2 e_{g\uparrow}^2$ (d^7) configuration and can locally only be screened via the $t_{2g\uparrow}^3 t_{2g\downarrow}^2 e_{g\uparrow}^2 e_{g\downarrow} \underline{L}_\downarrow$ ($d^8\underline{L}$). Alternatively, a non-local $t_{2g\uparrow}^3 t_{2g\downarrow}^2 e_{g\uparrow}^2 e_{g\downarrow}$–$t_{2g}^6 e_{g\downarrow}$ screening channel is possible, thereby requiring the antiferromagnetic alignment of the neighboring Ni site involved. Since this is the only non-local screening channel here, we expect a narrowing of the $^4T_1$ bandwidth for $T > T_N$ where this channel is suppressed by the breakup of the magnetic order. Indeed, in a very recent high-temperature HAXPES study on bulk NiO we found a substantial narrowing of the respective lines of the valence band and the Ni $2p$ core level [105].

To confirm our assignments, we have also performed a Ni_3O_{16} cluster calculation consisting of three edge-shared NiO_6 octahedra. While all the O $2p$ and Ni $3d$ orbitals are included for the NiO_6 octahedron in the center where the photo-excitation takes place, those on the other parts of the cluster are replaced by a reduced basis set using the method in Ref. [106]. The results are displayed in Fig. 3.5 and demonstrate the presence of both peaks A and B. Note that we have used the same parameters as for the single-site

calculation which produces only peak A, see Fig. 3.4. We also note that the energy difference between peaks A and B is somewhat smaller and the intensity of peak B is slightly larger than those of the experiments. This can be explained by the fact that the number of neighboring Ni sites is only two in the Ni_3O_{16} cluster: the energy difference will increase and the intensity of peak B will decrease for a larger number of neighboring sites [106].

These findings, together with the experimental results presented here, let us feel confident that the, so far only qualitative proposed mechanism is indeed important for the one-electron removal spectrum of NiO. More quantitative evidence from theory is, therefore, highly desired. A multi-site cluster calculation has been carried out to describe this process quantitatively in the cuprates [106]. Recent multi-site DMFT approaches ("Cluster DMFT", "Plaquette DMFT") have already shown that the inclusion of short range intersite correlations strongly modifies the shape of spectral functions [107, 108]. This techniques might, in consequence, be good candidates for a proper *ab initio* inclusion of the non-local screening. An extended multi-site CI cluster calculation, even if technically expensive, would be another alternative.

We have succeeded to determine reliably the Ni $3d$ valence band spectra representative for bulk NiO as well as for NiO as an impurity system. Standard band theory, CI cluster calculations, as well as state-of-the-art LDA+DMFT models fail to reproduce the experimental line shape in detail. From the impurity data we are able to extract the local electronic structure and the correlations herein, thereby establishing firmly the compensated-spin character of the first ionization state. By combining our high-resolution XPS, HAXPES, and XAS experimental data we have shown that the high binding energy shoulder of the main line of the valence band PES spectrum of bulk NiO is indeed an intrinsic feature of the electronic structure. Comparing the bulk with the impurity system, we were able to identify features in the bulk NiO spectrum which are caused by screening processes involving local quasi core valence band states and non-local low-energetic many body states. We proposed a non-local screening mechanism for the Ni $3d$ one-electron removal spectrum of NiO, similar to that accepted to explain the Ni $2p_{3/2}$ core level PES of NiO. Quantitative evidence from theory is highly desired.

Chapter 4

Local electronic structure of Fe^{2+} impurities in MgO thin films: Temperature-dependent soft x-ray absorption spectroscopy study

Part of this work has been published in:
T. Haupricht, R. Sutarto, M. W. Haverkort, H. Ott, A. Tanaka, H. H. Hsieh, H.-J. Lin, C. T. Chen, Z. Hu, and L. H. Tjeng, Physical Review B **82**, 035120 (2010), (Editors' Suggestions).

Magnetite is one of the most controversially discussed systems in solid state physics [109]. It shows a first-order anomaly in the temperature dependence of the electrical conductivity at 120 K, i.e., the famous Verwey transition [110] which is accompanied by a structural phase transition from the cubic inverse spinel to a distorted structure. It is only very recently that one realizes that this transition may involve not only charge ordering of Fe^{2+} and Fe^{3+} ions but also t_{2g} orbital ordering at the Fe^{2+} sites [111, 112, 113]. Important in this regard are the recent results from band theory studies [114, 115] in which the charge and orbital occupations were calculated based on the available crystal structure data [111, 112].

It is highly desired to determine experimentally the electronic structure of Fe_3O_4 and especially the local energetics of the Fe^{2+} sites in order to

test the conditions under which the t_{2g} orbital polarization and ordering can occur. Unfortunately, a direct approach to this system is difficult since the simultaneous presence of Fe^{2+} and Fe^{3+} valences as well as octahedral and tetrahedral sites makes standard electron spectroscopic methods to yield rather broad spectral line shapes, i.e., too featureless for a precise analysis concerning the details about the effective crystal fields with a symmetry lower than O_h [116].

Here we report on our study of the electronic structure of Fe impurities in MgO thin films. Having the local quasi-octahedral (O_h) symmetry and similar metal-oxygen bond lengths, the impurity system could serve as a valuable reference for the more complex Fe^{2+} containing magnetite. Using soft x-ray absorption spectroscopy and an analysis based on full multiplet cluster calculations we found that the Fe impurities are all in the 2+ charge state and that a dynamical Jahn-Teller distortion is clearly present. The spectra showed a strong temperature dependence which can be traced back to the existence of low-lying excited states due to the presence of the spin-orbit interaction. We were able to make estimates concerning the magnitude and temperature dependence of the orbital and spin contributions to the local magnetic moments. We infer that these local effects need to be included when interpreting the temperature dependence of the orbital and spin moments in magnetite across the Verwey transition.

$Fe_xMg_{1-x}O$ samples were prepared as polycrystalline thin films in an ultra-high vacuum MBE system with a base pressure of 5×10^{-10} mbar (cf. Sec. 2.1). High purity Mg and Fe metal were co-evaporated from alumina crucibles onto clean Cu substrates. Molecular oxygen was simultaneously supplied through a leak valve. The oxygen partial pressure was kept at about 1×10^{-7} mbar and monitored by a quadrupole mass spectrometer during growth. The Mg effusion cell temperature was kept at 315 °C corresponding to an Mg deposition rate of 2.6 Å/min as verified using a quartz crystal thickness monitor. During growth the substrate temperature was kept at 250 °C which led to a distillation process that allows the growth of stoichiometric MgO. This resulted in a MgO deposition rate of about 4 Å/min. The thickness of the $Fe_xMg_{1-x}O$ films was about 120 Å. The use of thin films on metallic substrates was necessary to avoid charging problems which otherwise readily occur in electron spectroscopic experiments on bulk insulators such as MgO. Clean Cu substrates were prepared by growing roughly 1000 Å thick Cu films *in situ* on top of atomically flat, epi-polished and oxygen-annealed MgO substrates.

The XAS measurements were performed at the 11A1 Dragon beamline of the National Synchrotron Radiation Research Center (NSRRC) in Taiwan [68, 69]. The photon energy resolution at the Fe $L_{2,3}$ edges ($h\nu \approx$ 700-

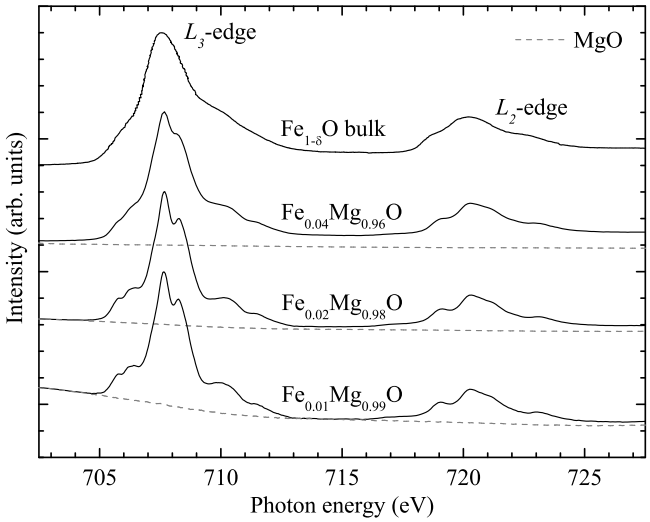

Fig. 4.1: Fe $L_{2,3}$ XAS spectra of $Fe_xMg_{1-x}O$ films for $x = 0.04, 0.02, 0.01$. Included is also the spectrum of bulk $Fe_{1-\delta}O$ (top curve, reproduced from Ref. [117]). The underlying dashed lines represent the XAS signal of a pure MgO film in the photon energy region of the Fe $L_{2,3}$, scaled to fit the pre-edge background of the respective $Fe_xMg_{1-x}O$ spectrum. All spectra were taken at room temperature.

730 eV) was set at about 0.35 eV. The spectra were recorded using the TEY method in the normal light incidence. The base pressure of the XAS chamber was 2×10^{-10} mbar. The MBE system was directly connected to this XAS chamber so that the freshly prepared samples could be transferred and measured all *in vacuo*, thereby assuring the cleanliness and reliability of the spectra presented here.

In Fig. 4.1 we show the experimental Fe $L_{2,3}$ XAS spectra of $Fe_xMg_{1-x}O$ films for $x = 0.04$, 0.02, and 0.01. We have also included the spectra of a bulk $Fe_{1-\delta}O$ crystal (reproduced from Ref. [117]) and of a pure MgO film (underlying dashed lines) as references. The MgO spectra have been scaled to fit the pre-edge background of the respective $Fe_xMg_{1-x}O$ spectrum. The pure MgO film was prepared under the same conditions as the $Fe_xMg_{1-x}O$ samples, i.e., it has $x = 0.00$. The Fe $L_{2,3}$ spectra are dominated by the Fe $2p$ core-hole spin-orbit coupling, which splits the spectrum roughly into two parts, namely, the L_3 ($h\nu \approx 708$ eV) and L_2 ($h\nu \approx 721$ eV) white line regions. The line shapes of the spectra depend strongly on the multiplet structure given by the atomiclike Fe $2p$-$3d$ and $3d$-$3d$ Coulomb and exchange interactions, as well as by the surrounding solid.

In going from bulk $Fe_{1-\delta}O$ to the films with decreasing Fe concentrations,

we can clearly observe that the spectral features become sharper. This can be taken as an indication for the presence of inter-Fe interactions in the more concentrated systems. Here we would like to note that the presence of Fe^{3+} species may also contribute to the broad spectral features of bulk $Fe_{1-\delta}O$, a material known to have inherent defects [118, 119]. For Fe concentrations lower than 2% the spectra do not significantly change anymore - apparently here we already arrived at the impurity limit. We notice that for the lowest Fe concentrations the pre-edge XAS background is increasing. This can be attributed to the contribution of the MgO to the XAS signal in the Fe $L_{2,3}$ region as shown by the spectrum of the pure MgO film.

We now focus on the temperature dependence of the spectra. Figure 4.2 shows a close-up of the experimental Fe L_3 and L_2 XAS spectra of $Fe_{0.02}Mg_{0.98}O$ for various temperatures ranging from 77 up to 500 K. For clarity, we here subtracted the XAS background coming from the pure MgO film in the Fe $L_{2,3}$ region. Clear and systematic changes with temperature can be observed in the spectra. This can be taken as a direct indication for the presence of local low-lying excited states.

To interpret and understand the spectra and their temperature dependence, we have performed simulations of the atomiclike $2p^6 3d^n \rightarrow 2p^5 3d^{n+1}$ ($n = 6$ for Fe^{2+}) transitions using the well-proven configuration-interaction cluster model [25, 29, 95]. Within this method we have treated the Fe impurity site as an FeO_6 cluster which includes the full atomic multiplet theory and the local effects of the solid. It accounts for the intra-atomic 3*d*-3*d* and 2*p*-3*d* Coulomb interactions, the atomic 2*p* and 3*d* spin-orbit couplings, the local crystal field, and the O 2*p*-Fe 3*d* hybridization. This hybridization is taken into account by adding the $3d^{n+1}\underline{L}$ and $3d^{n+2}\underline{L}^2$, etc. states to the starting $3d^n$ configuration, where $\underline{L}$ denotes a hole in the O *p* ligands. Pa-

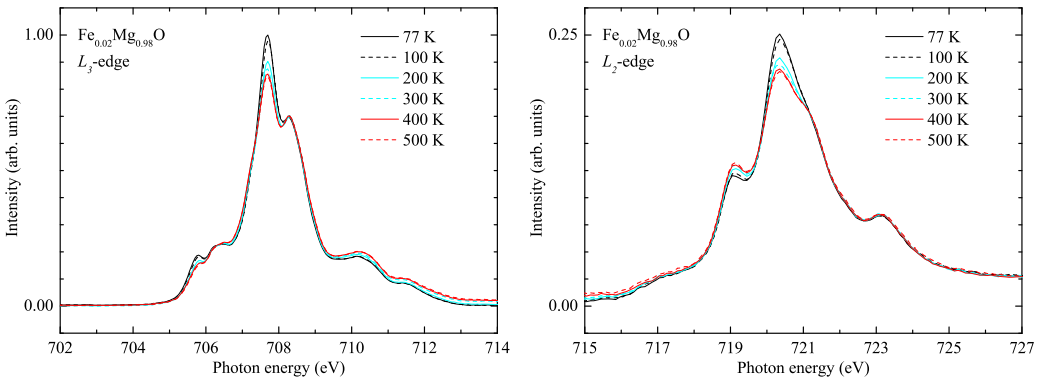

Fig. 4.2: Temperature dependence of the experimental Fe L_3 and L_2 XAS spectra of $Fe_{0.02}Mg_{0.98}O$ after subtraction of the pure MgO film background.

rameters for the multipole part of the Coulomb interactions were given by the Hartree-Fock values [25] while the monopole parts (U_{dd}, U_{pd}) were estimated from photoemission experiments on FeO [27]. The one-electron parameters such as the O $2p$-Fe $3d$ charge-transfer energies and integrals as well as the crystal field values were tuned to find the best match to the experimental spectra. The simulations were carried out using the program XTLS 8.3 [25, 120].

Starting with the simple crystal field scheme, an Fe ion in the O_h coordination will have its $3d$ states split into the lower lying t_{2g} and higher e_g levels, with the splitting given by 10Dq of order 1 eV (see Fig. 4.3). For an Fe^{2+} ion, five electrons will occupy all the available spin-up states. The remaining electron occupies one of the three spin-down t_{2g} orbitals ($t_{2g}^4 e_g^2$), giving the high-spin $S = 2$ Hund's rule ground state. In a multiplet scheme, neglecting the spin-orbit interaction, the ground state is termed the ${}^5T_{2g}$ state, well separated by about 1 eV or more from the higher lying ${}^5E_g$ and other lower spin configurations. Assigning a pseudo orbital momentum of $\tilde{L} = 1$ to the open t_{2g} shell [34, 121], the spin-orbit interaction will couple it to the $S = 2$ spin, resulting in three different states with $\tilde{J} = 1$, 2, and 3. The presence of the spin-orbit coupling in the $3d$ shell thus splits the 15-fold ${}^5T_{2g}$ state into the $\tilde{J}$ states with degeneracies of 3, 5, and 7, respectively (see Fig. 4.3). Using typical parameters for FeO [25, 120], we find an energy separation between them of about 33 meV ($\simeq$ 383 K) and 51 meV ($\simeq$ 597 K), respectively.

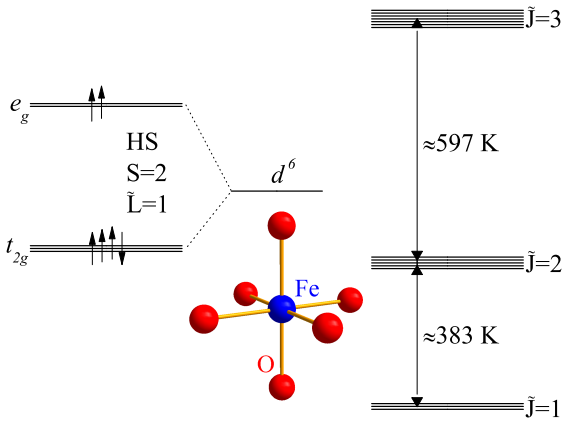

Fig. 4.3: Energy level diagrams for a Fe^{2+} cluster in the O_h coordination in a crystal field (left) and a full multiplet (right) scheme. HS denotes the Hund's rule high-spin configuration

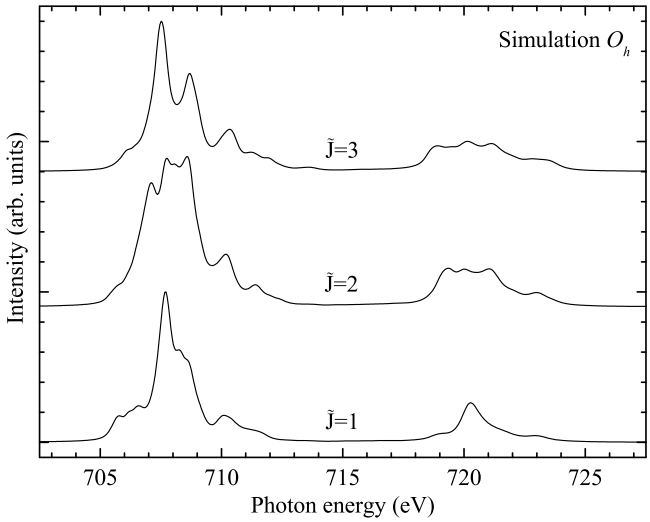

Fig. 4.4: Theoretical Fe $L_{2,3}$ XAS spectra starting from the three lowest multiplet states of the FeO_6 cluster in O_h symmetry, namely, the $\tilde{J} = 1$, 2, and 3 manifolds of the ${}^5T_{2g}$.

Important for the understanding of the line shape of the Fe $L_{2,3}$ XAS spectra and their temperature dependence is that initial states with different quantum numbers could produce quite different XAS spectra, since the dipole selection rules, e.g., $\Delta J = 0, \pm 1$, will dictate which of the possible final states can be reached in the photo-absorption process. This is shown in Fig. 4.4. Indeed, each of the three different $\tilde{J} = 1$, 2, and 3 states has its own characteristic XAS spectrum. It is then also quite natural to expect a strong temperature dependence for the XAS spectrum of a Fe^{2+} system if an increase in temperature causes a thermal population of the $\tilde{J} = 2$ and 3 excited states at the expense of a depopulation of the $\tilde{J} = 1$ ground state.

Yet, a detailed comparison between the experimental spectra and the simulations for the O_h case reveals important quantitative discrepancies. A closer look is provided in panel (a) of Fig. 4.5. One can clearly observe that neither the simulated 0 K spectrum, i.e., from the pure $\tilde{J} = 1$ ground state, nor the simulated 77 K spectrum, i.e., containing some amount of the $\tilde{J} = 2$ excited state, can reproduce the experimentally obtained 77 K spectrum. In particular, feature A is a single peak in the experiment while the O_h simulation produces two peaks, and feature B of the experiment has considerably more weight than can be generated by the simulation. All these strongly suggest that the symmetry must be lower than O_h, in line with earlier studies using optical and Mössbauer spectroscopies [122, 123, 124, 125, 126].

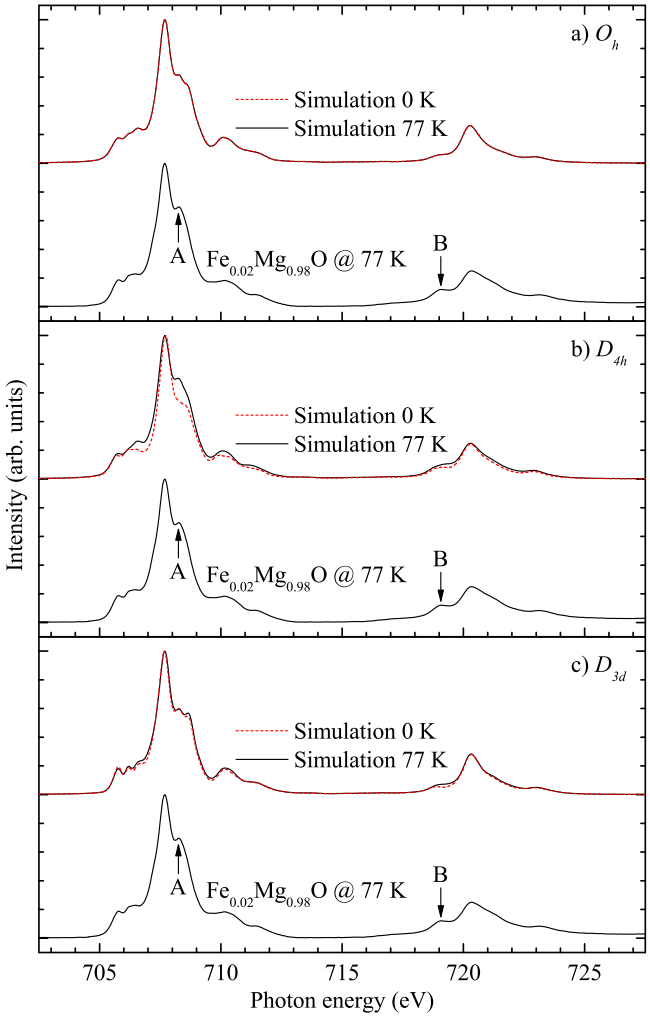

Fig. 4.5: Comparison between the experimental 77 K Fe $L_{2,3}$ XAS spectrum of $Fe_{0.02}Mg_{0.98}O$ and the simulated 0 K and 77 K spectra of the FeO_6 cluster in the (a) O_h, (b) D_{4h}, and (c) D_{3d} symmetry. Parameters for the simulations are explained in the text.

We have investigated two further scenarios: the D_{3d} (trigonal) and D_{4h} (tetragonal) cases. We find that the D_{3d} scenario does not provide a better fit, e.g., feature A still has a clear two peak structure and peak B has also not enough weight, as depicted in panel (c) of Fig. 4.5. On the other hand, we have been able to obtain a very good fit using the D_{4h} scenario as shown in the middle panel (b) of Fig. 4.5: The simulation gives more weight for peak B in better agreement with the experiment, and the simulated peak A is a more singly peak now as it is in the experiment. The overall line shape is thus well reproduced. We note that this also provides evidence that the $Fe_{0.02}Mg_{0.98}O$ film contains only Fe^{2+} ions since the simulation has been done for an FeO_6 cluster having the $3d^n$, $3d^{n+1}\underline{L}$, and $3d^{n+2}\underline{L}^2$ configurations with $n = 6$. We thus find no indication for the presence of Fe^{3+} or Fe^{1+} ions in our MBE-grown thin film samples, in contrast to other earlier studies [124, 125, 127, 128, 129, 130].

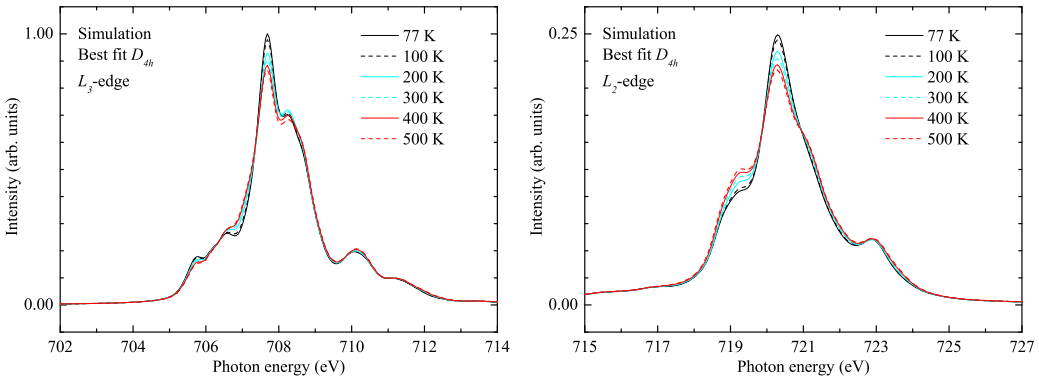

Fig. 4.6: Simulations of the temperature dependence of the Fe L_3 and L_2 XAS spectra in the D_{4h} symmetry. Parameters for the simulations are explained in the text.

Continuing now with the D_{4h} scenario, we also have simulated the temperature dependence of the Fe L_3 and L_2 XAS spectra. Figure 4.6 shows the results. One can observe that the experimentally obtained temperature dependence (see Fig. 4.2) is quantitatively very well reproduced. The good agreement between simulation and experiment at all the temperatures measured can be taken as a strong indication that the D_{4h} scenario describes accurately the local symmetry of the Fe ion in MgO and that the model parameters chosen are realistic giving also an appropriate energy separation between the ground state and the excited states. In the following we will discuss in more detail the total energy level diagram of the Fe^{2+} cluster in D_{4h} symmetry.

As already mentioned above, in O_h symmetry the Fe $3d^6$ $^5T_{2g}$ ground

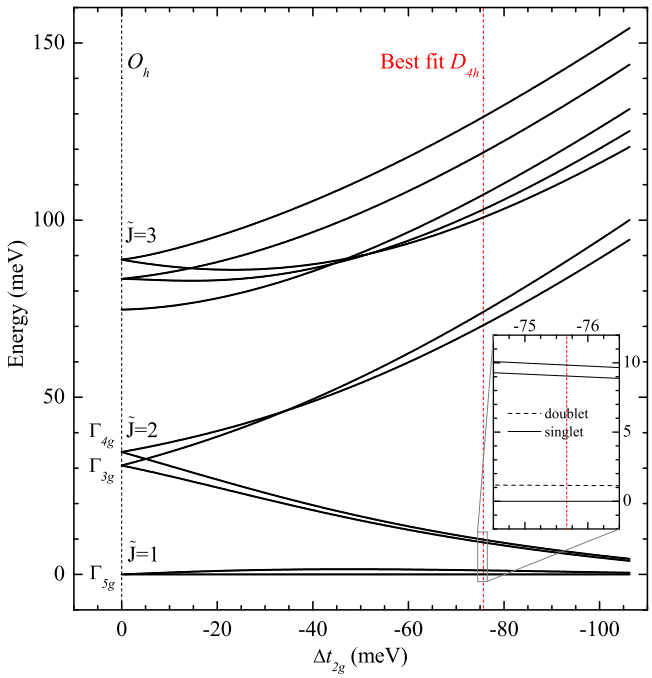

Fig. 4.7: The total energy level diagram of the Fe^{2+} FeO_6 cluster as a function of the D_{4h} crystal field splitting expressed in terms of Δt_{2g}.

state is split by the spin-orbit interaction into the $\tilde{J}$ = 1, 2, and 3 states. A closer look reveals that there are also smaller splittings within the $\tilde{J}$ = 2 and 3 manifolds. The ground state with $\tilde{J}$ = 1 is also labeled as Γ_{5g}, while the higher lying first excited states with $\tilde{J}$ = 2 are given the terms Γ_{3g} and Γ_{4g}. We now switch on the D_{4h} crystal field by introducing the parameters Ds and Dt [34], as well as differences in the O $2p$-Fe $3d$ hopping integrals along the c axis vs. the a axis of the FeO_6 cluster. The D_{4h} effective crystal field parameter can then be most conveniently described as the effective energy splitting Δt_{2g} between the xy and the yz/zx states. This splitting can be determined from a total energy calculation for which the spin-orbit interaction is set to zero. Here a negative Δt_{2g} means that the xy is the lowest state (compressed octahedron). The resulting total energy diagram (including spin-orbit interaction) vs. Δt_{2g} is plotted in Fig. 4.7.

In going from O_h to D_{4h} with increasing Δt_{2g}, we find that the splitting between the Γ_{5g} ground state and part of the excited states Γ_{3g} and Γ_{4g} becomes reduced. It decreases from roughly 30 meV for $\Delta t_{2g} = 0$ to approximately 10 meV for $\Delta t_{2g} = -76$ meV, the value with which we find the best simulations for our XAS data. See also the inset of Fig. 4.7. This 10 meV value agrees very well with earlier optical and spin relaxation measurements which have inferred the existence of a state at about 100-115 cm^{-1} [127, 128]. In our simulations we need to have the splitting reduced from its large cubic value of 30 meV to this particular 10 meV number in order (1) to have sufficient admixing of the Γ_{3g} and Γ_{4g} into the primarily Γ_{5g}-like ground state so that feature A becomes more like a single peak and feature B gains substantial spectral weight as in the experiment (see Fig. 4.5), and (2) to obtain sufficient thermal population of the excited states with increasing temperature in the 77-500 K range so that the experimentally observed strong temperature dependence is reproduced (see Figs. 4.2 and 4.6). We would like to note that the ground state of this $3d^6$ system in the D_{4h} symmetry is a singlet, as can be seen in the inset of Fig. 4.7.

As indicated above, we found $\Delta t_{2g} = -76$ meV to be the optimal number for the effective energy splitting in order to achieve the best simulations for the experimental data. It is important to realize that this splitting lies well within the phonon energies of the MgO crystal [131, 132]. Therefore, rather than expecting to see a static Jahn-Teller distortion, as it is present in some Fe^{2+} containing metal complexes [133, 134, 135], one should take this distortion as dynamical in which the phonons are strongly coupled to the electronic degrees of freedom as pointed out by Ham and co-workers [39, 123, 126]. To generate static distortions one would need an effective crystal field splitting of about 0.2 eV or larger.

Having found that the D_{4h} scenario properly simulates the experimental

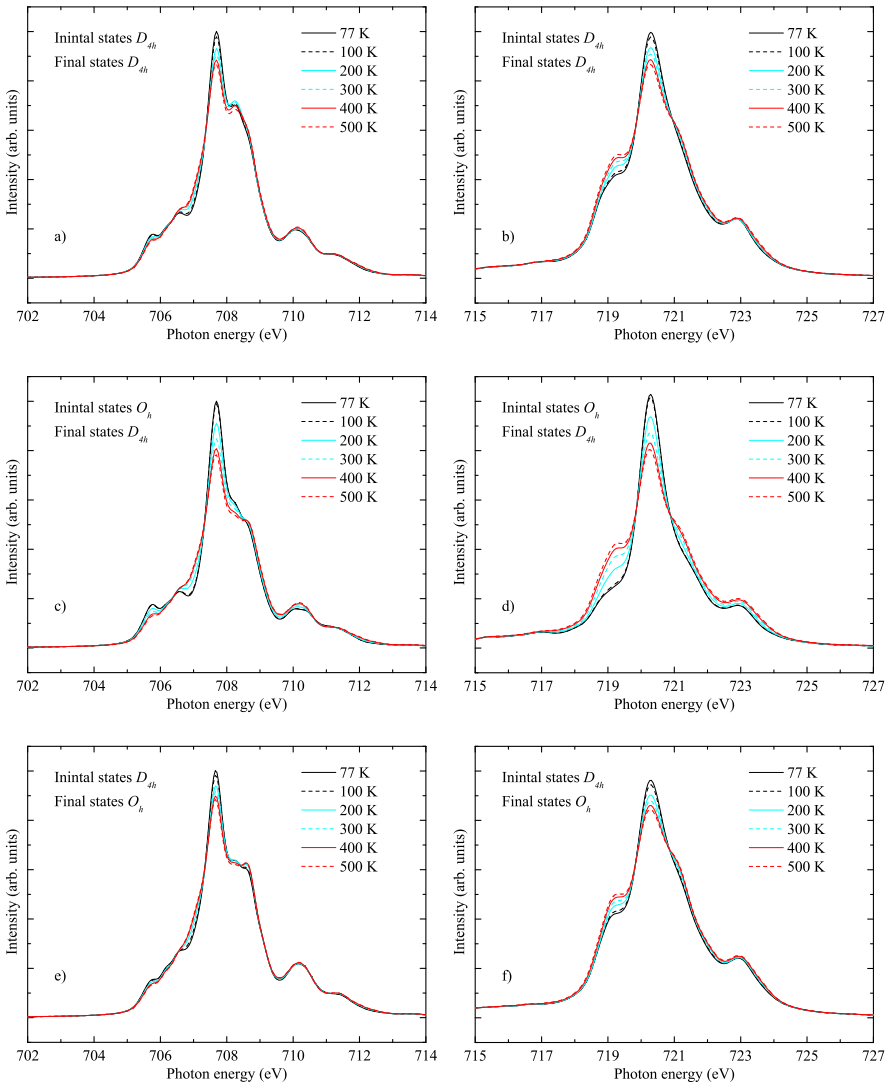

Fig. 4.8: Simulations of the temperature dependence of the Fe L_3 and L_2 XAS spectra for initial and final states in D_{4h} symmetry [panel (a) and (b)], initial states in O_h and final states in D_{4h} symmetry [panel (c) and (d)], and initial states in D_{4h} and final states in O_h symmetry [panel (e) and (f)]. Parameters for the simulations are explained in the text.

temperature dependence and leads to an total energy diagram that is in good agreement with other studies [127, 128], we still have to verify whether the temperature dependence is due to the D_{4h} splitting in the initial states. In XAS initial and final states enter the spectra on an equal footing, i.e., the temperature dependence could also be a final state effect. Therefore, in Fig. 4.8 we show again the simulated temperature dependence of the Fe L_3 and L_2 edges, but now in three different scenarios: (1) Initial and final states in D_{4h} symmetry [panel (a) and (b)], (2) initial states in O_h and final states in D_{4h} symmetry [panel (c) and (d)], and (3) initial states in D_{4h} and final states in O_h symmetry [panel (e) and (f)]. Comparing scenario (2) and (1) we find that with the initial states in O_h the temperature dependence is largely overestimated. In addition, several features in the simulated spectra do not properly fit the experiment, as already discussed above. In contrast, the temperature dependence with the initial states in D_{4h} (3) is very similar to the all D_{4h} scenario (1). This means that the temperature dependence is indeed due to the D_{4h} splitting in the initial states. However, a closer look reveals that the line shapes in scenarios (3) and (1) are not exactly the same, indicating that for the simulation a proper treatment of both, initial and final states, is needed.

It is now interesting to see what consequences the presence of the D_{4h} crystal field splitting has for the magnetic properties of the Fe^{2+} ion. We calculate the spin and orbital contributions to the magnetic moments in the presence of an exchange field (H_{ex}) of 75 meV. We chose for this value as it may be taken as a crude estimate for the case of Fe_3O_4. Figure 4.9 shows the results of the calculations for several values of the crystal field energy Δt_{2g}.

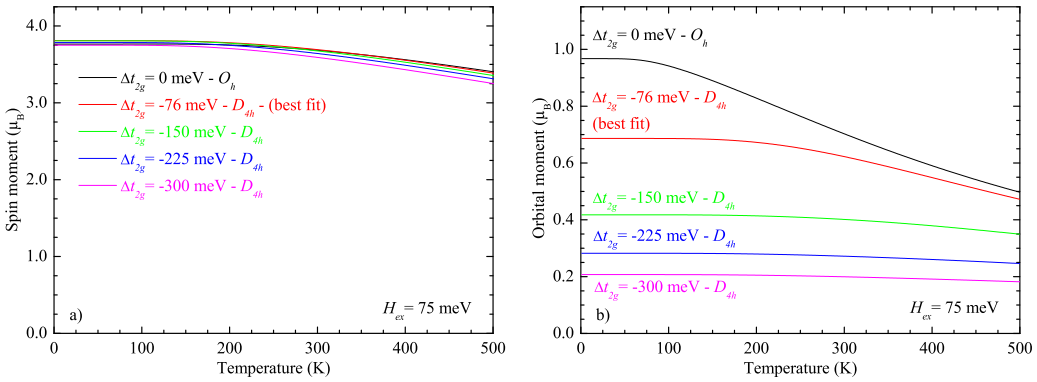

Fig. 4.9: Simulated temperature dependence of the spin [$m_s = 2 \cdot S_x$, panel (a)], and orbital [$m_l = L_x$, panel (b)] contributions to the local magnetic moment of the FeO_6 cluster for various D_{4h} crystal field energies (Δt_{2g}) and an exchange field of 75 meV.

For $\Delta t_{2g} = 0$, i.e., the O_h case, the orbital moment is very large, very close to 1.0 μ_B. Yet, it also decreases rapidly with temperature: At 500 K it becomes 0.5 μ_B. This is the consequence of the thermal population of the $\tilde{J} = 2$ and 3 excited states. Upon switching on the D_{4h} crystal field to -76 meV, the orbital moment gets also reduced, to about 0.7 μ_B already at 0 K. Increasing further the crystal field to -150 meV, -225 meV, and -300 meV produces smaller and smaller orbital moments, i.e., about 0.4, 0.3, and 0.2 μ_B, respectively. The spin moment, nevertheless, always stays close to about 4 μ_B.

These findings could provide an interesting path to critically test recent electronic structure theories [114, 115] for the explanation of the experimentally observed complex charge and orbital order phenomena in Fe_3O_4 [111, 112, 113]. An accurate measurement of the orbital moment, i.e., the orbital moment at the Fe^{2+} sites (the Fe^{3+} $3d^5$ with their high-spin half-filled shell do not carry an orbital moment), will provide a direct estimate of the magnitude of the effective crystal field splitting. This in turn will determine whether the occupied minority t_{2g} orbital of the Fe^{2+} is made of mainly real space orbitals or has a more complex nature. Only for crystal fields substantially larger than the spin-orbit interaction one can obtain the real space orbitals necessary to build a robust orbital ordering. In this sense the measurement of 0.76 μ_B orbital moment at 88 K by Huang *et al.* [136] would suggest the occupation of a complex t_{2g} orbital and a crystal field too small to produce a static Jahn-Teller distortion. On the other hand, the measurement by Goering *et al.* [137] of 0.01 μ_B would support the scenario for real-space orbitals and large static Jahn-Teller distortions, much more in line with the recent theoretical studies [114, 115]. Nevertheless, the issue on the magnitude of the orbital moment is not clear and is subject of debate [138, 139].

To conclude, we have succeeded in preparing the Fe^{2+}:MgO impurity system using MBE thin film technology. The resulting Fe $L_{2,3}$ soft x-ray absorption spectra display very sharp features, thereby allowing us to firmly establish that the Fe local coordination has a lower symmetry than O_h. A detailed analysis of the spectral line shape and its temperature dependence reveals that the local symmetry is D_{4h} with an effective t_{2g} crystal field splitting of about -76 meV. With an energy well within the phonon frequencies of MgO, this gives rise to a dynamic Jahn-Teller distortion. Using this Fe^{2+} impurity system as a model we showed that an accurate measurement of the orbital moment in Fe_3O_4 will provide a direct estimate for the effective local low-symmetry crystal fields on the Fe^{2+} sites, important for the theoretical modeling of the formation of orbital ordering.

Chapter 5

Local view on correlated electron systems: Electronic structure of Mn^{2+} impurities in MgO

Transition metal monoxides are very important model systems to study electron correlation effects in solids. Among these, MnO plays a special role because the Mn^{2+} ion has a half-filled $3d$ shell with the $3d^5$ high-spin configuration stabilized by the Hund's rule coupling [140]. MnO crystallizes in the NaCl structure and orders antiferromagnetically below the Néel temperature of $T_N = 118$ K [141]. It is an insulator with a bandgap of about 3.6 eV [142]. Even though band structure calculations find an insulating character of MnO at least in the magnetically ordered phase, the gap is always underestimated [143, 144, 145]. It has been shown that in band structure calculations the long-range magnetic order is responsible for the gap [143, 145]. In the paramagnetic phase MnO was predicted to be metallic by one-electron theory [143]. This problem could be fixed by cluster type calculations [25, 140, 146], which show that for MnO both, the *d-d* Coulomb interaction U and the charge transfer energy Δ, are large with comparable values. From these estimates MnO was classified in the intermediate region (AB) of the Zaanen-Sawatzky-Allen (ZSA) [23] phase diagram meaning that the first ionization states should be of highly mixed character [140]. The gap could also be fixed in band theory by the inclusion of a self-interaction correction term to the model [17]. However, band structure calculations are not able to reproduce excitation spectra of MnO, such as PES or XAS. The configuration-interaction cluster model works quite well to simulate these data [147], but on the other hand is not *ab initio* and it is in fact an impurity

calculation, thereby neglecting the band formation of the bulk material. It is unclear to what extent non-local effects, such as those found in NiO (cf. Chapter 3 and Ref. [93]), enter the excitation spectra.

Because of its special role as a limiting case among the transition metal oxides (half-filled $3d$ shell), a profound understanding of the electronic structure of MnO is highly desirable. However, in order to develop reasonable theoretical models clean experimental data sets for comparison are needed. Electron spectroscopies, like XAS and PES, offer a direct approach to examine the microscopic electronic structure. Unfortunately they are both susceptible to specimen charging and saturation effects for measurements on insulating samples. In PES charging effects lead to shifts and broadening of the spectra, in XAS they also broaden the spectra and change the line shape and background.

We, therefore, set out to study stoichiometric MnO and Mn^{2+} impurities in MgO ($Mn_{0.02}Mg_{0.98}O$) both grown as thin films on Ag substrates using XAS and PES. The use of thin films grown on metal substrates offers a way to eliminate the above mentioned charging problems. If the films are thin enough the conducting substrate provides electrons which compensate the charge emitted in the photo-excitation process. We show that the Mn $L_{2,3}$ XAS spectra of MnO thin films grown on Ag are, in contrast to those of bulk MnO, free from charging effects, thereby representing a well defined data set for comparison to theory. We explain differences in the Mn $L_{2,3}$ XAS spectra of $Mn_{0.02}Mg_{0.98}O$ and MnO by simulating the experimental data using a cluster model, thereby showing that they are caused by different local crystal fields in both compounds. Based on these results we claim that those different local crystal fields should also show up in the Mn $2p$ XPS spectra. In addition by using 140 eV photons (the Cooper minimum of the Ag $4d$) and a subtraction procedure, we are also able to extract the MnO impurity contribution to the valence band PES spectrum of $Mn_{0.02}Mg_{0.98}O$. A comparison to the spectrum of the stoichiometric MnO and to the result of the respective cluster simulations shows that bulk and impurity spectra are very similar and that non-local effects play, if present, only a minor role here.

The measurements were performed at the 11A1 Dragon beamline of the NSRRC in Hsinchu, Taiwan [68, 69]. X-ray absorption data were collected using the TEY mode in normal light incidence. In the energy region of the Mn $L_{2,3}$ edge ($\simeq 630-660$ eV) the photon energy resolution of the beamline was set to about 240 meV, and the degree of linear polarization was close to 100 %. PES spectra were recorded using a Scienta SES-100 electron energy analyzer. For the PES measurements using 140 eV photons the overall energy resolution was set to about 130 meV. The Mn $2p$ XPS ($h\nu = 1486.6$ eV) spectrum of

MnO was recorded using a Vacuum Generators twin crystal monochromator Al-K_α source, with an overall energy resolution set to 0.4 eV. The thin film samples were prepared by molecular beam epitaxy *in situ*. The base pressure of the UHV system was below 3×10^{-10} mbar. To simulate the experimental data we carried out a configuration-interaction cluster calculation on a MnO_6 cluster which includes the full atomic multiplet theory, the local crystal fields, the hybridization with the O $2p$ ligands, and the spin-orbit coupling. It has been shown in many cases that this kind of calculation is very suitable to simulate and interpret XAS and PES data [25, 29, 95]. The calculations were performed using the XTLS 8.3 code by A. Tanaka [25].

The thin film samples were grown on polished Ag foil (99.9%) from Mateck GmbH. Before growth the foil was cleaned in UHV conditions by several cycles of Ar sputtering and annealing at 500 °C. For the preparation of MnO and $Mn_{0.02}Mg_{0.98}O$ thin films, high purity Mn and Mg metal were evaporated from alumina crucibles in effusion cells from Luxel. Molecular oxygen was supplied via a leak valve and a nozzle located at a distance of about 2 cm from the sample, and its partial pressure was monitored using a baratron capacitance manometer and an ion gauge. Before growing the final compounds on top we have first grown a 30 Å MgO buffer layer on top of the clean Ag substrate in order to exclude any possible influence of the interface to the Ag substrate to the spectroscopic data. To do so, Mg was evaporated with a evaporation rate of about 1 Å/min in an oxygen atmosphere of 5×10^{-7} mbar. For the MgO buffer layer, the substrate temperature was kept at 150 °C during growth. For the pure MnO sample, 170 Å of MnO was grown on top of the buffer layer using a Mn rate of 1.1 Å/min, an oxygen partial pressure of 7×10^{-8} mbar, and a substrate temperature of 300 °C. The $Mn_{0.02}Mg_{0.98}O$ film (thickness about 150 Å) was grown on top of the MgO buffer by co-evaporation of Mg an Mn metal in an oxygen background of about 4×10^{-8} mbar, the substrate temperature kept at 350 °C. The overall thickness of the thin film samples was chosen such that no contribution of the Ag substrate to the spectra was found, and on the other hand no charging effects were observed. Furthermore, distortions induced by the Ag substrate which were found for ultrathin MnO films on Ag [148] are prevented by the film thickness and the MgO buffer layer.

In Fig. 5.1 we compare the Mn $L_{2,3}$ XAS of a freshly cleaved bulk MnO crystal to that of a polycrystalline MnO film grown on Ag. First of all we find that all features in the spectra are the same. This reflects the good quality of the film, showing that it is indeed stoichiometric MnO with the Mn ions in the 2+ valence state. We find no indications of Mn ions in other valences such as Mn^{3+} or Mn^{4+}. Furthermore, we find that in the bulk MnO XAS most features are suppressed compared to the spectrum of the thin film.

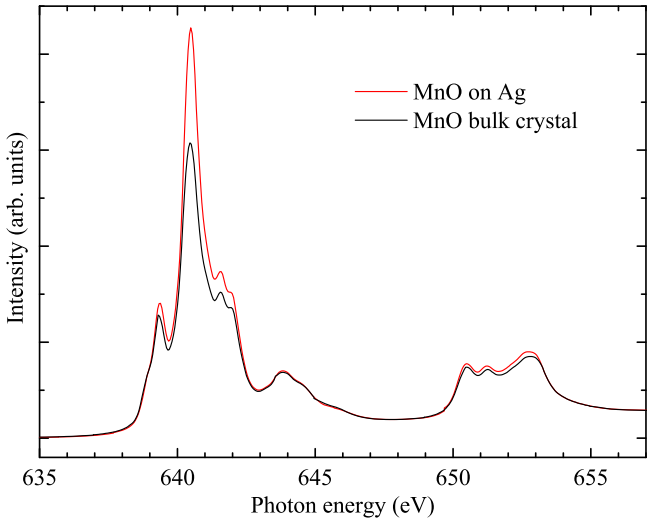

Fig. 5.1: Mn $L_{2,3}$ XAS spectrum of a polycrystalline MnO film grown on Ag in comparison to that of a freshly cleaved MnO bulk crystal. As a result of specimen charging, the spectrum of the single crystal is considerably suppressed.

This is due to specimen charging that occurs for the insulating bulk MnO. In the thin film grown on Ag, the film is thin enough such that the conducting Ag substrate can provide electrons that neutralize this charging effect here. This allows us to conclude that the spectrum of the polycrystalline MnO film grown on Ag is actually the "better" MnO for comparison to theory since it is free from saturation or charging effects that are present in bulk samples.

The Mn $L_{2,3}$ XAS of the polycrystalline MnO on Ag (see above) and that of $Mn_{0.02}Mg_{0.98}O$ on Ag is shown in Fig. 5.2. Comparing both spectra we see that they are surprisingly different. Even though the position of the main peaks is the same, firmly establishing that also for the $Mn_{0.02}Mg_{0.98}O$ the Mn ions are in the 2+ valence state, all other features in the spectrum differ considerably in detail. In order to explain the differences in the spectra we first recall that XAS is very sensitive to the local crystal fields and symmetry of the probed ion. Since the Mn^{2+} in MnO has a high-spin $3d^5$ configuration, stabilized by the Hund's rule coupling, it cannot lower the energy of the ground state by lowering its symmetry from O_h. Thus, it is very unlikely that a lower local symmetry is the reason for the differences in the XAS of MnO and $Mn_{0.02}Mg_{0.98}O$. However, looking at the crystal structures of bulk MgO and MnO we recall that their lattice constants are quite different ($a_{MgO} = 4.21$ Å [149] and $a_{MnO} = 4.44$ Å [150]). A different transition metal to oxygen distance will of course influence the strength of the cubic crystal

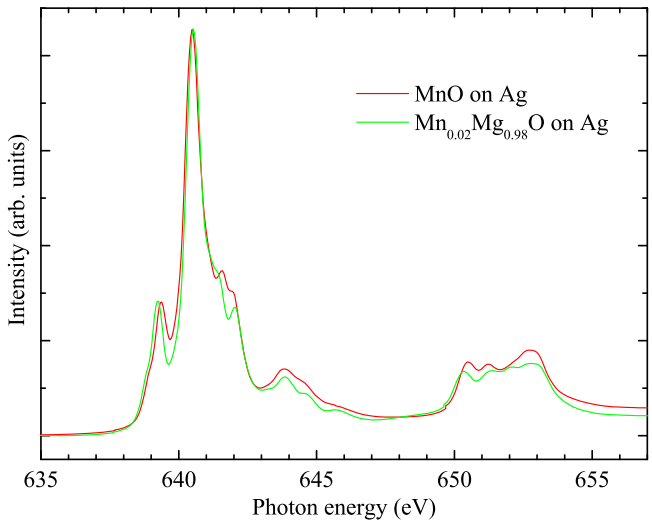

Fig. 5.2: Mn $L_{2,3}$ XAS spectrum of a polycrystalline MnO film grown on Ag in comparison to that of $Mn_{0.02}Mg_{0.98}O$ on Ag.

field splitting $10Dq$ and of the hybridization, as it has already been shown in electron spin resonance measurements [151, 152].

We have, therefore, performed a configuration-interaction cluster calculation on an MnO_6 cluster in O_h symmetry. d^5, $d^6\underline{L}$, and $d^7\underline{L}^2$ initial states are included, where $\underline{L}$ denotes a ligand hole. We used parameters typical for a Mn^{2+} system in octahedral symmetry [25, 27, 153]. The result of the simulation in comparison to the experimental data is shown in Fig. 5.3. For the comparison to the simulation, an integrated background was subtracted from the raw experimental data (Fig. 5.2) here. The Lorentzian and Gaussian broadening, that has been added to the calculated spectral weights to draw the spectra, is the same for both systems. Comparing experiment and theory we first of all find that for both systems the XAS data can be very well reproduced by the cluster analysis. The only difference in both simulations is the value of the parameters $10Dq$, the ionic crystal field splitting, and $V(e_g)$, the strength of the p-d hybridization. These differences in the parameter sets can be understood by the different surrounding of the MnO_6 cluster for the impurity system: The lattice constant of MgO is around 5% smaller than that of bulk MnO and, thus, the crystal field splitting is larger here. In our model we have, therefore, assumed that these parameters change with the ratio of the MgO and $Mn_xMg_{1-x}O$ lattice constant d as $10Dq(Mn_xMg_{1-x}O) = 10Dq(MnO) \cdot d^{-5}$ and $V(e_g)(Mn_xMg_{1-x}O) = V(e_g)(MnO) \cdot d^{-7/2}$ [154, 155]. We have obtained

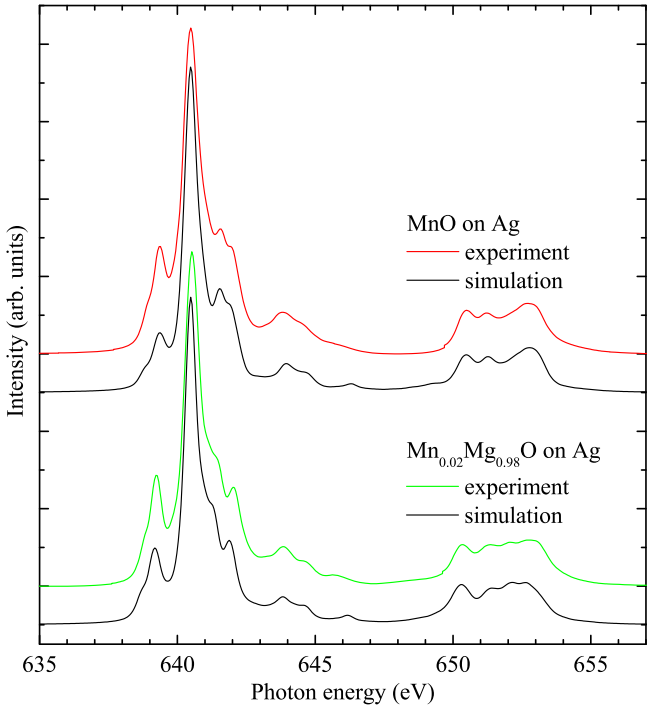

Fig. 5.3: Comparison of the experimental Mn $L_{2,3}$ XAS spectra of MnO and $Mn_{0.02}Mg_{0.98}O$ to the result of a simulation using a configuration-interaction cluster model. Parameters of the calculations are explained in the text.

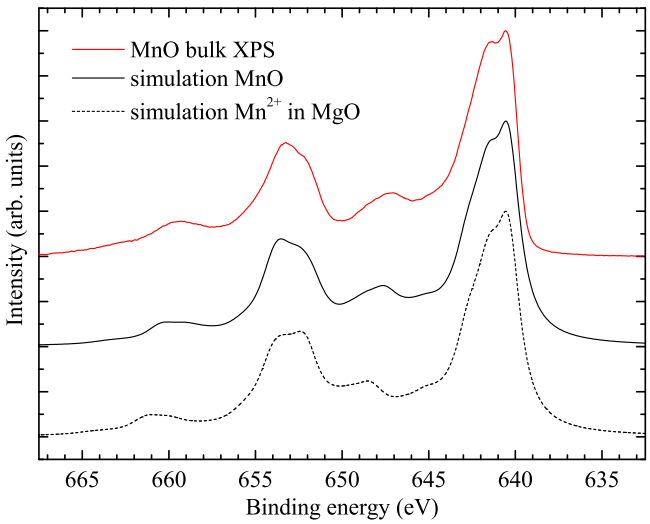

Fig. 5.4: Mn $2p$ XPS spectrum of a freshly cleaved MnO single crystal compared to simulated spectra using the cluster model. Parameters of the calculations are explained in the text.

the best fit to the experimental data for $d = 0.95$, consistent with the value that one gets using the bulk lattice constants of MgO and MnO. This means that the Mn impurity sites in the MgO take over the MgO lattice constant. With this we end up with $10Dq = 0.40$ eV and $V(e_g) = 2.30$ eV for the MnO, and $10Dq = 0.52$ eV and $V(e_g) = 2.75$ eV for the $Mn_{0.02}Mg_{0.98}O$. Note that the hybridization and the change therein have by far the larger effect to the simulated spectra than the $10Dq$ parameter. Therefore, the value of the exponent n in the d^{-n} dependence of the ionic crystal field parameter $10Dq$ (here $n = 5$) cannot be tested in this particular experiment.

After we have found from the XAS experiments together with the cluster simulations that the different manganese to oxygen distances in MnO and $Mn_{0.02}Mg_{0.98}O$ lead to different local crystal fields, one might expect that these differences should also show up in the Mn $2p$ core level XPS. We have, therefore, also calculated the Mn $2p$ XPS spectra using the cluster model with the same two sets of parameters. The result is shown in Fig. 5.4. Here we also show the Mn $2p$ XPS of a freshly cleaved MnO single crystal; the Mn $2p$ XPS of the impurity system has not yet been measured. Comparing experiment and the simulation using the bulk MnO parameter set we find a very good agreement. As for the XAS, energy positions and the spectral line shape are well reproduced. When we compare the two simulations using the different parameter sets of MnO and $Mn_{0.02}Mg_{0.98}O$ we find that indeed

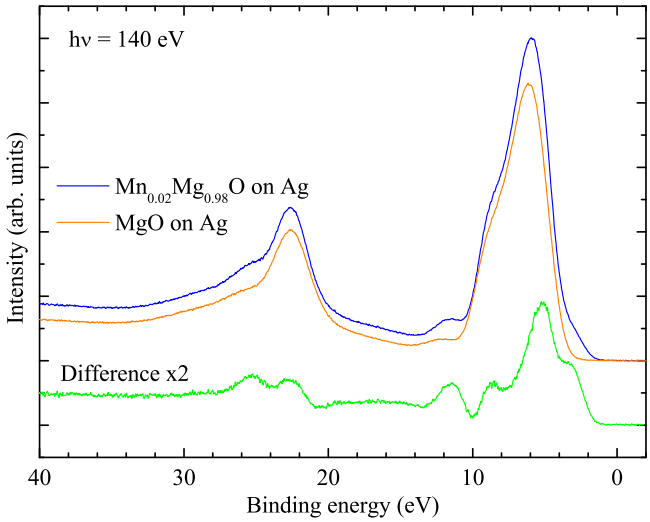

Fig. 5.5: Extraction of the impurity valence band: The spectra of $Mn_{0.02}Mg_{0.98}O$ (blue) and MgO (orange) on Ag are very similar at first sight. Only the difference spectrum (green) reveals the MnO impurity contribution to the valence band.

the spectra are also different here. Even though they are not so obvious as in the XAS, we find distinct differences in the line shape of the Mn $2p_{1/2}$ line and in the energy positions of the two charge-transfer satellites. Thus, a detailed experimental study of the Mn $2p$ core level XPS of $Mn_xMg_{1-x}O$ would certainly give further insight to this system.

We now turn to the valence band PES spectrum. To do so we first have to deal with the problem, that due to the thinness of the film the Ag $4d$ signal from the substrate will contaminate the $Mn_xMg_{1-x}O$ signal that we would like to record. By using 140 eV photons, which is the so-called Cooper minimum of the Ag $4d$ [59, 97], we were able to suppress the Ag $4d$ contribution to the valence band spectra below the detection limit. Then we need to extract the MnO impurity contribution from the $Mn_{0.02}Mg_{0.98}O$ valence band spectrum which is, of course, basically the O $2p$ valence band of the MgO. The extraction of the impurity contribution is shown in Fig. 5.5. We find the MnO impurity contribution as the difference of a $Mn_{0.02}Mg_{0.98}O$ and a MgO reference spectrum. To eliminate effects of small differences in the sample preparation both, the $Mn_{0.02}Mg_{0.98}O$ and the MgO reference film, were grown at the same time and on the same substrate by separating parts of the substrate using a stainless steel flag.

We are now ready to compare the bulk and the impurity valence band spectra (see Fig. 5.6). The experimental valence band spectra have in general

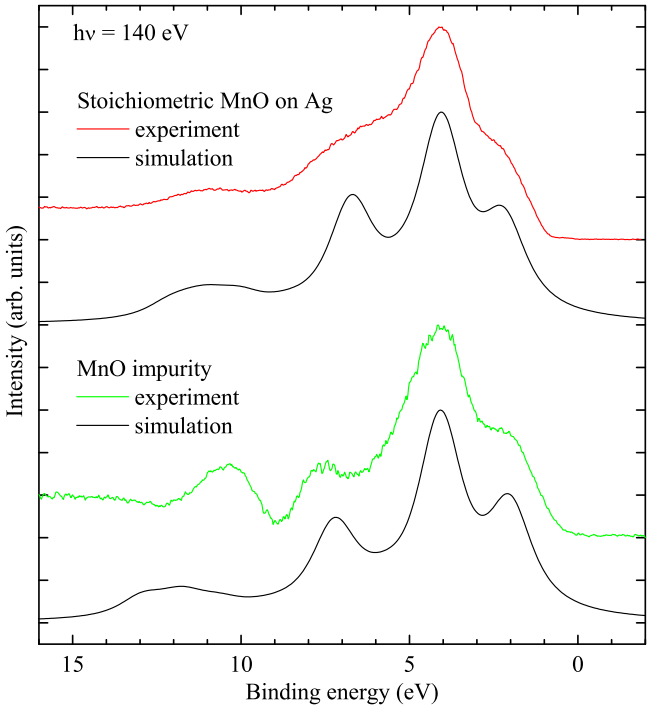

Fig. 5.6: Comparison of the valence band PES spectra of stoichiometric MnO on Ag and of MnO impurities in MgO. The impurity spectrum has been shifted by about 1 eV for comparison. Also included are simulated spectra resulting from the cluster model. Parameters of the calculations are explained in the text.

similar features: They consist of four structures, yet, the impurity spectrum is considerably narrower than the bulk. In addition we find that in the impurity spectrum the spread of the spectral weight over the energy range is larger. Moreover, the intensity ratio of the three main peaks differs somewhat from the bulk. Most of these observations can be well reproduced by the cluster model, as it is also shown in Fig. 5.6. The larger hybridization ($V(e_g)$) in $Mn_{0.02}Mg_{0.98}O$ spreads the spectral weight wider over the measured energy range, in good agreement with earlier studies [140]. The impurity spectrum shows a pronounced feature at around 10.5 eV binding energy which we do not find in the bulk spectrum nor in the simulations, at least, not as pronounced. At present we are not able to explain the origin of this feature. It is possible that this feature is an artefact of the extraction of the impurity valence band from the raw data (see Fig. 5.5). The subtraction procedure as well as the high surface sensitivity at 140 eV photons makes us very sensitive to small imperfections, impurities, etc. in or on the the surface of the sample which are too small to also show up in the XAS.

To conclude, we have studied the electronic structure of MnO and $Mn_{0.02}Mg_{0.98}O$ thin films grown on Ag substrates by MBE using XAS and PES. By comparison of the XAS of bulk MnO to that of the thin film grown on Ag we have shown that the Ag substrate is able to compensate for specimen charging due to the photo-excitation process. We have found that the Mn $L_{2,3}$ XAS spectra of MnO thin films grown on Ag provide a well defined data set for comparison to theory. We were able to explain differences in the Mn $L_{2,3}$ XAS spectra of $Mn_{0.02}Mg_{0.98}O$ and MnO by fitting the experimental data using a cluster model taking the different local crystal fields in MnO and MgO into account. The simulation suggests that similar effects should also be visible in the Mn $2p$ XPS. We were able to measure and extract the MnO impurity valence band PES spectrum by using 140 eV photons and a subtraction procedure. The impurity valence band spectrum shows differences to that of the bulk which can be explained by the cluster model with the use of different local crystal fields in both compounds. Yet, the differences are not as dramatic as in the case of NiO, so that we can conclude that non-local effects play only a minor role in MnO.

Chapter 6

V^{3+} impurities in Al_2O_3: Importance of intersite correlations

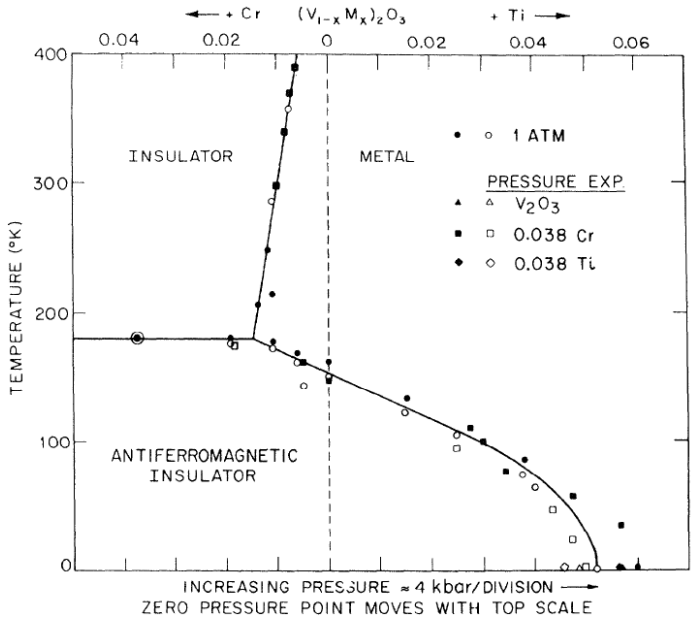

Fig. 6.1: Phase diagram of V_2O_3. Reproduced from Ref. [156]

Vanadium sesquioxide V_2O_3 has extensively been studied over the past decades as the canonical Mott-Hubbard system [6]. It shows a phase transition at around 150 K with a change of the resistivity of seven orders of

magnitude [109], accompanied by a structural transition from a corundum (T > 150 K) to a monoclinic (T < 150 K) structure [157]. This changes remarkably upon applying external pressure or when substituting part of the V ions by several percent of Ti or Cr. For substitutions by small amounts of Cr a second phase transition sets in, but here the symmetry of the crystal remains unchanged. Because of this feature it was argued that the phase transition is due to the correlation of electrons (Mott transition) [109]. Looking at the famous phase diagram of V_2O_3 shown in Fig. 6.1 [156] one finds three phases depending on pressure, doping, and temperature: Paramagnetic metal (PM), paramagnetic insulator (PI), and antiferromagnetic insulator (AFI).

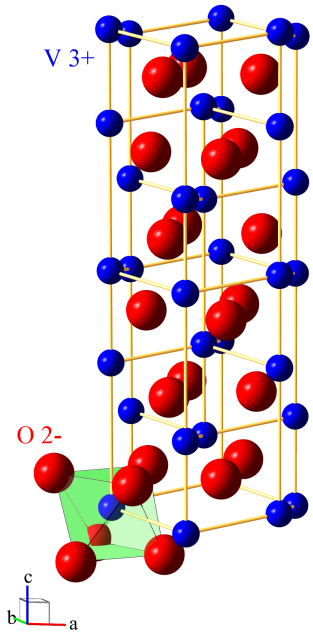

Fig. 6.2: Corundum crystal structure of V_2O_3: The V^{3+} ions are arranged as pairs along the c axis. Each V^{3+} ion is surrounded by a trigonally distorted oxygen octahedron. Illustrated using [28].

In the corundum structure of V_2O_3, each V^{3+} ion is surrounded by a trigonally distorted (D_{3d}) oxygen octahedron (see Fig. 6.2). Thus, in an one-electron picture, the trigonal crystal field lifts the degeneracy of the t_{2g} states of the cubic crystal field and splits these into a non-degenerate a_{1g} and a doubly degenerate e_g^π state. See Fig. 6.3. On top of that, the V^{3+} ions are arranged in pairs along the c axis in the corundum structure. These so-called dimers have been proposed to form molecular orbitals (a_{1g} molecular singlets) which would lead to an effective $S = 1/2$ system [158, 159, 160].

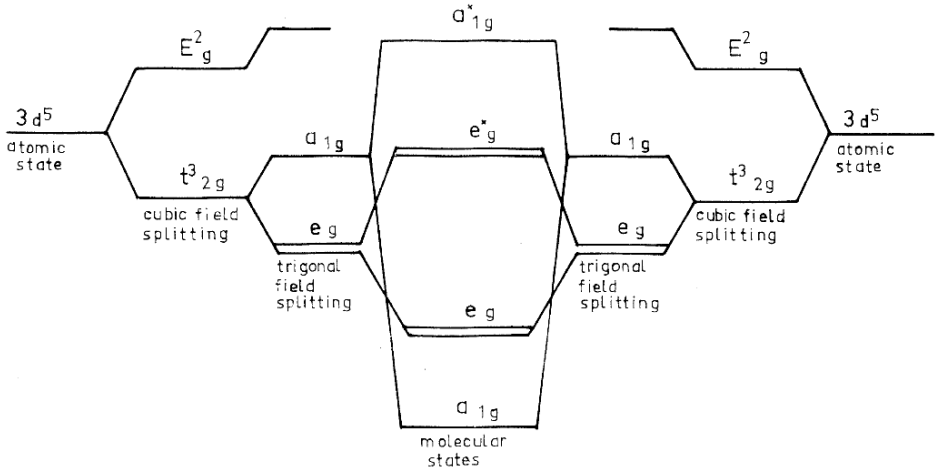

Fig. 6.3: Schematic one-electron energy level diagram of the $3d$ states in the corundum structure. Treatment of the c axis dimers as a diatomic molecule leads to the formation of molecular states, hence, an effective $S = 1/2$ system. Reproduced from Ref. [158].

More recently, an LDA and LDA+U study by Ezhov *et al.* claimed the spin 1/2 model not to be valid for V_2O_3 [161]. Their calculations result in a total spin of $S = 1$.

Only one year later, Park *et al.* [162] have shown using polarization-dependent XAS that this is indeed the case. Their most important result is shown Fig. 6.4. One can immediately see that the linear dichroism is very different in the three phases. According to Sec. 2.2 the linear dichroism is a measure for the orbital occupation. The a_{1g} orbital has lobes along the c axis of the hexagonal basis, the lobes of the e_g^π orbitals are more in the ab plane. The XAS transition probability to an empty a_{1g} or e_g^π state, thus, strongly depends on whether the polarization vector **E** of the light is parallel or perpendicular to **c** [162]. Assuming a model where part of the V sites have an $e_g^\pi e_g^\pi$ configuration, i.e., both electrons occupy the two e_g^π states, and the other part an $e_g^\pi a_{1g}$ configuration, i.e., one electron occupies the a_{1g} and the other electron one of the two e_g^π states, Park *et al.* found that the $e_g^\pi e_g^\pi$:$e_g^\pi a_{1g}$ occupation ratio is about 2:1 in the AFI, 1:1 in the PM, and 3:2 in the PI phase. Yet, for V_2O_3 to become metallic, at least 50% $e_g^\pi a_{1g}$ occupation is needed. Even though the orbital occupation changes remarkably across the phase transitions, the V^{3+} $3d^2$ ion is always in the $S = 1$ high-spin state. This ruled out the possibility of projecting out the a_{1g} orbital by means of molecular orbital formation and showed that the dimer is electronically non-existent. Interactions in the ab plane are of equal importance, in-line with

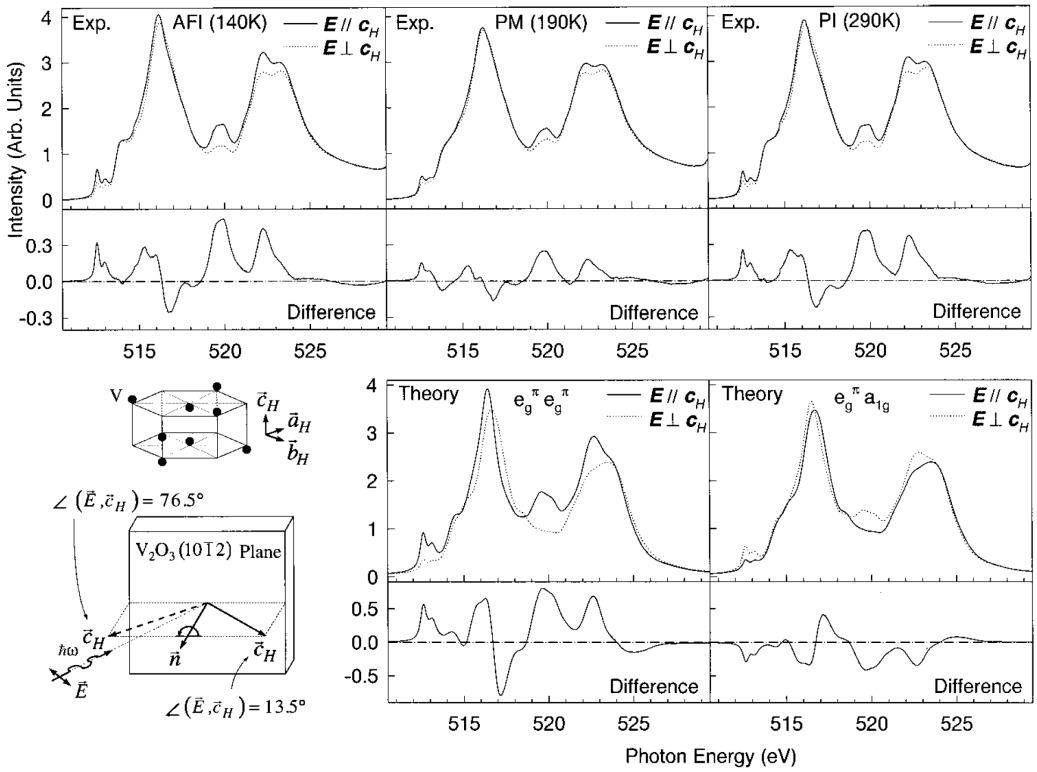

Fig. 6.4: Polarization-dependent V $L_{2,3}$ XAS of $(V_{0.988}Cr_{0.012})_2O_3$ in the AFI, PM, and PI phases taken at 140, 190, and 290 K, respectively. The bottom-middle and -right panels show theoretical spectra of the pure $e_g^\pi e_g^\pi$ and $e_g^\pi a_{1g}$ initial states. Reproduced from Ref. [162].

recent LDA results [163].

LDA+DMFT has been used to describe the electronic structure of V_2O_3, also taking many-body effects into account [164, 165, 166]. The calculations all find the V^{3+} d^2 system to be in an $S = 1$ state with reasonable values of U and an orbital occupation in agreement with the XAS results by Park *et al.*. These studies also provide predictions for the V $3d$ single particle spectral functions. For the PM phase of V_2O_3 they predict a prominent quasiparticle peak in the PES spectrum at the Fermi energy. There is a discussion whether such a peak has indeed been found in bulk-sensitive photoemission spectroscopy [167, 168] (cf. appendix 7).

The XAS results of Park et al. [162] have clearly shown that dimerization plays no important role for the electronic structure of V_2O_3. The dimer is, at least electronically, not present. However, to further strengthen this point and to discuss the importance of in-plane interactions we have studied

the electronic structure of an isolated V_2O_3 impurity by measuring the V $L_{2,3}$ XAS of the V:Al_2O_3 impurity system. By comparison of the experimental data to the result of a single-site cluster calculation we will discuss the influence of the $3d$ spin-orbit coupling and the size of the trigonal crystal field splitting. Differences between bulk and impurity spectra are interpreted in terms of substantial virtual charge fluctuations present in the electronic structure of bulk V_2O_3, with appreciable amplification of the broadening in the XAS spectra due to core hole effects.

Al_2O_3 is one of the best-known insulators (bandgap 8.8 eV [169]) and is, therefore, also discussed as a gate material in transistors [170]. Thus, the simple total electron yield detection of the XAS is not possible here. We have used the fluorescence yield detection mode instead, which is known to be very powerful for bulk-sensitive XAS measurements on diluted samples [171]. The use of V:Al_2O_3 thin films grown on metal substrates to overcome the problem of specimen charging was not possible here. With our present MBE setup we did not find any set of growth parameters resulting in crystalline Al_2O_3 films. The films always turned out to grow amorphous. The growth of crystalline Al_2O_3 thin films by MBE would presumably need growth or post-annealing at temperatures higher than 900 °C [172].

The experiments were performed at the 11A1 Dragon beamline of the NSRRC in Hsinchu, Taiwan. For the XAS measurements the photon energy resolution at the V $L_{2,3}$ edges ($h\nu \simeq 510 - 530$ eV) was set to about 0.13 eV. The XAS signal was detected using a home-made channeltron fluorescence yield detector. For details of the detector see Ref. [173]. For each scan the XAS spectrum of a YVO_3 single crystal was measured simultaneously in a separate chamber as an energy reference. The base pressure of the UHV system was below 3×10^{-10} mbar.

The V:Al_2O_3 sample (courtesy of J. W. Allen) was obtained by melting crystalline pieces of V_2O_3 and Al_2O_3 in sealed cylindrical crucibles and slowly cooling. At the measured spot the V concentration was about 1% (determined by electron-microprobe analysis), assuring the probability to have a V first nearest neighbor (c axis dimer) to be negligibly small [160].

Our experimental data obtained using the fluorescence detection is shown in the bottom panel of Fig. 6.5. Also included here for comparison is the spectrum of a thick V_2O_3 film grown on $Al_2O_3(10\bar{1}2)$ which has been shown to have bulk-like properties (cf. Appendix 7). At the very first sight the XAS spectrum of the impurity seems to be very similar to that of the thick film. However, taking a more detailed look, the features of the impurity spectrum appear much sharper than those of the thick V_2O_3 film, indicating that we are indeed in the impurity limit. The difference of the line widths of thick film and impurity spectra is much larger than one would expect from a

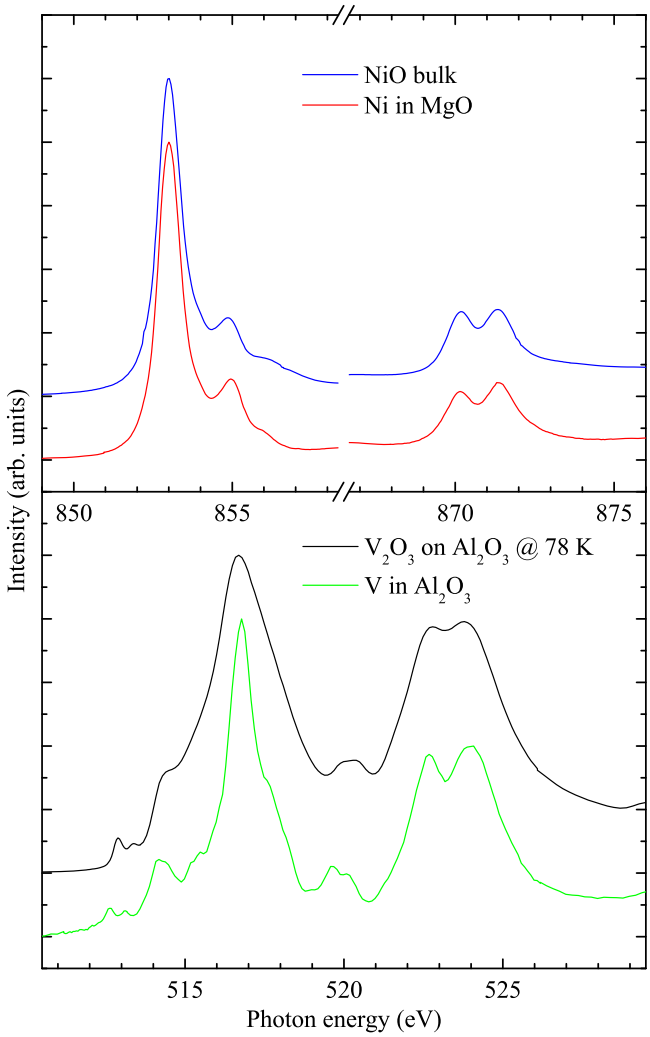

Fig. 6.5: Isotropic $L_{2,3}$ XAS spectra of V^{3+} impurities in Al_2O_3 and a thick V_2O_3 film grown on top of $Al_2O_3(10\bar{1}2)$ (bottom panel), compared to those of Ni^{2+} impurities in MgO and bulk NiO (top panel). In the top panel the energy axis is broken between the L_3 and L_2 edges to yield the same eV/cm scale in both panels for better comparability.

broadening due to band formation only. For comparison, in the top panel of Fig. 6.5 we have plotted the Ni $L_{2,3}$ XAS spectra of bulk NiO and NiO as an impurity in MgO. Note that the energy axis is broken between the L_3 and L_2 edges here to yield the same eV/cm scale in both panels of the figure. For NiO, the line widths of bulk and impurity spectra do not differ at all. This clearly indicates that intersite correlations must be very important for the

electronic structure of V_2O_3. In addition we find the spread of the spectral weight over the energy range for V:Al_2O_3 to be significantly larger than in V_2O_3. Since the atomic distances in Al_2O_3 are very different from those in V_2O_3 (both, a and c axis are considerably shorter) we expect that the local crystal fields are stronger here. This could lead to the enhancement of the spread of the spectral weight for V:Al_2O_3.

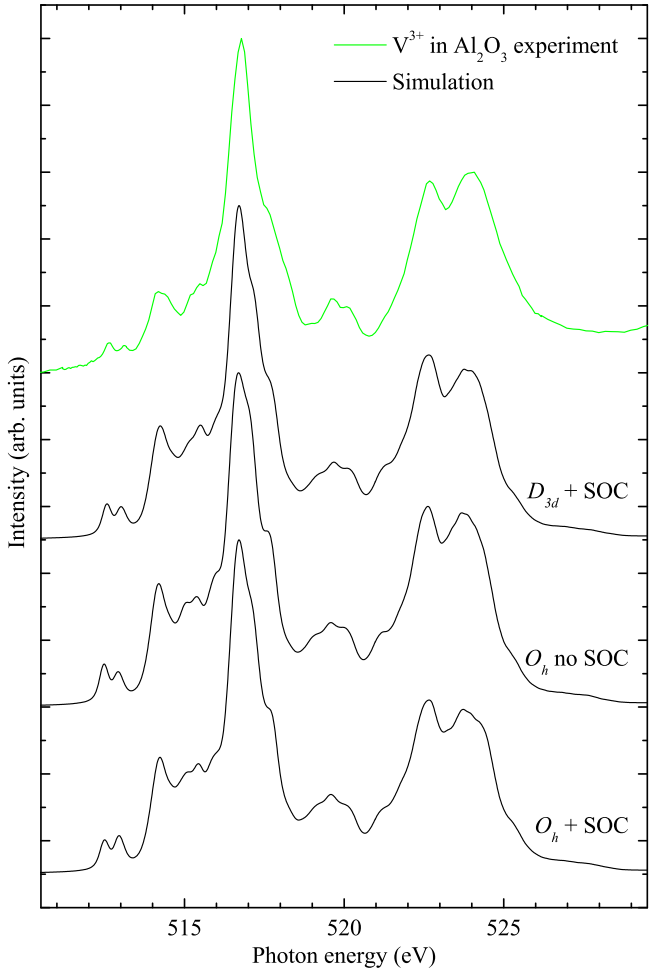

Fig. 6.6: Isotropic V $L_{2,3}$ XAS spectrum of V^{3+} impurities in Al_2O_3 compared to the result of a cluster simulation using three different parameter sets. Details and parameters of the calculation are explained in the text.

In order to extract quantitative information about the electronic structure we have simulated the experimental spectrum using the well-proven CI cluster model. Our simulations include the full-atomic multiplet theory, the $2p$ and $3d$ spin-orbit interactions, the hybridization with the oxygen ligands,

and the local crystal fields [174]. The simulations have been performed using the XTLS 8.30 code by A. Tanaka [25]. The parameters for the multipole parts of the Coulomb interaction were given by the Hartree-Fock values [30]. The monopole parts U_{dd}, U_{pd}, and the charge-transfer energy Δ have been estimated from photoemission experiments [175, 176]. Covalency was included by, besides the ionic d^2, also taking the $d^3\underline{L}$ and $d^4\underline{L}^2$ states into account, where $\underline{L}$ denotes a hole in the oxygen ligands. The parameters for the hopping integrals were calculated using the HYBRID code by T. Burnus [31]. A trigonal crystal field (D_{3d}) was accounted for by introduction of the parameters Dq, $D\sigma$, and $D\tau$ [34], in terms of D^0_{trig} and V_{mix} as defined in Chapter 1. The strength of the local crystal fields and especially that of the trigonal crystal field splitting (D^0_{trig}) has been estimated from the results of an LDA+U calculation by Hua Wu. In a first step, D^0_{trig} was calculated here for an artificial $VAlO_3$ crystal (in order to avoid direct V-V interactions) and assuming the crystal structure of Al_2O_3. The calculated trigonal crystal field splitting then is negligibly small. In the cluster simulation we have, therefore, started by assuming a local O_h symmetry. The result is shown in the bottom curve of Fig. 6.6 where we compare the experimental XAS spectrum of the V_2O_3 impurity in Al_2O_3 to the cluster simulations. The fit exhibits similarities with the experimental spectrum but a detailed comparison reveals differences. Most notably, the intensity ratio of the first two peaks at 512.5 and 512.9 eV is opposite to that of those in the experimental data. This can be fixed by switching off the spin-orbit interaction in the calculation as it is also shown in Fig. 6.6 (curve "O_h no SOC"), as it has already been done in previous calculations [162]. There is, however, no special motivation why the spin-orbit coupling should be switched off *a priori*. Thus, there must be another interaction present that overcomes the spin-orbit coupling and suppresses its contribution to the XAS spectrum. In Al_2O_3 all atomic shells are either completely full or empty. One could, therefore, imagine that the presence of a $3d$ ion such as the V^{3+} could locally strongly distort the surrounding oxygen octahedron simply due to the asymmetric shape of the $3d$ orbitals. Calculating D^0_{trig} again for the artificial $VAlO_3$ crystal but now using the crystal structure of the PI phase of V_2O_3 yields a much larger value, namely, D^0_{trig}=160 meV with a sign such that the e_g^π level is stabilized. This value is indeed much larger than the spin-orbit coupling, ζ_{3d}=27 meV. Similar values of the trigonal crystal field splitting have indeed already been found long time ago, namely, in optical spectroscopy, magnetic susceptibility, and related theoretical studies on V:Al_2O_3 [37, 38, 177, 178, 179]. A cluster simulation using this value for the trigonal crystal field splitting is also shown in Fig. 6.6, just below the experimental data ("D_{3d} + SOC"). In this scenario the ratio of the two pre-peaks is indeed correct now, and

also the overall agreement compared to the experiment is very good. All features of the spectrum can be reproduced in the simulation with the correct energy position and comparable intensity ratios. The single-site cluster model simulates the experimental XAS spectra very well. This, on the other hand, means that the differences in the spectra of bulk V_2O_3 and V_2O_3 as an impurity in Al_2O_3 must be due to the presence of intersite correlations in bulk V_2O_3. Indeed, assuming virtual charge fluctuations being present in the electronic structure of V_2O_3 would lead to extra peaks in the XAS spectrum. In a very simple model we take a look at two neighboring V^{3+} sites. Allowing for charge fluctuations with a hopping parameter t, in the ground state we can have the configurations d^2-d^2, d^1-d^3, and d^3-d^1, whereas for $U \gg t$ the latter two are higher in energy by about the Coulomb repulsion U. In the XAS final state we then also have three possible configurations, namely, the $\underline{c}d^3$-d^2, $\underline{c}d^2$-d^3, or $\underline{c}d^4$-d^1, where $\underline{c}$ denotes a core hole. Instead of only one line that we would find without charge fluctuations, the XAS spectrum would now consist of three lines at about the energies 0, $2U - Q$, and Q, where Q is the attractive core hole potential. The exact peak positions and their weights, however, strongly depend on the strengths of U, Q, and t. Whether these intersite correlations are due to dimerization or in-plane interactions cannot be judged at this point. A detailed theoretical study using a dimer or a multi-site cluster would definitely yield more insights here.

To summarize, we have measured the V $L_{2,3}$ XAS spectrum of V:Al_2O_3 using the fluorescence yield detection method. The spectrum displays sharp features and shows substantial differences compared to the spectrum of stoichiometric V_2O_3. Especially, the spectrum of stoichiometric V_2O_3 is much broader than that of V:Al_2O_3, much more than one observes in a comparison of the Ni $L_{2,3}$ XAS spectra of bulk NiO vs. NiO impurity in MgO. The impurity spectrum could be very well simulated within a single-site cluster *ansatz*, with reasonable parameter values and taking a large trigonal distortion into account. The differences between bulk and impurity spectra are interpreted in terms of substantial virtual charge fluctuations present in the electronic structure of bulk V_2O_3, with appreciable amplification of the broadening in the XAS spectra due to core hole effects.

Chapter 7

V_2O_3 thin films on Al_2O_3

Connected to our study on V^{3+} impurities in Al_2O_3 we have also carried out experimental work on stoichiometric V_2O_3 thin films grown on differently oriented Al_2O_3 substrates in a combined XAS and PES study. Depending on the film thickness one could expect the lattice mismatch of the V_2O_3 and Al_2O_3 crystal structures[1] to induce a compressive lattice strain in the V_2O_3 films, thereby stabilizing the metallic phase towards lower temperatures (cf. Fig. 6.1).

The experiments were performed at the 11A1 Dragon beamline of the NSRRC in Hsinchu, Taiwan. For the XAS measurements the photon energy resolution at the V $L_{2,3}$ edges ($h\nu \simeq 510 - 530$ eV) was set to about 0.13 eV. The degree of linear polarization of the incident light was about 99%. The XAS signal was detected by measuring the total electron yield (TEY). PES spectra were recorded using a Scienta SES-100 electron energy analyzer using 140 eV photons. The overall energy resolution was set to about 130 meV. The base pressure of the UHV system was below 3×10^{-10} mbar.

For **c** oriented samples polarization-dependent XAS spectra were recorded in a geometry in which the Poynting vector of the incoming light has an angle of $\alpha = 70°$ with respect to the **c** axis of the sample. Rotating the sample around an axis parallel to the Poynting vector allows to vary θ, the angle between the **E** vector of the light and **c**, between 20° and 90°. In this measurement geometry the optical path of the light is independent of θ, thereby allowing for a reliable comparison of spectral line shapes for different polarization directions. Spectra for $\mathbf{E} \perp \mathbf{c}$ ($I_\perp$) can be measured directly ($\theta = 90°$) while the spectra for $\mathbf{E} \parallel \mathbf{c}$ are calculated by the expression $I_\parallel = [I_p - I_\perp \cos^2(\alpha)]/\sin^2(\alpha)$. Here, I_p is the measured intensity with $\theta = 20°$,

[1] V_2O_3: a=4.95 Å, c=14.01 Å, c/a=2.83 [180].
Al_2O_3: a=4.76 Å, c=12.99 Å, c/a=2.73 [181].

and $\sin^2(\alpha) = 0.883$ and $\cos^2(\alpha) = 0.117$. Isotropic spectra are obtained from $I_{iso} = I_{\parallel} + 2 \cdot I_{\perp}$. For details of the geometry see, e.g., Ref. [182].

In the case of V_2O_3 thin films grown on **r** plane[2] oriented Al_2O_3 substrates polarization-dependent XAS data were taken using the azimuthal rotation geometry as presented in Ref. [162]. In this geometry θ can be varied between 13.5° and 76.5° ($\cos^2(\theta) = 0.95$ and $\cos^2(\theta) = 0.05$, respectively). Thus, this geometry reaches almost the perfect $\mathbf{E} \parallel \mathbf{c}$ and $\mathbf{E} \perp \mathbf{c}$ alignment such that further corrections are not needed here.

V_2O_3 thin films were grown on (0001) (*c* plane) and $(10\bar{1}2)$ (*r* plane) oriented, epi-polished Al_2O_3 substrates using MBE. The thickness of the films was estimated from deposition rates measured with a quartz crystal thickness monitor. Before film growth the substrates were annealed at 600 °C in an oxygen atmosphere of 1×10^{-7} mbar for 1 hour. High-purity V metal was evaporated from a rod (diameter 2 mm) using an Omnivac electron beam evaporator. Deposition rates ranged between 1 and 3 Å/min. During growth the substrate temperature was kept at 500 °C. Molecular oxygen was supplied through a leak valve and a nozzle and its partial pressure was monitored using a capacitance manometer. We were able to grow epitaxial and stoichiometric V_2O_3 for oxygen partial pressures ranging from 1×10^{-7} to 1×10^{-6} mbar. Orientation and epitaxy of the films was monitored during growth using reflective high energy electron diffraction (RHEED).

The line shapes of the XAS spectra depend strongly on the multiplet structure given by the atomiclike V 2*p*-3*d* and 3*d*-3*d* Coulomb and exchange interactions, as well as on local crystal fields and hybridization with the oxygen ligands [50]. The spectra display two sharp pre-peaks at around 512.7 and 513.2 eV, hardly affected by the background and solid-state broadening. For this reason, following Park *et al.* [162], we define the dichroism at the first of these peaks as the difference divided by the sum of the intensities measured for the $\mathbf{E} \parallel \mathbf{c}$ and $\mathbf{E} \perp \mathbf{c}$ geometries.

Our combined PES and XAS setup allows to directly link the metallic or insulating phase to the V 3*d* orbital occupation. In a first step we have grown V_2O_3 films with three different thicknesses of 33 Å, 50 Å, and 540 Å on *c* oriented $Al_2O_3(0001)$ substrates. The temperature-dependent valence band PES and V $L_{2,3}$ XAS spectra of these samples is shown in Fig. 7.1.

[2]The $(10\bar{1}2)$ plane of the corundum structure is the primary natural cleavage plane for many corundum compounds like Ti_2O_3, V_2O_3, or Cr_2O_3, but not for Al_2O_3, corundum itself [183].

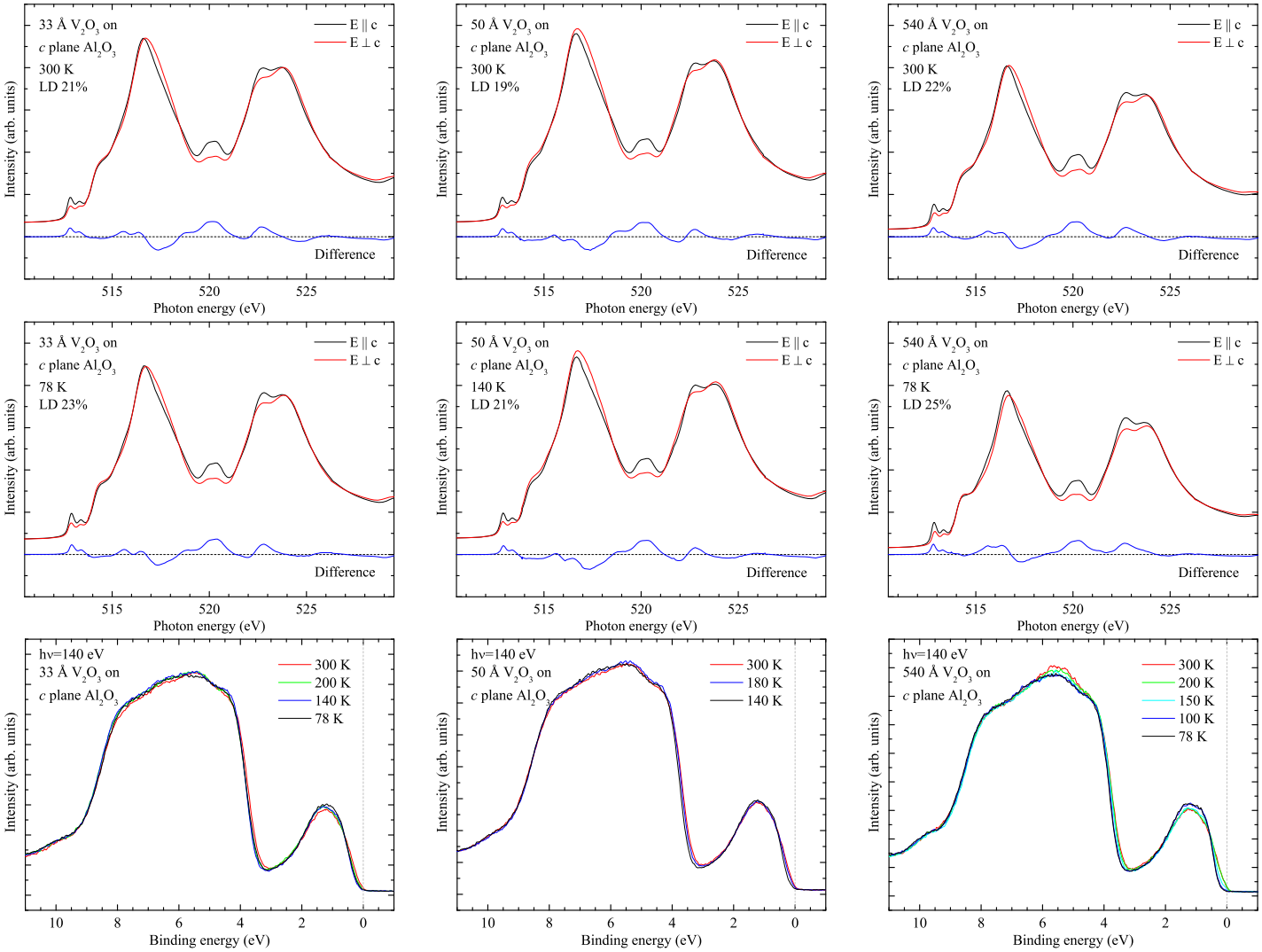

Fig. 7.1: Top two panels: Polarization-dependent V $L_{2,3}$ XAS of 33 Å (left), 50 Å (middle), and 540 Å (right) V_2O_3 on $Al_2O_3(0001)$ in the high and low temperature phase. Bottom panels: Temperature-dependent valence band PES spectra.

We first discuss the PES data. The spectra are basically divided into two parts. The intense broad peak between about 4 and 9 eV binding energy can be identified with the O $2p$ contribution to the valence band. The spectral weight between 0 and 4 eV has predominantly V $3d$ character. In our discussion we now focus on the latter, $3d$ related part of the spectrum. Looking first at the spectra for all three samples we find that our V_2O_3 thin films are always insulating, independent on the film thickness and temperature. For none of the samples we find a spectral weight at the Fermi level, which would indicate a metallic system. For the thick film (right panels in Fig. 7.1) we see some indication of transfer of spectral weight to lower binding energies above 150 K, but the sample remains insulating. The PES results is consistent with the V $L_{2,3}$ XAS. For all three samples the XAS spectra show a pronounced polarization-dependence. The linear dichroism at low temperatures is always slightly higher. Comparing the spectra and their polarization-dependence to the results of Park *et al.* [162] we can identify our spectra with one of those of the two insulating phases of V_2O_3. The spectrum of the metallic phase (Fig. 6.4) is clearly different.

The XAS results are, thus, consistent with the PES data. At present, we are not able to explain why the V_2O_3 films on $Al_2O_3(0001)$ show no metallic phase at least at room temperature. However, the corundum (0001) surface poses conceptual problems since the atomic layers normal to the c axis contain either only cations or only anions [183]. It is a polar surface [184]. These surfaces are, thus, expected to relax or reconstruct in some way to compensate for the otherwise diverging electrical potential. Probably, films considerably thicker than 540 Å are required to approach the bulk limit and stabilize the metallic phase at room temperature.

When growing V_2O_3 on $Al_2O_3(0001)$ the lattice strain is only in the ab plane. Alternatively, we have also grown V_2O_3 films on r plane oriented $Al_2O_3(10\bar{1}2)$ substrates where the lattice compression also acts in the c direction. In addition, the corundum r plane is non-polar. The XAS and PES results for a thin (50 Å) and a thick (240 Å) V_2O_3 film grown on $Al_2O_3(10\bar{1}2)$ is shown in Fig. 7.2.

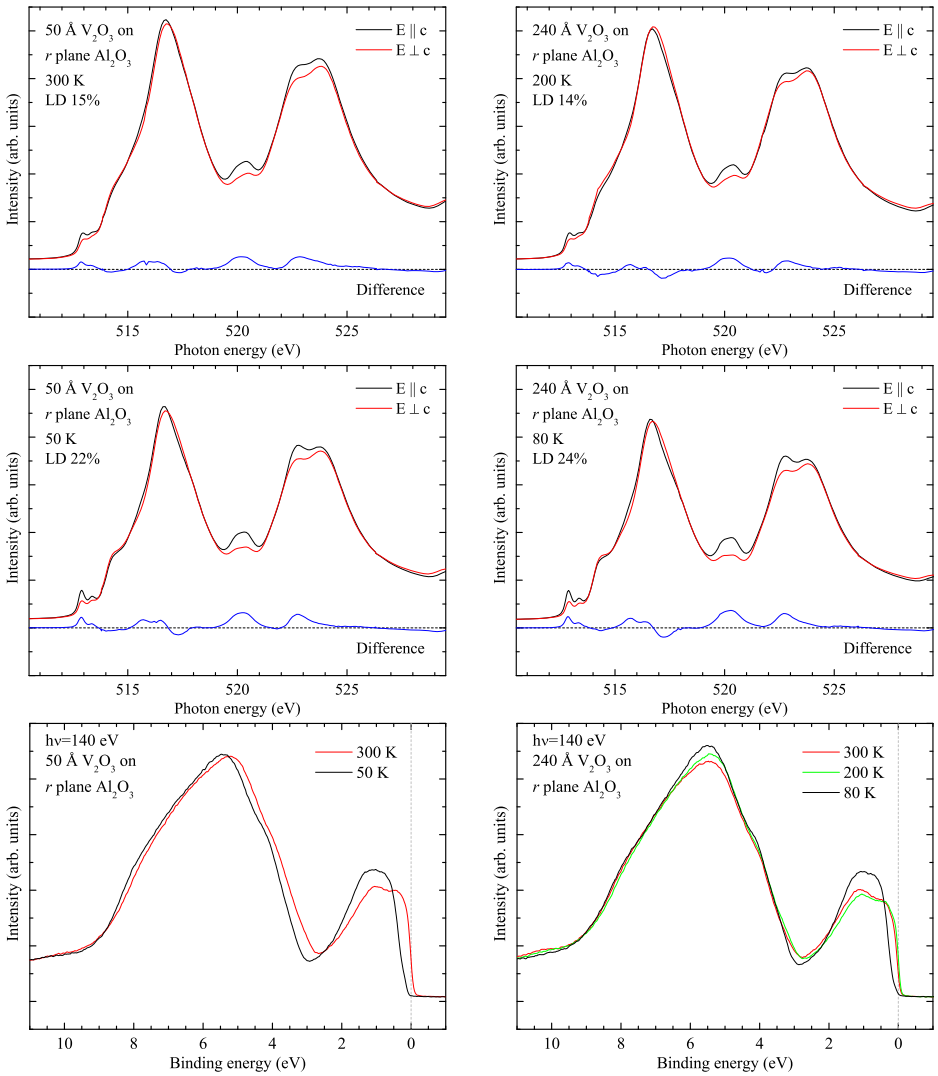

Fig. 7.2: Top two panels: Polarization-dependent V $L_{2,3}$ XAS of 50 Å (left), and 240 Å (right) V_2O_3 on $Al_2O_3(10\bar{1}2)$ in the high and low temperature phase. Bottom panels: Temperature-dependent valence band PES spectra.

Again, we first discuss the valence band PES data. For the films grown on r plane Al_2O_3 the PES spectra show a strong temperature dependence. At low temperatures they have a line shape very similar to that of the V_2O_3 on $Al_2O_3(0001)$ spectra. In contrast, at high temperatures the spectra are very different. We clearly see intensity emerging at the Fermi level, indicating a metallic state. We identify this peak, even if the intensity is much lower due to the reduced probing depth at 140 eV photon energy, as the quasiparticle peak also found in the metallic phase of bulk V_2O_3 [167, 168]. The PES results are again inline with the XAS results also shown in Fig. 7.2. At low temperatures we find again a pronounced polarization dependence with a linear dichroism comparable to that of the samples grown on $Al_2O_3(0001)$. In contrast, the spectral line shape of the high-temperature spectra is clearly different now and also the polarization dependence is a lot reduced.

The V_2O_3 thin films grown on $Al_2O_3(10\bar{1}2)$, thus, behave much more like the bulk V_2O_3 system. Note that we found no indication for another insulating phase at even higher temperatures up to 400 K.

In conclusion, we have successfully grown V_2O_3 thin films on $Al_2O_3(0001)$ and $Al_2O_3(10\bar{1}2)$ in an epitaxial fashion. The films grown on c plane oriented substrates behave very surprisingly, partially in contradiction to other studies [185, 186]. Both, our PES and polarization-dependent XAS spectra clearly show an insulating phase at all temperatures measured. V_2O_3 films grown on r plane oriented substrates, however, show a more bulk-like behavior: They are metallic at high and insulating at low temperatures. However, the unexpected behavior of the V_2O_3 films on $Al_2O_3(0001)$ cannot be explained at present. To solve this problem an even more detailed experimental study would be needed. Such as study would have to combine microscopic (PES, XAS) and macroscopic (transport, magnetism) information on the electronic structure, together with a careful study of the crystal structure (RHEED, LEED, XRD).

Summary

In terms of materials, most of the modern electronic devices are still based on the electrical properties of metals and semiconductors. Yet, the class of transition metal compounds and, especially, transition metal oxides shows a variety of spectacular physical effects like, e.g., high-temperature superconductivity, the giant or tunnel magneto resistance, spin-polarized transport, metal to insulator transitions, or multiferroic order. If ways could be found to make use of these phenomena, one could obtain devices with unprecedented functionalities. This, however, requires tuning of the material properties, and this in turn a profound understanding of the electronic structure of these compounds. In contrast to simple metals and semiconductors where a mean-field one-electron description is typically sufficient, electron-electron correlations are very important here, thereby requiring a more sophisticated theoretical *ansatz*. Since an exact treatment is impossible due to the huge number of degrees of freedom one has to use approximations or simplified model systems. An effective first order approach to take these correlation effects into account is to neglect the translational symmetry of the real crystal and to describe the electronic structure in a local single-site impurity model. This is done for example in the so-called configuration-interaction cluster calculations where the system is reduced to a single ion and its ligands. The underlying idea is that the ground state and near ground state properties as well as the excitation spectra can be described on an equal footing as far as the many body aspects are concerned. One of the latest and most sophisticated development in theoretical solid state physics, namely, the dynamical mean-field theory (DMFT) is also based on this idea. Yet, it is not always easy to judge about the applicability of the results for the real bulk systems. An experimental test is highly desired.

In this thesis we have, therefore, set out to study the electronic structure of selected transition metal impurities in oxides using photoemission (PES) and x-ray absorption spectroscopy (XAS). These systems have already been very popular in the past for electron spin-resonance and optical spectroscopy experiments yielding valuable information on energy levels and crystal fields.

Modern spectroscopic techniques together with the availability of synchrotron radiation now allow us to investigate their electronic structure with unprecedented detail. We have simulated our experimental data using a single-site cluster model and compare the results to the respective bulk systems.

In Chapter 3 we report on a comparative study of the valence band electronic structure of NiO as bulk material and of NiO as impurity in MgO. From the impurity we have been able to determine reliably the parameters which describe the local correlations, thereby establishing the compensated-spin character of the first ionization state or the state created by hole doping. Using bulk-sensitive hard x-ray photoemission (HAXPES) we identify features which cannot be explained by single-site many body approaches nor by mean-field calculations. We infer the presence of screening processes involving local quasi-core states in the valence band and non-local coherent many body states.

Chapter 4 deals with the local electronic structure of Fe impurities in MgO thin films. Using XAS we verified that the Fe impurities are all in the 2+ valence state. The fine details in the line shape of the Fe $L_{2,3}$ edges provide direct evidence for the presence of a dynamical Jahn-Teller distortion. We were able to determine the magnitude of the effective D_{4h} crystal field energies. We also observed a strong temperature dependence in the spectra which we can attribute to the thermal population of low-lying excited states that are present due to the spin-orbit coupling in the Fe $3d$. Using this Fe^{2+} impurity system as an example, we show that an accurate measurement of the orbital moment in Fe_3O_4 will provide a direct estimate for the effective local low-symmetry crystal fields on the Fe^{2+} sites, important for the theoretical modeling of the formation of orbital ordering.

The local single-site description is very successful in the case of MnO and Mn impurities in MgO which is treated in Chapter 5. Here, we have studied the electronic structure of MnO and Mn impurities in MgO thin films grown on Ag substrates by molecular beam epitaxy (MBE) using XAS and PES. By comparison of the XAS spectrum of bulk MnO to that of the thin film grown on Ag we have shown that the Ag substrate is able to compensate for specimen charging due to the photo-excitation process. We have found that the Mn $L_{2,3}$ spectra of MnO thin films grown on Ag provide a well defined data set for comparison to theory. We were able to explain differences in the Mn $L_{2,3}$ spectra of the MnO impurity and bulk MnO by fitting the experimental data using a cluster model taking the different magnitude of the local crystal fields in MnO and MgO into account. We were able to measure and extract the MnO impurity valence band photoemission spectrum by using 140 eV photons. Very much unlike the NiO case, here the impurity valence band spectrum shows only small differences to the bulk spectrum

which could also be explained by the cluster model and the different local crystal fields in both compounds.

The importance of intersite effects in the electronic structure of V_2O_3 is the topic of Chapter 6. Here, we have measured the V $L_{2,3}$ XAS spectrum of V^{3+} impurities in bulk Al_2O_3 using the fluorescence yield detection method. The spectrum exhibits substantial differences compared to that of stoichiometric V_2O_3. The latter is much broader than that of the impurity, much more than one observes in a comparison of the Ni $L_{2,3}$ XAS spectra of bulk NiO vs. NiO impurity in MgO. The V in Al_2O_3 spectrum can be very well simulated within a single-site cluster *ansatz*, with reasonable parameter values and taking a large trigonal distortion into account. The differences between bulk and impurity spectra are interpreted in terms of substantial virtual charge fluctuations present in the electronic structure of bulk V_2O_3, with appreciable amplification of the broadening in the XAS spectra due to core hole effects.

In conclusion, transition metal impurities in oxides are fundamental model systems to study the electronic structure of strongly correlated oxides. A detailed study of their electronic structure yields essential information on the importance of local and non-local interactions in the associated bulk compounds and even more complicated materials.

Zusammenfassung

Die Funktionsweise moderner elektronischer Geräte basiert noch immer weitestgehend auf den elektronischen Eigenschaften von einfachen Metallen und Halbleitern. Die Klasse der Übergangsmetallverbindungen hingegen und insbesondere die Übergangsmetalloxide weisen eine Vielzahl spektakulärer physikalischer Eigenschaften auf. So zeigen Sie z.B. Hochtemperatursupraleitung, den Riesen- oder Tunnelmagnetwiderstand, Spin-polarisierten Transport, Metall-Isolator Übergänge oder multiferroische Ordnung. Die technische Nutzung dieser Phänomene würde einen Zugang zu Geräten mit nie dagewesenen Eigenschaften ermöglichen. Diese allerdings erfordert die gezielte Manipulation von Materialeigenschaften, und diese wiederum ein tiefgehendes Verständnis der elektronischen Struktur dieser Verbindungen. Während die wichtigsten Eigenschaften von einfachen Metallen und Halbleitern in einem Einelektronenmodell ausreichend beschrieben werden können, sind Elektron-Elektron Wechselwirkungen hier sehr ausgeprägt und erfordern eine anspruchsvollere und detailliertere theoretische Behandlung. Die große Anzahl der möglichen Freiheitsgrade macht eine exakte theoretische Beschreibung jedoch unmöglich, und man muss sich geeigneter Näherungsmethoden oder Modellsysteme bedienen. In einem weit verbreiteten und sehr erfolgreichen Ansatz zur Berücksichtigung dieser Korrelationseffekte wird die Translationssymmetrie eines realen Kristalls vollkommen vernachlässigt. Stattdessen wird die lokale elektronische Struktur einer einzigen isolierten Störstelle beschrieben. Diesen Ansatz verfolgen sog. *configuration-interaction* Clusterrechnungen, in denen der Festkörper auf ein einzelnes Ion nebst den dazugehörigen Liganden reduziert wird. Die zugrunde liegende Idee ist, dass hier Grundzustands- und Nahgrundzustandseigenschaften sowie Anregungsspektren im Hinblick auf Korrelationseffekte gleichberechtigt behandelt werden können. Auch eine der am weitesten fortgeschrittenen Methoden der theoretischen Festkörperphysik, die dynamische Mean-Field Theorie (DMFT), basiert auf diesem Ansatz. Trotzdem ist es oft nicht leicht zu beurteilen, wie gut die Ergebnisse und Modellparameter auf reale, ausgedehnte Systeme übertragbar sind. Ein experimenteller Test wäre

daher sehr wünschenswert.

Diese Arbeit beschäftigt sich aus diesem Grund mit der Untersuchung der elektronischen Struktur von Übergangsmetall-Störstellen in Oxiden mittels Photoemissions- (PES) und Röntgenabsorptionsspektroskopie (XAS). Bereits in der Vergangenheit lieferten solche Systeme in optischen Absorptions- und Elektronenspinresonanzexperimenten wichtige Informationen zu Energiezuständen und Kristallfeldern. Moderne spektroskopische Methoden und die Verfügbarkeit von Synchrotronstrahlung erlauben es uns heute, die elektronische Struktur dieser Systeme weitaus detaillierter zu untersuchen. Die gewonnenen experimentellen Daten wurden im Rahmen von Clusterrechnungen simuliert, und die Ergebnisse mit den zugehörigen Volumensystemen verglichen.

Kapitel 3 berichtet über eine Vergleichsstudie der elektronischen Struktur des Valenzbandes von NiO als Volumenkristall und als Störstelle in MgO. Das Störstellensystem erlaubt eine verlässliche Bestimmung der Modellparameter, die die lokalen Korrelationseffekte beschreiben. Dadurch konnte der kompensierte Spinzustand des ersten Ionisierungszustandes bzw. eines durch Lochdotierung hervorgerufenen Zustandes bestätigt werden. Mit Hilfe volumenempfindlicher Photoemissionsspektroskopie mit harter Röntgenstrahlung (HAXPES) konnten im Valenzbandspektrum von NiO Strukturen nachgewiesen werden, die weder mit Vielteilchen-Störstellenrechnungen noch mit Mean-Field Methoden zu erklären sind. Zur Erklärung werden Abschirmprozesse vorgeschlagen, die mit der Existenz von lokalen, Rumpniveauartigen Zuständen und nichtlokalen, kohärenten Vielteilchenzuständen einhergehen.

Kapitel 4 beschäftigt sich mit der elektronischen Struktur von Fe Störstellen in MgO. Mittels XAS wurde hier festgestellt, dass sämtliche Störstellen zweiwertig vorliegen. Die Fe $L_{2,3}$ Absorptionskanten weisen scharfe Strukturen auf, die Rückschlüsse auf das Vorhandensein einer dynamischen Jahn-Teller Verzerrung erlauben. Die Stärke des effektiven D_{4h} Kristallfeldes konnte abgeschätzt werden. Zusätzlich zeigen die Absorptionsspektren eine ausgeprägte Temperaturabhängigkeit, die eindeutig auf die thermische Besetzung tief liegender angeregter Zustände zurückgeführt werden konnte, die aufgrund der Spin-Bahn-Aufspaltung der Fe $3d$ Orbitale vorliegen. Beispielhaft wird an diesem Fe^{2+} System gezeigt, dass eine genaue Messung des orbitalen magnetischen Momentes in Fe_3O_4 direkten Zugang zur Abschätzung der lokalen effektiven Kristallfelder niedriger Symmetrie an den Fe^{2+} Plätzen bietet, eine wichtige Information zur theoretischen Modellierung orbitaler Ordnung.

Die Untersuchung von MnO und MnO als Störstelle in dünnen Filmen aus MgO zeigt, dass hier das lokale Störstellenmodell zur Beschreibung der

elektronischen Struktur sehr erfolgreich ist (Kapitel 5). Hier wurde deren elektronische Struktur mittels PES und XAS studiert. Zunächst wird durch einen Vergleich der Absorptionsspektren von MnO als Volumenkristall und dem eines dünnen MnO Filmes, der mittels Molekularstrahlepitaxie (MBE) auf ein Ag Substrat aufgebracht wurde, gezeigt, dass das metallische Substrat tatsächlich eine durch den Anregungsprozess bedingte Aufladung des Oxidfilms kompensieren kann. Die Absorptionsspektren eines auf ein Ag Substrat aufgebrachten MnO Films eignen sich daher hervorragend als wohl definierter Datensatz zum Vergleich mit Simulationen. Unterschiede in den Absorptionsspektren von MnO und MnO als Störstelle in MgO wurden im Rahmen einer Clusterrechnung erklärt, die die unterschiedlich starken lokalen Kristallfelder in MnO und MgO berücksichtigt. Mit Hilfe von Photoemissionsmessungen bei einer Photonenenergie von 140 eV war es möglich, das Valenzbandspektrum einer MnO Störstelle zu messen und zu extrahieren. Ganz im Gegensatz zu NiO, zeigen die Valenzbandspektren von Störstelle und Volumenkristall hier nur geringfügige Unterschiede, die wiederum mit den unterschiedlich starken Kristallfeldern erklärt werden konnten.

Die Bedeutung von nichtlokalen Effekten für die elektronische Struktur von V_2O_3 wird in Kapitel 6 behandelt. In diesem Zusammenhang wurde das V $L_{2,3}$ Röntgenabsorptionsspektrum von V^{3+} Störstellen in Al_2O_3 mit Hilfe der Fluoreszenzdetektion gemessen. Im Vergleich zum Spektrum eines V_2O_3 Volumenkristalls fallen deutliche Unterschiede auf. Insbesondere sind die Spektrallinien des Volumensystems wesentlich breiter, und zwar deutlich mehr als man es in einem Vergleich der Ni $L_{2,3}$ Absorptionskanten von NiO als Volumenkristall und NiO als Störstelle in MgO beobachtet. Mit Hilfe einer Clusterrechnung, die auch ein vergleichsweise starkes, trigonales Kristallfeld berücksichtigt, konnte das Spektrum des V:Al_2O_3 Störstellensystems sehr gut reproduziert werden. Die Unterschiede in den Spektren von Störstellen- und Volumensystem wurden daher auf das Vorhandensein erheblicher virtueller Ladungsfluktuationen in Letzterem zurückgeführt, die zu einer deutlichen Verbreiterung der XAS Spektren durch sog. *core hole* Effekte führen.

Zusammenfassend sind Übergangsmetall-Störstellen in Oxiden fundamentale Modellsysteme zur Untersuchung der elektronischen Struktur stark korrelierter Oxide. Ihre detaillierte Untersuchung liefert essentielle Informationen über den Einfluss lokaler und nicht-lokaler Wechselwirkungen in den zugehörigen Volumensystemen oder weitaus komplizierteren Verbindungen.

Bibliography

[1] Bardeen, J. and Brattain, W. H. *The Transistor, A Semi-Conductor Triode.* Phys. Rev. **74**, 230 (1948).

[2] Packan, P. et al. *High performance 32nm logic technology featuring 2nd generation high-k + metal gate transistors.* Electron Devices Meeting (IEDM), 2009 IEEE International 1–4 (2009).

[3] Miyazaki, T. and Tezuka, N. *Giant magnetic tunneling effect in* $Fe/Al_2O_3/Fe$ *junction.* J. Magn. Magn. Mater. **139**, L231 (1995).

[4] Gregg, J. F. *Spintronics: A growing science.* Nat. Mater. **6**, 798 (2007).

[5] Schmehl, A. et al. *Epitaxial integration of the highly spin-polarized ferromagnetic semiconductor EuO with silicon and GaN.* Nat. Mater. **6**, 882 (2007).

[6] Imada, M., Fujimori, A. and Tokura, Y. *Metal-insulator transitions.* Rev. Mod. Phys. **70**, 1039 (1998).

[7] Spaldin, N. A. and Fiebig, M. *The Renaissance of Magnetoelectric Multiferroics.* Science **309**, 391 (2005).

[8] Kotliar, G. and Vollhardt, D. *Strongly Correlated Materials: Insights From Dynamical Mean-Field Theory.* Phys. Today **57**, 53 (2004).

[9] de Boer, J. H. and Verwey, E. J. W. *Semi-conductors with partially and with completely filled 3 d -lattice bands.* Proc. Phys. Soc. **49**, 59 (1937).

[10] Ashcroft, N. W. and Mermin, I. *Solid State Physics* (Thomson Learning, Inc., 1976).

[11] Hohenberg, P. and Kohn, W. *Inhomogeneous Electron Gas.* Phys. Rev. **136**, B864 (1964).

[12] Kohn, W. and Sham, L. J. *Self-Consistent Equations Including Exchange and Correlation Effects.* Phys. Rev. **140**, A1133 (1965).

[13] Terakura, K., Williams, A. R., Oguchi, T. and Kübler, J. *Transition-Metal Monoxides: Band or Mott Insulators.* Phys. Rev. Lett. **52**, 1830 (1984).

[14] Ching, W. Y., Xu, Y.-N. and Wong, K. W. *Ground-state and optical properties of Cu_2O and CuO crystals.* Phys. Rev. B **40**, 7684 (1989).

[15] Oguchi, T., Terakura, K. and Williams, A. R. *Band theory of the magnetic interaction in MnO, MnS, and NiO.* Phys. Rev. B **28**, 6443 (1983).

[16] Terakura, K., Oguchi, T., Williams, A. R. and Kübler, J. *Band theory of insulating transition-metal monoxides: Band-structure calculations.* Phys. Rev. B **30**, 4734 (1984).

[17] Svane, A. and Gunnarsson, O. *Transition-metal oxides in the self-interaction–corrected density-functional formalism.* Phys. Rev. Lett. **65**, 1148 (1990).

[18] Fujimori, A. and Minami, F. *Valence-band photoemission and optical absorption in nickel compounds.* Phys. Rev. B **30**, 957 (1984).

[19] Sawatzky, G. A. and Allen, J. W. *Magnitude and Origin of the Band Gap in NiO.* Phys. Rev. Lett. **53**, 2339 (1984).

[20] Altland, A. and Simons, B. *Condensed Matter Field Theory* (Cambridge University Press, Cambridge, 2006).

[21] Lieb, E. H. and Wu, F. Y. *Absence of Mott Transition in an Exact Solution of the Short-Range, One-Band Model in One Dimension.* Phys. Rev. Lett. **20**, 1445 (1968).

[22] van Dongen, P. and Vollhardt, D. *Exact solution and thermodynamics of the Hubbard model with infinite-range hopping.* Phys. Rev. B **40**, 7252 (1989).

[23] Zaanen, J., Sawatzky, G. A. and Allen, J. W. *Band gaps and electronic structure of transition-metal compounds.* Phys. Rev. Lett. **55**, 418 (1985).

[24] Koethe, T. C. *Bulk sensitive Photoelectron Spectroscopy of strongly correlated transition metal oxides*. Ph.D. thesis, Universität zu Köln (2007).

[25] Tanaka, A. and Jo, T. *Resonant 3d, 3p and 3s Photoemission in Transition Metal Oxides Predicted at 2p Threshold*. J. Phys. Soc. Jpn. **63**, 2788 (1994).

[26] Fujimori, A., Bocquet, A. E., Saitoh, T. and Mizokawa, T. *Electronic structure of 3d transition metal compounds: systematic chemical trends and multiplet effects*. Journal of Electron Spectroscopy and Related Phenomena **62**, 141 (1993).

[27] Bocquet, A. E., Mizokawa, T., Saitoh, T., Namatame, H. and Fujimori, A. *Electronic structure of 3d-transition-metal compounds by analysis of the 2p core-level photoemission spectra*. Phys. Rev. B **46**, 3771 (1992).

[28] Ozawa, T. C. and Kang, S. J. *Balls & Sticks: Easy-to-Use Structure Visualization and Animation Creating Program*. Appl. Cryst. **37**, 679 (2004).

[29] de Groot, F. M. F. *X-ray absorption and dichroism of transition metals and their compounds*. J. Electron. Spectrosc. Relat. Phenom. **67**, 529 (1994).

[30] Haverkort, M. W. *Spin and orbital degrees of freedom in transition metal oxides and oxide thin films studied by soft x-ray absorption spectroscopy*. Ph.D. thesis, Universität zu Köln (2005).

[31] Burnus, T. *Study of Charge, Spin and Orbital States in Novel Transition-Metal Oxides Using X-Ray Absorption Spectroscopy*. Ph.D. thesis, Universität zu Köln (2008).

[32] Slater, J. C. and Koster, G. F. *Simplified LCAO Method for the Periodic Potential Problem*. Phys. Rev. **94**, 1498 (1954).

[33] Thole, B. T., Cowan, R. D., Sawatzky, G. A., Fink, J. and Fuggle, J. C. *New probe for the ground-state electronic structure of narrow-band and impurity systems*. Phys. Rev. B **31**, 6856 (1985).

[34] Ballhausen, C. J. *Introduction to ligand field theory* (McGraw-Hill, New York, 1962).

[35] Gunnarsson, O. and Jepsen, O. *Configuration dependence of hopping matrix elements in the Anderson model*. Phys. Rev. B **38**, 3568 (1988).

[36] Okada, K. and Kotani, A. *Effects of configuration-dependent hybridization on core-level photoemission spectra.* J. Electron. Spectrosc. Relat. Phenom. **71**, R1 (1995).

[37] McClure, D. S. *Optical Spectra of Transition-Metal Ions in Corundum.* J. Chem. Phys. **36**, 2757 (1962).

[38] Brumage, W. H., Quade, C. R. and Lin, C. C. *Magnetic Susceptibilities of Transition Elements in Host Crystals. I. V^{3+} in Corundum.* Phys. Rev. **131**, 949 (1963).

[39] Ham, F. S., Schwarz, W. M. and O'Brien, M. C. M. *Jahn-Teller Effects in the Far-Infrared, EPR, and Mössbauer Spectra of MgO: Fe^{2+}.* Phys. Rev. **185**, 548 (1969).

[40] Abragam, A. and Bleaney, B. *Electron paramagnetic resonance of transitionion ions* (Oxford University Press, London, 1970).

[41] Altieri, S., Tjeng, L. H. and Sawatzky, G. A. *Electronic structure and chemical reactivity of oxide-metal interfaces: MgO(100)/Ag(100).* Phys. Rev. B **61**, 16948 (2000).

[42] Venables, J. A., Spiller, G. D. T. and Hanbucken, M. *Nucleation and growth of thin films.* Rep. Prog. Phys. **47**, 399 (1984).

[43] Herman, M. A., Richter, W. and Sitter, H. *Epitaxy: physical principles and technical implementation*, vol. 64 of *Springer Series in Materials Science* (Springer, Berlin, 2004).

[44] Norton, D. P. *Synthesis and properties of epitaxial electronic oxide thin-film materials.* Mater. Sci. Eng., R **43**, 139 (2004).

[45] Sutarto, R. et al. *Epitaxial and layer-by-layer growth of EuO thin films on yttria-stabilized cubic zirconia (001) using MBE distillation.* Phys. Rev. B **79**, 205318 (2009).

[46] Gudat, W. and Kunz, C. *Close Similarity between Photoelectric Yield and Photoabsorption Spectra in the Soft-X-Ray Range.* Phys. Rev. Lett. **29**, 169 (1972).

[47] Pedio, M. et al. *Covalency in oxygen chemisorption as probed by x-ray absorption.* Phys. Rev. B **40**, 7924 (1989).

[48] Himpsel, F. J. et al. *Fine structure of the Ca 2p x-ray-absorption edge for bulk compounds, surfaces, and interfaces.* Phys. Rev. B **43**, 6899 (1991).

[49] Jaklevic, J. et al. *Fluorescence detection of EXAFS: Sensitivity enhancement for dilute species and thin films.* Solid State Commun. **23**, 679 (1977).

[50] de Groot, F. *Multiplet effects in X-ray spectroscopy.* Coord. Chem. Rev. **249**, 31 (2005).

[51] Thole, B. T. and van der Laan, G. *Branching ratio in x-ray absorption spectroscopy.* Phys. Rev. B **38**, 3158 (1988).

[52] Chen, C. T. et al. *Out-of-plane orbital characters of intrinsic and doped holes in* $La_{2-x}Sr_xCuO_4$. Phys. Rev. Lett. **68**, 2543 (1992).

[53] Thole, B. T., Carra, P., Sette, F. and van der Laan, G. *X-ray circular dichroism as a probe of orbital magnetization.* Phys. Rev. Lett. **68**, 1943 (1992).

[54] Carra, P., Thole, B. T., Altarelli, M. and Wang, X. *X-ray circular dichroism and local magnetic fields.* Phys. Rev. Lett. **70**, 694 (1993).

[55] Reinert, F. and Hüfner, S. *Photoemission spectroscopy - from early days to recent applications.* New J. Phys. **7**, 97 (2005).

[56] Einstein, A. *Über einen die Erzeugung und Verwandlung des Lichtes betreffenden heuristischen Gesichtspunkt.* Ann. Phys. **17**, 132 (1905).

[57] Hertz, H. R. *Über einen Einfluß des ultravioletten Lichtes auf die electrische Entladung.* Ann. Phys. **31**, 983 (1887).

[58] Hallwachs, W. *Über den Einfluß des Lichtes auf electrostatisch geladene Körper.* Ann. Phys. **33**, 301 (1888).

[59] Yeh, J. J. and Lindau, I. *Atomic subshell photoionization cross sections and asymmetry parameters:* $1 \leq Z \leq 103$. At. Data Nucl. Data Tables **32**, 1 (1985).

[60] Sawatzky, G. A. and Post, D. *X-ray photoelectron and Auger spectroscopy study of some vanadium oxides.* Phys. Rev. B **20**, 1546 (1979).

[61] Cooper, J. W. *Photoionization from Outer Atomic Subshells. A Model Study.* Phys. Rev. **128**, 681 (1962).

[62] Seah, M. P. and Dench, W. A. *Quantitative electron spectroscopy of surfaces: A standard data base for electron inelastic mean free paths in solids*. Surf. Interface Anal. **1**, 2 (1979).

[63] NSRRC. *Synchrotron Radiation* (2010). URL `http://www.nsrrc.org.tw/english/lightsource.aspx`. [Accessed 2010-03-17].

[64] Thompson, A. C. et al. *X-RAY DATA BOOKLET* (Lawrence Berkeley National Laboratory, Berkeley, California, 2001), 2nd edn.

[65] Liénard, A. *Produit par une charge électrique concentrée en un point et animée d'un mouvement quelconque*. L'Éclairage Électrique **16**, 5 (1898).

[66] Elder, F. R., Gurewitsch, A. M., Langmuir, R. V. and Pollock, H. C. *Radiation from Electrons in a Synchrotron*. Phys. Rev. **71**, 829 (1947).

[67] Gullikson, E. *Bend Magnet Spectrum* (2010). URL `http://henke.lbl.gov/optical_constants/bend2.html`. [Accessed 2010-03-17].

[68] Chen, C. T. and Sette, F. *Performance of the Dragon soft x-ray beamline (invited)*. Rev. Sci. Instrum. **60**, 1616 (1989).

[69] Chen, C. T. and Sette, F. *High Resolution Soft X-Ray Spectroscopies with the Dragon Beamline*. Phys. Scr. **T31**, 119 (1990).

[70] Tsang, K. L. and Chen, C. T. *Dragon-type Beamlines*. NSRRC Activity Report 141 (2002/2003).

[71] Roth, W. L. *Magnetic Structures of MnO, FeO, CoO, and NiO*. Phys. Rev. **110**, 1333–1341 (1958).

[72] Mott, N. F. *The Basis of the Electron Theory of Metals, with Special Reference to the Transition Metals*. Proc. Phys. Soc. London, Sect. A **62**, 416 (1949).

[73] Hubbard, J. *Electron Correlations in Narrow Energy Bands*. Proc. R. Soc. London, Ser. A **276**, 238–257 (1963).

[74] Anisimov, V. I., Zaanen, J. and Andersen, O. K. *Band theory and Mott insulators: Hubbard U instead of Stoner I*. Phys. Rev. B **44**, 943–954 (1991).

[75] van Elp, J., Eskes, H., Kuiper, P. and Sawatzky, G. A. *Electronic structure of Li-doped NiO.* Phys. Rev. B **45**, 1612–1622 (1992).

[76] Almbaldh, C.-O. and Hedin, L. *Handbook on Synchrotron Radiation*, vol. 1b (North-Holland, Amsterdam, 1983).

[77] Blaha, P., Schwarz, K., Madsen, G., Kvasnicka, D. and Luitz, J. WIEN2K *package.* URL `http://www.wien2k.at`.

[78] Anisimov, V. I., Solovyev, I. V., Korotin, M. A., Czyżyk, M. T. and Sawatzky, G. A. *Density-functional theory and NiO photoemission spectra.* Phys. Rev. B **48**, 16929–16934 (1993).

[79] Anisimov, V. I., Kuiper, P. and Nordgren, J. *First-principles calculation of NiO valence spectra in the impurity-Anderson-model approximation.* Phys. Rev. B **50**, 8257 (1994).

[80] Kuiper, P., Kruizinga, G., Ghijsen, J., Sawatzky, G. A. and Verweij, H. *Character of Holes in $Li_xNi_{1-x}O$ and Their Magnetic Behavior.* Phys. Rev. Lett. **62**, 221 (1989).

[81] Zhang, F. C. and Rice, T. M. *Effective Hamiltonian for the superconducting Cu oxides.* Phys. Rev. B **37**, 3759 (1988).

[82] Eskes, H. and Sawatzky, G. A. *Tendency towards Local Spin Compensation of Holes in the High-T_c Copper Compounds.* Phys. Rev. Lett. **61**, 1415 (1988).

[83] Ren, X. et al. *$LDA + DMFT$ computation of the electronic spectrum of NiO.* Phys. Rev. B **74**, 195114 (2006).

[84] Kuneš, J., Anisimov, V. I., Skornyakov, S. L., Lukoyanov, A. V. and Vollhardt, D. *NiO: Correlated Band Structure of a Charge-Transfer Insulator.* Phys. Rev. Lett. **99**, 156404 (2007).

[85] Kuneš, J., Anisimov, V. I., Lukoyanov, A. V. and Vollhardt, D. *Local correlations and hole doping in NiO: A dynamical mean-field study.* Phys. Rev. B **75**, 165115 (2007).

[86] Yin, Q., Gordienko, A., Wan, X. and Savrasov, S. Y. *Calculated Momentum Dependence of Zhang-Rice States in Transition Metal Oxides.* Phys. Rev. Lett. **100**, 066406 (2008).

[87] Jiang, H., Gomez-Abal, R. I., Rinke, P. and Scheffler, M. *First-principles modeling of localized d states with the GW@LDA + U approach.* Phys. Rev. B **82**, 045108 (2010).

[88] van Veenendaal, M. A. and Sawatzky, G. A. *Nonlocal screening effects in 2p x-ray photoemission spectroscopy core-level line shapes of transition metal compounds.* Phys. Rev. Lett. **70**, 2459–2462 (1993).

[89] Sangaletti, L., Depero, L. E. and Parmigiani, F. *On the non-local screening mechanisms in the 2p photoelectron spectra of NiO and La2NiO4.* Solid State Commun. **103**, 421 – 424 (1997).

[90] Soriano, L. et al. *Surface effects in the Ni 2p x-ray photoemission spectra of NiO.* Phys. Rev. B **75**, 233417 (2007).

[91] Preda, I. et al. *Interface effects in the Ni2p x-ray photoelectron spectra of NiO thin films grown on oxide substrates.* Phys. Rev. B **77**, 075411 (2008).

[92] Mossanek, R. J. O. et al. *Investigation of surface and non-local screening effects in the Ni 2p core level photoemission spectra of NiO.* Chem. Phys. Lett. **501**, 437 (2011).

[93] Alders, D., Voogt, F. C., Hibma, T. and Sawatzky, G. A. *Nonlocal screening effects in 2p x-ray photoemission spectroscopy of NiO (100).* Phys. Rev. B **54**, 7716–7719 (1996).

[94] Altieri, S., Tjeng, L. H., Tanaka, A. and Sawatzky, G. A. *Core-level x-ray photoemission on NiO in the impurity limit.* Phys. Rev. B **61**, 13403–13409 (2000).

[95] See review in the Theo Thole Memorial Issue. J. Electron Spectrosc. Relat. Phenom. **86**, 1 (1997).

[96] Parameters used for the calculation of the NiO_6 cluster (in eV): Δ=5.0, U_{dd}=6.5, $U_{\underline{c}d}$=7.6, $10Dq$=0.5, T_{pp}=0.8, $V(e_g)$=2.2 (PES), $V(e_g)'$=1.9 (XAS), $V(t_{2g})=V(e_g)/2$, ζ see Ref. [25], Slater integrals 70% (PES)/90% (XAS) of Hartree-Fock values.

[97] Molodtsov, S. L. et al. *Cooper Minima in the Photoemission Spectra of Solids.* Phys. Rev. Lett. **85**, 4184–4187 (2000).

[98] Powell, C. J. and Jablonski, A. *Evaluation of electron inelastic mean free paths for selected elements and compounds.* Surf. Interface Anal. **29**, 108 (2000).

[99] Trzhaskovskaya, M. B., Nefedov, V. I. and Yarzhemsky, V. G. *Photoelectron angular distribution parameters for elements Z=1 to Z=54 in the photoelectron energy range 100-5000 eV.* At. Data Nucl. Data Tables **77**, 97 (2001).

[100] Wassdahl, N. et al. *Recent advances in ultra soft x-ray fluorescence spectroscopy.* AIP Conf. Proc. **215** (1990).

[101] van Veenendaal, M. A., Alders, D. and Sawatzky, G. A. *Influence of superexchange on Ni 2p x-ray-absorption spectroscopy in NiO.* Phys. Rev. B **51**, 13966 (1995).

[102] Alders, D. et al. *Temperature and thickness dependence of magnetic moments in NiO epitaxial films.* Phys. Rev. B **57**, 11623 (1998).

[103] Haverkort, M. W. et al. *Magnetic versus crystal-field linear dichroism in NiO thin films.* Phys. Rev. B **69**, 020408 (2004).

[104] Taguchi, M. et al. *Revisiting the Valence-Band and Core-Level Photoemission Spectra of NiO.* Phys. Rev. Lett. **100**, 206401 (2008).

[105] J. Weinen *et al.* In preparation.

[106] Tanaka, A. *Intersite Effects on Valence Band Photoemission Spectra of Undoped CuO_2 Plane and CuO_3 Chain.* J. Phys. Soc. Jpn. **68**, 3493 (1999).

[107] Park, H., Haule, K. and Kotliar, G. *Cluster Dynamical Mean Field Theory of the Mott Transition.* Phys. Rev. Lett. **101**, 186403 (2008).

[108] Gull, E., Werner, P., Wang, X., Troyer, M. and Millis, A. J. *Local order and the gapped phase of the Hubbard model: A plaquette dynamical mean-field investigation.* Europhys. Lett. **84**, 37009 (2008).

[109] Tsuda, N., Nasu, K., Fujimori, A. and Siratori, K. *Electronic Conduction in Oxides* (Springer, New York, 2000).

[110] Verwey, E. J. W. *Electronic Conduction of Magnetite (Fe_3O_4) and its Transition Point at Low Temperatures.* Nature **144**, 327 (1939).

[111] Wright, J. P., Attfield, J. P. and Radaelli, P. G. *Long Range Charge Ordering in Magnetite Below the Verwey Transition.* Phys. Rev. Lett. **87**, 266401 (2001).

[112] Wright, J. P., Attfield, J. P. and Radaelli, P. G. *Charge ordered structure of magnetite Fe_3O_4 below the Verwey transition.* Phys. Rev. B **66**, 214422 (2002).

[113] Schlappa, J. et al. *Direct Observation of t_{2g} Orbital Ordering in Magnetite.* Phys. Rev. Lett. **100**, 026406 (2008).

[114] Leonov, I., Yaresko, A. N., Antonov, V. N., Korotin, M. A. and Anisimov, V. I. *Charge and Orbital Order in Fe_3O_4.* Phys. Rev. Lett. **93**, 146404 (2004).

[115] Jeng, H.-T., Guo, G. Y. and Huang, D. J. *Charge-Orbital Ordering and Verwey Transition in Magnetite.* Phys. Rev. Lett. **93**, 156403 (2004).

[116] Park, J.-H., Tjeng, L. H., Allen, J. W., Metcalf, P. and Chen, C. T. *Single-particle gap above the Verwey transition in Fe_3O_4.* Phys. Rev. B **55**, 12813–12817 (1997).

[117] Park, J.-H. Ph.D. thesis, University of Michigan (1994).

[118] Jeanloz, R. and Hazen, R. M. *Compression, nonstoichiometry and bulk viscosity of wüstite.* Nature **304**, 620 (1983).

[119] Rao, C. N. R. and Raveau, B. *Transition Metal Oxides* (Wiley-VCH, 1997), 2nd edn.

[120] Parameters used for the calculation of the FeO_6 cluster (in eV): Δ=7.5, U_{dd}=6.0, $U_{\underline{c}d}$=7.5, $10Dq$=0.6, T_{pp}=0.7, and ζ see Ref. [25], Slater integrals 75% of Hartree-Fock values.

[121] Goodenough, J. B. *Spin-Orbit-Coupling Effects in Transition-Metal Compounds.* Phys. Rev. **171**, 466–479 (1968).

[122] Jones, G. D. *Jahn-Teller Splittings in the Optical Absorption Spectra of Divalent Iron Compounds.* Phys. Rev. **155**, 259 (1967).

[123] Ham, F. S. *Mössbauer Spectrum of Fe^{2+} in MgO.* Phys. Rev. **160**, 328 (1967).

[124] Leider, H. R. and Pipkorn, D. N. *Mössbauer Effect in MgO:Fe^{2+}; Low-Temperature Quadrupole Splitting.* Phys. Rev. **165**, 494 (1968).

[125] Manson, N. B., Gourley, J. T., Vance, E. R., Sengupta, D. and Smith, G. *The $^5T_{2g} \rightarrow {}^5E_g$ absorption in MgO:Fe^{2+}.* J. Phys. Chem. Solids **37**, 1145 – 1148 (1976).

[126] Hjortsberg, A., Vallin, J. T. and Ham, F. S. *Jahn-Teller effects in the near-infrared absorption spectrum of MgO:Fe^{2+}.* Phys. Rev. B **37**, 3196–3215 (1988).

[127] Wong, J. Y. *Far-Infrared Spectra of Iron-Doped MgO.* Phys. Rev. **168**, 337 (1968).

[128] Wilkinson, E. L., Hartman, R. L. and Castle, J. G. *Spin Relaxation via Low-Lying Energy Level of Fe^{2+} in MgO.* Phys. Rev. **171**, 299 (1968).

[129] Chappert, J., Misetich, A., Frankel, R. B. and Blum, N. A. *Stress-Induced Angular Momentum Quenching in MgO: Fe^{2+} as Observed by Mössbauer Spectroscopy.* Phys. Rev. B **1**, 1929 (1970).

[130] Modine, F. A., Sonder, E. and Weeks, R. A. *Determination of the Fe^{2+} and Fe^{3+} concentration in MgO.* J. Appl. Phys. **48**, 3514 (1977).

[131] Sangster, M. J. L., Peckham, G. and Saunderson, D. H. *Lattice dynamics of magnesium oxide.* J. Phys. C: Solid State Phys. **3**, 1026 (1970).

[132] Oganov, A. R., Gillan, M. J. and Price, G. D. *Ab initio lattice dynamics and structural stability of MgO.* J. Chem. Phys. **118**, 10174 (2003).

[133] Thole, B., van der Laan, G. and Butler, P. *Spin-mixed ground state of Fe phthalocyanine and the temperature-dependent branching ratio in X-ray absorption spectroscopy.* Chem. Phys. Lett. **149**, 295 (1988).

[134] Liao, M.-S. and Scheiner, S. *Electronic structure and bonding in metal phthalocyanines, Metal=Fe, Co, Ni, Cu, Zn, Mg.* J. Chem. Phys. **114**, 9780 (2001).

[135] Bernien, M. et al. *Tailoring the Nature of Magnetic Coupling of Fe-Porphyrin Molecules to Ferromagnetic Substrates.* Phys. Rev. Lett. **102**, 047202 (2009).

[136] Huang, D. J. et al. *Spin and Orbital Magnetic Moments of Fe_3O_4.* Phys. Rev. Lett. **93**, 077204 (2004).

[137] Goering, E., Gold, S., Lafkioti, M. and Schütz, G. *Vanishing Fe 3d orbital moments in single-crystalline magnetite.* Europhys. Lett. **73**, 97 (2006).

[138] Goering, E., Lafkioti, M. and Gold, S. *Comment on "Spin and Orbital Magnetic Moments of Fe_3O_4".* Phys. Rev. Lett. **96**, 039701 (2006).

[139] Huang, D. J., Lin, H.-J. and Chen, C. T. *Huang et al. Reply:*. Phys. Rev. Lett. **96**, 039702 (2006).

[140] van Elp, J., Potze, R. H., Eskes, H., Berger, R. and Sawatzky, G. A. *Electronic structure of MnO*. Phys. Rev. B **44**, 1530–1537 (1991).

[141] Seehra, M. and Wijn, H. *Various Other Oxides*. Landolt-Börnstein - Group III Condensed Matter **27G**, 4 (1992).

[142] Madelung, O., Rössler, U. and Schulz, M. *Non-Tetrahedrally Bonded Binary Compounds II*. Landolt-Börnstein - Group III Condensed Matter **41D**, 1 (2000).

[143] Terakura, K., Oguchi, T., Williams, A. R. and Kübler, J. *Band theory of insulating transition-metal monoxides: Band-structure calculations*. Phys. Rev. B **30**, 4734–4747 (1984).

[144] Oguchi, T., Terakura, K. and Williams, A. R. *Band theory of the magnetic interaction in MnO, MnS, and NiO*. Phys. Rev. B **28**, 6443–6452 (1983).

[145] Terakura, K., Williams, A. R., Oguchi, T. and Kübler, J. *Transition-Metal Monoxides: Band or Mott Insulators*. Phys. Rev. Lett. **52**, 1830–1833 (1984).

[146] Fujimori, A. et al. *Electronic structure of MnO*. Phys. Rev. B **42**, 7580–7586 (1990).

[147] F. M. F. de Groot. *X-ray absorption of transition metal oxides: An overview of the theoretical approaches*. J. Electron Spectrosc. Relat. Phenom. **62**, 111 – 130 (1993).

[148] Nagel, M. et al. *Ultrathin transition-metal oxide films: Thickness dependence of the electronic structure and local geometry in MnO*. Phys. Rev. B **75**, 195426 (2007).

[149] Fiquet, G., Richet, P. and Montagnac, G. *High-temperature thermal expansion of lime, periclase, corundum and spinel*. Phys. Chem. Miner. **27**, 103 (1999).

[150] Pacalo, K. E. and Graham, E. K. *Pressure and temperature dependence of the elastic properties of synthetic MnO*. Phys. Chem. Miner. **18**, 69 (1991).

[151] Coles, B. A., Orton, J. W. and Owen, J. *Antiferromagnetic Exchange Interactions between Mn^{2+} Ions in MgO.* Phys. Rev. Lett. **4**, 116–117 (1960).

[152] Gordon, B. L. and Seehra, M. S. *Magnetic susceptibility of Mn^{2+} ions in MgO and evidence of clustering.* Phys. Rev. B **40**, 2348–2353 (1989).

[153] Parameters used for the simulation of the MnO on Ag data (in eV): $\Delta = 7.0$, $U_{dd} = 5.5$, $U_{pd} = 7.2$, $T_{pp} = 0.7$. Values for the Slater integrals and the spin orbit coupling from Ref. [30]. Slater integrals 90% of their Hartree-Fock values.

[154] Harrison, A. H. *Electronic structure and the properties of solids: The physics of the chemical bond* (Dover Publications, Inc., New York, 1989).

[155] Sugano, S., Tanabe, Y. and Kamimura, H. *Multiplets of transition-metal ions in crystals* (Academic Press, New York, 1970).

[156] McWhan, D. B. et al. *Electronic Specific Heat of Metallic Ti-Doped V_2O_3.* Phys. Rev. Lett. **27**, 941–943 (1971).

[157] Dernier, P. D. and Marezio, M. *Crystal Structure of the Low-Temperature Antiferromagnetic Phase of V_2O_3.* Phys. Rev. B **2**, 3771 (1970).

[158] Castellani, C., Natoli, C. R. and Ranninger, J. *Magnetic structure of V_2O_3 in the insulating phase.* Phys. Rev. B **18**, 4945 (1978).

[159] Ashkenazi, J. and Weger, M. *A model for the metal-to-insulator transition in V_2O_3.* Adv. Phys. **22**, 207 (1973).

[160] Allen, J. W. *Optical Study of Vanadium-Ion Interactions in $(V_2O_3)_x(Al_2O_3)_{1-x}$.* Phys. Rev. Lett. **36**, 1249 (1976).

[161] Ezhov, S. Y., Anisimov, V. I., Khomskii, D. I. and Sawatzky, G. A. *Orbital Occupation, Local Spin, and Exchange Interactions in V_2O_3.* Phys. Rev. Lett. **83**, 4136 (1999).

[162] Park, J.-H. et al. *Spin and orbital occupation and phase transitions in V_2O_3.* Phys. Rev. B **61**, 11506 (2000).

[163] Elfimov, I. S., Saha-Dasgupta, T. and Korotin, M. A. *Role of c-axis pairs in V_2O_3 from the band-structure point of view.* Phys. Rev. B **68**, 113105 (2003).

[164] Held, K., Keller, G., Eyert, V., Vollhardt, D. and Anisimov, V. I. *Mott-Hubbard Metal-Insulator Transition in Paramagnetic V_2O_3: An $LDA + DMFT(QMC)$ Study.* Phys. Rev. Lett. **86**, 5345 (2001).

[165] Laad, M. S., Craco, L. and Müller-Hartmann, E. *Orbital Switching and the First-Order Insulator-Metal Transition in Paramagnetic V_2O_3.* Phys. Rev. Lett. **91**, 156402 (2003).

[166] Keller, G., Held, K., Eyert, V., Vollhardt, D. and Anisimov, V. I. *Electronic structure of paramagnetic V_2O_3: Strongly correlated metallic and Mott insulating phase.* Phys. Rev. B **70**, 205116 (2004).

[167] Mo, S.-K. et al. *Prominent Quasiparticle Peak in the Photoemission Spectrum of the Metallic Phase of V_2O_3.* Phys. Rev. Lett. **90**, 186403 (2003).

[168] Mo, S.-K. et al. *Photoemission study of $(V_{1-x}M_x)_2O_3$ $(M = Cr, Ti)$.* Phys. Rev. B **74**, 165101 (2006).

[169] French, R. H. *Electronic Band Structure of Al_2O_3, with Comparison to Alon and AlN.* J. Am. Ceram. Soc. **73**, 477 (1990).

[170] Robertson, J. *High dielectric constant oxides.* Eur. Phys. J. Appl. Phys. **28**, 265 (2004).

[171] Eisebitt, S., Böske, T., Rubensson, J.-E. and Eberhardt, W. *Determination of absorption coefficients for concentrated samples by fluorescence detection.* Phys. Rev. B **47**, 14103 (1993).

[172] Jakschik, S. et al. *Crystallization behavior of thin ALD-Al_2O_3 films.* Thin Solid Films **425**, 216 (2003).

[173] Weinen, J. *A New Detector for Bulk-Sensitive XAS on Highly Insulating Samples.* Master's thesis, Universität zu Köln (2009).

[174] Parameters used for the simulation of the V:Al_2O_3 V $L_{2,3}$ XAS (in eV): $\Delta = 4.0$, $U_{dd} = 4.0$, $U_{pd} = 5.0$, $10Dq = 1.7$. Values for the Slater integrals and the spin orbit coupling from Ref. [30]. Hybridization reduced to 75%, Slater integrals 80% of their Hartree-Fock values.

[175] Bocquet, A. E. et al. *Electronic structure of early 3d-transition-metal oxides by analysis of the 2p core-level photoemission spectra.* Phys. Rev. B **53**, 1161 (1996).

[176] Uozumi, T. et al. *Theoretical and experimental studies on the electronic structure of M2O3 (M = Ti, V, Cr, Mn, Fe) compounds by systematic analysis of high-energy spectroscopy.* J. Electron. Spectrosc. Relat. Phenom. **83**, 9 (1997).

[177] Stephens, P. J. and Lowe-Pariseau, M. *Zeeman Study of the Jahn-Teller Effect in the $^3T_{2g}$ State of Al_2O_3: V^{3+}.* Phys. Rev. **171**, 322 (1968).

[178] Rahman, H. U. and Runciman, W. A. *Energy levels and g values of vanadium corundum.* J. Phys. C: Solid State Phys. **4**, 1576 (1971).

[179] Dong-ping, M., Xiao-dong, M., Ju-rong, C. and Yan-yun, L. *Pressure-induced shifts of energy levels of $\alpha - Al_2O_3 : V^{3+}$ and a complete ligand-field calculation.* Phys. Rev. B **56**, 1780 (1997).

[180] Rozier, P., Ratuszna, A. and Galy, J. *Comparative structural and electrical studies of V_2O_3 and $V_{2-x}Ni_xO_3$ ($0 < x < 0.75$) solid solution.* Z. Anorg. Allg. Chem. **628**, 1236 (2002).

[181] Tsirelson, V. G., Antipin, M. Y., Gerr, R. G., Ozerov, R. P. and Struchkov, Y. T. *Ruby structure peculiarities derived from X-ray diffraction data localization of chromium atoms and electron deformation density.* Phys. Status Solidi A **87**, 425 (1985).

[182] Lin, H.-J. et al. *Local orbital occupation and energy levels of Co in Na_xCoO_2 : A soft x-ray absorption study.* Phys. Rev. B **81**, 115138 (2010).

[183] Henrich, V. E. and Cox, P. A. *The Surface Science of Metal Oxides* (Cambridge University Press, New York, 1994).

[184] Tasker, P. W. *The stability of ionic crystal surfaces.* J. Phys. C: Solid State Phys. **12**, 4977 (1979).

[185] Luo, Q., Guo, Q. and Wang, E. G. *Thickness-dependent metal–insulator transition in V_2O_3 ultrathin films.* Appl. Phys. Lett. **84**, 2337 (2004).

[186] Autier-Laurent, S., Mercey, B., Chippaux, D., Limelette, P. and Simon, C. *Strain-induced pressure effect in pulsed laser deposited thin films of the strongly correlated oxide V_2O_3.* Phys. Rev. B **74**, 195109 (2006).

Acknowledgements

Scientific work in physics and, especially, in experimental physics involving experiments at synchrotron light sources cannot be done by a single person only. Teamwork is the crucial ingredient for successful projects here. As a consequence I want to thank quite a number of people for their enormous help and support.

First of all, I would like to thank my supervisor Hao Tjeng. I was lucky to be given the opportunity to continue the work on some of his thin films projects within my PhD thesis after I already did my Diploma thesis in his group. Hao, your knowledge in physics, experimental techniques, theory, but also technical details is really amazing. You taught me that only the combination of experiment and theory is the key to a profound understanding of physical problems. Besides all the scientific details, I learned from you that a good scientist also needs to be a good manager. The way how you manage to cover all these challenges at the same time is really impressive. I learned a lot from you about organization, well structured approaches to the solution of problems, teamwork, and time management. For the latter you are really somebody to be modeled on: For all the very limited time you still manage to take care about the future career of your students.

Thomas Michely, many thanks for refereeing my thesis that spontaneously. I also would like to acknowledge Achim Rosch and Thomas Koethe as the chairman and assessor of the committee of my dissertation, respectively. Manfred Fiebig was my second mentor in the Bonn-Cologne Graduate School of Physics and Astronomy (BCGS). I have enjoyed our discussions in Bonn, BCGS events, and a few poster sessions during conferences.

During my PhD work I had also the opportunity to guide two diploma students. Especially in experimental physics, this is a win-win situation. Rainald Gierth and Jonas Weinen, I enjoyed working with you a lot. Your help was a major contribution to this thesis. Rainald, thanks for your help in the Ni:MgO and Mn:MgO projects. These were really tough beamtimes. I have enjoyed our trips to Hsinchu and Taipei. And thanks for the birthday cake in the lab during an exhausting night shift! Jonas, thank you for your

help, especially for the construction of the nice FY detector. The S/N ratio... The V:Al_2O_3 spectra could not have been recorded without it. Also thank you for supporting me in humming carnival's songs during long night shifts at the synchrotron. You know that people from Cologne sometimes need that to survive. In case you do not like physics anymore at some point in time you should think about a career as a professional air-hockey player!

As stated above, the importance of teamwork especially holds for synchrotron beamtimes (and here especially for thin film projects). Therefore, special thanks go to all the people who I worked with during many beamtimes in Taiwan. I know that the work at the synchrotron is tough and exhausting, especially if something does not work as planned (which is always the case) and if it is not your "own" project. Here, special thanks go to Zhiwei Hu. For you the expression "experience is everything" really holds. You are a living database of x-ray absorption spectra. Having you at the beamline is a priceless advantage. Additionally, you always no about the best restaurants in Hsinchu. Together with you I enjoyed the best seafood I ever had. Simone Altendorf, you are a real specialist in thin film growth. Thanks for all the nice films and good luck for your EuO project which is, I know, really tough. I hope that you finally get some very nice results after all. Yi-Ying Chin, your help at the beamline is highly appreciated. Your translation of the the menu of the "Mensa" of the Chiao Tung University is invaluable. Nils Hollmann helped me with finding out about the wrong orientation/measurement geometry of the V_2O_3 thin films. This saved the results of that beamtime. A real expert in photoemission experiments is Jan Gegner. Thanks for your help with the experiments and for always keeping cool even in stressful moments. The same holds for Hidenori Fujiwara. Your support is highly appreciated. More support during experiments at NSRRC came from Andreas Hendricks and David Regesch. Many thanks! I would like to express my gratitude to Christian Schüßler-Langeheine, Chun-Fu (Roger) Chang, and Thomas Koethe for their help with the installation and commissioning of the Scienta analyzer at the Dragon beamline. Roger, thank you for guiding Rainald and me through the busy streets of Hsinchu and Taipei! I also would like to acknowledge Holger Ott who guided me during my diploma thesis and my first experiences with working at the synchrotron. Ronny Sutarto, most of what I know about MBE and the machines in the Cologne lab I learned from you. You are one of the most caring people I ever met. Thanks for your help during my first beamtime, with the EuO project, and for the nice Fe:MgO data. The beamtimes at the NSRRC would not have been successful without the local support. Chien-Te Chen, I have only met you very few times when we had more severe problems with "your" Dragon beamline. You have always solved these "unsolvable" problems within a few

minutes. Good luck with the new synchrotron! Hong-Ji Lin and Fan-Hsiu Chang, thank you for supplying everything needed at the experiment and keeping the beamline running, but also for the organizational help like the booking of the guesthouse, transportation to the airport, changes of flights etc.. Hui Huang Hsieh, I really appreciate your support at the beamline but also your help with driving us to supermarkets or restaurants. Last but not least I would like to acknowledge the chefs of our two favorite Teppanyaki restaurants in Hsinchu: Great job, great food, great value.

I am also indebted to Jonas Weinen, Thomas Willers, Fabio Strigari, Ku-Ding Tsuei, and Yen-Fa Liao for the measurement of the nice HAXPES data at SPring-8.

Configuration-interaction cluster calculations account for a major part of this thesis. I deeply thank Nils Hollmann for explaining me the use of Tanaka's program and answering all the questions about calculational details. Maurits Haverkort, your help with the simulation of the Fe in MgO spectra is highly acknowledged. Your O_h fits were kind of starting point of that project. Special thanks also go to Hua Wu who did the LDA and LDA+U calculations on NiO and the trigonal crystal field in V:Al_2O_3. Zhiwei Hu is not only a specialist in x-ray absorption experiments but also in the simulation of the spectra. Zhiwei, it was your idea to try to include some distortion in the Fe in MgO simulations. This turned out to be a key issue here. I would like to express my gratitude to Arata Tanaka for the fruitful discussions during his stay in Cologne. His XTLS program is amazingly powerful.

Most of the experimental setups used for the measurements shown in this thesis were not commercially available but rather designed and manufactured on our own. In this context I would like to thank Lucie Hamdan for her skillful technical and organizational assistance, Christian Schüßler-Langeheine for his advice, and, especially, the teams of the mechanical and electrical workshops of the II. Phyikalisches Institut. Both workshops with their heads Werner Külzer and Hans-Gerhard Menz are real masters of their trade. Thank you for always fulfilling my sometimes special requests in very short time but with high precision (I know now that it is no fun to make small precise parts from Molybdenum).

Andrea Helldörfer, Anke Riebe, and Carmen Handels, thank you for guiding me through the university's bureaucracy with orderings, invoices, travel expenses etc...

There is many more people in Hao Tjeng's group with whom I did not work directly on certain projects but with whom I spent a lot of time and from whom I learned a lot. Especially to the current and former inhabitants of room 317 not mentioned so far (I hope I did not forget anybody): Marcel Buchholz, Christoph Trabant, Christian Caspers, Beatrice Coloru, Michael

Zell, Marco Moretti, Stefan Klein, and Sven Binder. Thank you for the funny time that we had together in the office and elsewhere, for the discussions about science but also problems of everyday-life, and also for patiently enduring my stupid comments, humming etc.. And also to all remaining people and guests of the Tjeng-group: Many thanks for the successful collaboration!

I would like to thank the University of Cologne, the DFG via SFB 608, and the BCGS for the funding of my research.

At the end, the last special thanks go to a number of people who did not technically support my work but who play a very important role in my life and have thus also considerably contributed to the success of my work, namely, my parents Ulrike and Michael, my brother Frederik, and my beloved wife Tina. Vielen Dank für Alles, ohne Eure Unterstützung hätte ich das nicht geschafft!

Erklärung

Ich versichere, dass ich die von mir vorgelegte Dissertation selbständig angefertigt, die benutzten Quellen und Hilfsmittel vollständig angegeben und die Stellen der Arbeit - einschließlich Tabellen, Karten und Abbildungen -, die anderen Werken im Wortlaut oder dem Sinn nach entnommen sind, in jedem Einzelfall als Entlehnung kenntlich gemacht habe; dass diese Dissertation noch keiner anderen Fakultät oder Universität zur Prüfung vorgelegen hat; dass sie - abgesehen von unten angegebenen Teilpublikationen - noch nicht veröffentlicht worden ist sowie, dass ich eine solche Veröffentlichung vor Abschluss des Promotionsverfahrens nicht vornehmen werde. Die Bestimmungen der Promotionsordnung sind mir bekannt. Die von mir vorgelegte Dissertation ist von Prof. Dr. L. H. Tjeng betreut worden.

Köln, den 3. Dezember 2010

Tim Haupricht

Publications

1. *Local correlations, non-local screening, and band formation in NiO*
   T. Haupricht, J. Weinen, R. Gierth, S. G. Altendorf, Y.-Y. Chin, T. Willers, J. Gegner, H. Fujiwara, F. Strigari, A. Hendricks, D. Regesch, Z. Hu, Hua Wu, A. Tanaka, K.-D. Tsuei, Y. F. Liao, H. H. Hsieh, H.-J. Lin, C. T. Chen, and L. H. Tjeng
   Submitted to Phys. Rev. Lett.

2. *Local electronic structure of Fe^{2+} impurities in MgO thin films: Temperature-dependent soft x-ray absorption spectroscopy study*
   T. Haupricht, R. Sutarto, M. W. Haverkort, H. Ott, A. Tanaka, H. H. Hsieh, H.-J. Lin, C. T. Chen, Z. Hu, and L. H. Tjeng
   Phys. Rev. B **82**, 035120 (2010), (Editors' Suggestions)

3. *Electronic structure of $SrPt_4Ge_{12}$: Combined photoelectron spectroscopy and band structure study*
   H. Rosner, J. Gegner, D. Regesch, W. Schnelle, R. Gumeniuk, A. Leithe-Jasper, H. Fujiwara, T. Haupricht, T. C. Koethe, H.-H. Hsieh, H.-J. Lin, C. T. Chen, A. Ormeci, Yu. Grin, and L. H. Tjeng
   Phys. Rev. B **80**, 075114 (2009)

4. *Epitaxy, stoichiometry, and magnetic properties of Gd-doped EuO films on YSZ (001)*
   R. Sutarto, S. G. Altendorf, B. Coloru, M. Moretti Sala, T. Haupricht, C. F. Chang, Z. Hu, C. Schüßler-Langeheine, N. Hollmann, H. Kierspel, J. A. Mydosh, H. H. Hsieh, H.-J. Lin, C. T. Chen, and L. H. Tjeng
   Phys. Rev. B **80**, 085308 (2009)

5. *Epitaxial and layer-by-layer growth of EuO thin films on yttria-stabilized cubic zirconia (001) using MBE distillation*
   R. Sutarto, S. G. Altendorf, B. Coloru, M. Moretti Sala, T. Haupricht, C. F. Chang, Z. Hu, C. Schüßler-Langeheine, N. Hollmann, H. Kierspel, H. H. Hsieh, H.-J. Lin, C. T. Chen, and L. H. Tjeng
   Phys. Rev. B **79**, 205318 (2009)